Mathematical Modeling and Simulation of Intravascular Drug Delivery from Drug-Eluting Stents with Biodegradable PLGA Coating

by

Xiaoxiang Zhu

M.S., University of Illinois (2010)
B.S. & M.S., Zhejiang University (2008)

Submitted to the Department of Chemical Engineering
in partial fulfillment of the requirements for the degree of

Doctor of Philosophy

at the

MASSACHUSETTS INSTITUTE OF TECHNOLOGY

September 2014

Author..... Signature redacted
Department of Chemical Engineering
August 14, 2014

Certified by..... Signature redacted
Richard D. Braatz
Edwin R. Gilliland Professor of Chemical Engineering
Thesis Supervisor

Accepted by..... Signature redacted
Patrick S. Doyle
Professor of Chemical Engineering
Chairman, Committee for Graduate Students

Mathematical Modeling and Simulation of Intravascular Drug Delivery from Drug-Eluting Stents with Biodegradable PLGA Coating

by

Xiaoxiang Zhu

Submitted to the Department of Chemical Engineering on July 10, 2014,
in partial fulfillment of the requirements for the degree of
Doctor of Philosophy in Chemical Engineering

ABSTRACT

Drug-eluting stents (DES) are commonly used in coronary angioplasty procedures. A DES elutes drug compounds from a thin polymeric coating into the surrounding coronary artery tissue to reduce in-stent restenosis (a significant lumen loss due to growth of vascular tissue). Biodurable (non-erodible) polymers are often used in the current DES coatings, which stay permanently in the patients. While promising treatment results were obtained, in-stent restenosis remains an issue and late in-stent thrombosis, which is associated with hypersensitivities to the polymer coatings, is also reported. Increasing interests have been raised towards the design of a more biocompatible coating, in particular a poly(lactic acid-co-glycolic acid) (PLGA) coating, for DES applications to improve the drug delivery and reduce adverse outcomes in patients.

This dissertation aims to develop a mathematical model for describing the process of drug release from a biodegradable PLGA stent coating, and subsequent drug transport, pharmacokinetics, and distribution in the arterial wall. A model framework is developed in the first part of the dissertation, where a biodurable stent coating is considered, and the intravascular delivery of a hydrophobic drug from an implanted DES in a coronary artery is mathematically modeled. The model integrates drug diffusion in the coating with drug diffusion and reversible drug binding in the arterial wall. The model was solved by the finite volume method. The drug diffusivities in the coating and in the arterial wall were investigated for the impact on the drug release and arterial drug uptake. In particular, anisotropic vascular drug diffusivities result in slightly different average arterial drug levels but can lead to very different spatial drug distributions, and is likely related to the reported non-uniform restenosis thickness distribution in the artery cross-section.

The second part of the dissertation focuses on modeling drug transport in a biodegradable poly(D,L-lactic-co-glycolic acid) (PLGA) coating. A mathematical model for the PLGA degradation, erosion, and coupled drug release from PLGA stent coating is developed and validated. An analytical expression is derived for PLGA mass loss. The drug transport model incorporates simultaneous drug diffusion through both the polymer solid and the liquid-filled pores in the coating, where an effective drug diffusivity model is derived taking into account factors including polymer molecular weight change, stent coating porosity change, and drug partitioning between solid and aqueous phases. The model predicted *in vitro* sirolimus release from PLGA stent coating, and demonstrated

the significance of the developed model by comparing with existing drug transport models.

An integrated model for intravascular drug delivery from a PLGA-coated DES is developed in the last part of the dissertation. The integrated model describes the processes of drug release in a PLGA coating and subsequent drug delivery, distribution, and drug pharmacokinetics in the arterial wall. Model simulations first compared a biodegradable PLGA coating with a biodurable coating for stent-based drug delivery. The simulations further investigated drug internalization, interstitial fluid flow in the arterial wall, and stent embedment for impact on the drug release and arterial drug distribution of a PLGA-coated stent. These three factors greatly change the average drug concentrations in the arterial wall. Each factor leads to significant and distinguished alterations in the arterial drug distribution that can potentially influence the treatment outcomes.

The developed model here provides the basis of a design tool for evaluating and studying a PLGA coating for stent applications. Simulations using the model helped to provide insights into the potential impacts of various factors that can affect the efficacy of drug delivery. With the developed model, optimization of the model parameters can also be performed for future exploration on the design of PLGA-coated drug-eluting stents.

Thesis Supervisor: Richard D. Braatz
Title: Edwin R. Gilliland Professor of Chemical Engineering

Acknowledgments

My deepest gratitude goes to my advisor, Professor Richard D. Braatz, for being such a wonderful mentor on both research and life. The dissertation work started off at University of Illinois at Urbana-Champaign in 2009, and Prof. Braatz has allowed me the freedom and provided his full support for me to continue the work after I moved to MIT in 2011. Without his guidance and support, the dissertation would not have been possible.

I am also very grateful to my thesis committee members, Professor Daniel G. Anderson and Professor Paula. T. Hammond, for their insightful inputs and suggestions in my dissertation work. I would like to thank all of the current and past members of the Braatz group during my study, particularly those that I have collaborated with (Dr. Ashlee Ford Versypt, Dr. Ali Mesbah, Dr. Stefan Streif, Lifang Zhou, Mo Jiang, Joel Paulson, Benben Jiang, Zhilong Zhu, You Peng, and Paphonwit Chaiwatanodom). I have had such a great time with all the people of the Braatz group both in and outside the lab.

This dissertation was also built on the foundations of support I have received from my dear family and friends. Despite the most difficult time that my family had to go through in the past few years, my mother has always been the pillar and the firm supporter throughout my entire journey of PhD.

The dissertation work was also made possible through the financial support of the National Institute of Health (NIBIB 5RO1EB005181). Other funding resources I have received during my PhD study, including Novartis-MIT Center for Continuous Manufacturing and BP, are also acknowledged.

Table of Contents

CHAPTER 1

INTRODUCTION

1.1 Motivation

Development of controlled release drug delivery systems has opened up a new era of drug therapeutics. In particular, drug-eluting stents (DES) are commonly used in coronary angioplasty procedures. The device helps to reduce in-stent restenosis, a significant lumen loss due to growth of vascular tissue, by eluting drug compounds from a thin polymeric film coating into the surrounding coronary artery tissue. In current DES devices, biodurable (non-erodible) polymers are often used for the coating, which stays permanently in the patients after complete elution of the drug. While promising treatment results are obtained in DES as compared with bare-metal stents, in-stent restenosis remains an issue. Insights into the drug delivery and distribution process in the DES systems are needed. Meanwhile, long-term problems have also been reported, for example, late in-stent thrombosis that is associated with hypersensitivities to the polymer coatings in existing DES designs. Using a more biocompatible coating, in particular a poly(lactic acid-co-glycolic acid) (PLGA) coating, could potentially reduce such problems and improve DES efficacy.

Some preliminary work has been reported in researching PLGA coating for drug delivery in DES. However, limited studies are available due to the high complexity in the system and heavy dependency on trial-and-error experiments. Even for *in vitro* drug release investigation, a thorough understanding of the mechanisms regulating the drug

release is still needed. More complexities are encountered in intravascular drug delivery study, arising from DES interactions with local physiological environment. In order to evaluate and understand DES function, information of drug release and arterial drug uptake are important but yet difficult to acquire.

Mathematical models and simulations offer one possible approach to such information and can facilitate the understanding of the drug delivery process. Drug release behaviors in various conditions can be evaluated, including experimentally studied (model validation) and theoretical interest (prediction). Such models will be very useful for evaluating and designing DES to optimize for specific therapeutic requirements.

The dissertation work is intended to develop a mathematical model for describing the drug release from a biodegradable PLGA stent coating and subsequently drug transport and distribution in the arterial wall. Development of the model requires the understanding of drug transport and behaviors in distinct domains, which includes the changing properties in the degrading PLGA coating, drug interactions in the arterial wall, as well as drug behaviors on the interfaces of different domains. Such a comprehensive model studies the drug delivery and arterial distribution integrally and can offer insights in the design and evaluation of the performance of a DES with PLGA coating.

The objectives of the research proposal are briefly described as below and are discussed in detail section 1.2.

- **Objective 1.** Model intravascular drug delivery from a DES with biodurable coating

- **Objective 2.** Develop a predictive model for the degradation and erosion of PLGA stent coating
- **Objective 3.** Model drug transport in PLGA coating with *in vitro* release validation
- **Objective 4.** Model intravascular drug delivery from a DES with PLGA coating
- **Objective 5.** Explore model factors for intravascular drug delivery

1.2 Research Objectives

In this section, the five research objectives of the dissertation are explained and discussed in detail.

Objective 1. Model intravascular drug delivery from a DES with biodurable coating

The intravascular drug delivery of a hydrophobic drug (such as sirolimus or paclitaxel) from a DES with biodruable coating is modeled. The model aims to incorporate the drug transport in the polymer coating as well as the drug transport and binding in the arterial wall, and is an approximation of *in vivo* drug delivery in a DES.

On one hand, the model simulations will provide insights in the current DES systems with biodurable coatings. The parameter space of the model will be examined, including investigation of different values of the drug diffusivities in the coating and in the arterial wall for impact on drug release rates and spatiotemporal arterial drug distributions. More specifically, anisotropic drug diffusivities in the arterial wall in the circumferential and transmural directions will be studied in detail. On the other hand, the

model for a biodurable coating also serves as a model framework for future studies, where the components can be either replaced by a new one (biodegradable coating) or modified with new features (mechanisms of drug pharmacokinetics in the arterial wall).

Objective 2. Develop a predictive model for the degradation and erosion of PLGA stent coating

The goal is to develop a mechanistic model to describe the degradation and erosion of PLGA thin coatings. The model aims to provide information on the change of polymer molecular weight and coating porosity (or the polymer weight loss), which is necessary for subsequent description of drug transport in the coating.

Objective 3. Model drug transport in PLGA coating with *in vitro* release validation

The development of a drug transport model in a PLGA coating needs to take into account the evolving effective drug diffusivity in the coating as a result of both polymer molecular weight change and coating porosity change. This proposed dual-dependency of the effective drug diffusivity has not been evaluated in the literature and can bring more physical significance compared with the existing forms of effective diffusivity that are dependent on only one factor or the other.

Integrating drug transport model with the PLGA degradation and erosion model, simulations with reported experimental conditions can be performed for model validation using data from *in vitro* studies.

Objective 4. Model intravascular drug delivery from a DES with PLGA coating

This objective requires an integration of the validated coating models for PLGA degradation and erosion (Objective 2) and drug transport (Objective 3) into the intravascular drug delivery model frame (Objective 1). The integrated model will provide a complete description of drug release from a DES with biodegradable PLGA coating. The drug release profiles and arterial drug distributions in the PLGA-coated DES will be simulated and compared with biodurable coating and *in vitro* studies, and further provides evaluation of PLGA coating for DES.

Objective 5. Explore model factors for intravascular drug delivery

Various factors in the model will be explored to study the impact of drug release and arterial drug uptake and distribution enabled by a PLGA-coated drug-eluting stent. The investigation will provide insights into the system for potentially improving the efficacy of drug delivery and treatment outcome.

1.3 Organization

The dissertation work is organized as follows. In Chapter 2, the background concepts of controlled drug release delivery, drug-eluting stents (DES), and drug release in DES are described. A brief literature review of modeling efforts is provided in Chapter 3, which covers the drug release in polymer-coated DES, intravascular delivery in DES, PLGA degradation and erosion and coupled drug release. The model framework (Objective 1) is developed in Chapter 4 based on intravascular drug delivery from DES with a biodurable coating, which provides simulation insights into the current DES design and experimental observations. A mechanistic model for describing the degradation and erosion of PLGA

coating (Objective 2) and the couple drug release (Objective 3) is developed in Chapter 5, with model verifications using reported experimental data. The developed PLGA-drug release model is integrated with the model framework based on biodurable DES coating in Chapter 6 (Objective 4), where model simulations were used to investigate the impact of drug internalization, interstitial flow, and strut embedment on drug release and distribution. Conclusions are presented in Chapter 7.

CHAPTER 2

BACKGROUND CONCEPTS

This section provides an overview of polymer-based controlled release drug delivery systems. Following that, coronary drug-eluting stents (DES) are discussed in detail, including the achievements, existing issues, and recent research progress.

2.1 Polymeric Controlled Release Drug Delivery Systems

Controlled-release drug delivery systems have gained significant growth over the last decades and have opened up a new era of drug therapeutics. Compared with conventional drug therapy, controlled release systems are capable of achieving drug delivery to a target environment with minimum fluctuation and extended duration, and have certain advantages regarding maintenance of drug levels in the therapeutically desirable range, reduction of harmful side effects, potentially less amount of drug needed, as well as less frequent drug administration and better patient compliance [1, 2]. In addition, development of polymeric drug delivery systems have provided better drug protection and improved drug stability, allowing extended activity duration of drugs with short half-life which were previous difficult to utilize [1, 3]. Representative drug delivery systems include polymeric systems, liposome, hydrogel, and responsive drug delivery systems based on magnetic signal, electrical signal, ultrasonic signal, pH and temperature [4]. Using controlled release systems, various bioactive compounds can be delivered, including small molecule drugs, vaccine, protein and DNA for gene therapy [5].

Polymeric controlled-release drug delivery systems are classified broadly into three categories according to the mechanisms of drug release: (1) diffusion controlled systems; (2) chemically controlled systems, where release is activated by the degradation and erosion of the polymer, or the cleavage of a chemical bound between the drug and the polymer; and (3) solvent activation controlled systems such as osmotic pumping or swelling [1, 2]. However, a distinct classification is not easy as a polymeric system can often involve multiple release mechanisms.

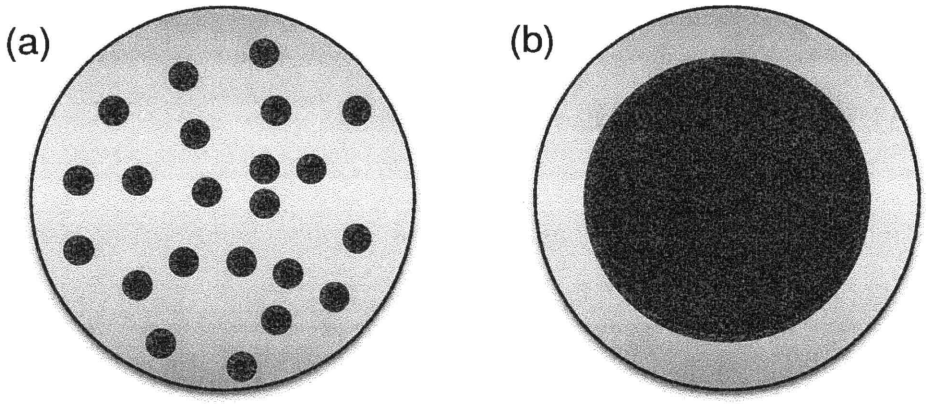

Figure 2.1 In a matrix configuration (a), drug is uniformly dispersed; in a reservoir configuration (b), a drug core is contained in a polymeric shell.

Matrix system and reservoir system are two commonly used configurations for polymeric delivery systems [1, 2]. In a matrix system, a drug is usually uniformly distributed within the polymer matrix and is released by either drug diffusion or a combination of drug diffusion and polymer erosion (Figure 2.1a). A reservoir system typically contains a drug core surrounded by a polymeric out-layer (Figure 2.1b). Large amount of drug can be embedded in a reservoir system, however, such a system may experience the risk of overdose when factures form on the outer polymeric layer.

Both biodurable (non-erodible) and biodegradable polymers are found in controlled drug release systems [3, 6]. A biodurable polymer stays intact both during and after the drug release and is usually used in drug delivery systems which can be retrieved or removed after the drug release, such as oral and transdermal applications [3]. Biodegradable polymers undergo degradation and erosion, which eventually lead to break-down of the devices. Most synthetic biodegradable polymers undergo degradation hydrolytically [7]. Detailed reviews of the polymers used in controlled release are also available [3, 7].

2.2 Polymer-Coated Drug-Eluting Stents

Drug-eluting stents (DES) are commonly used in the cardiovascular intervention procedures. An overview of the advancements and issues in the existing DES design is given in the first part of the subsection. Representative drugs used in DES applications (such as sirolimus and paclitaxel) and their physiochemical properties are discussed. Drug release from biodurable and biodegradable PLGA polymeric coatings in DES are examined in the last part.

2.2.1 Progress and Issues in DES

Drug-eluting stents are used for controlled release of immunosuppressive, anti-inflammatory, or antiproliferative drugs at the wounded coronary artery site after coronary angioplasty procedures [8]. The primary purpose of the delivered drugs is to reduce exaggerated vascular neointimal proliferation in the patients, also known as in-stent restenosis [8, 9]. In-stent restenosis occurs at a high rate (20-30%) in bare metal

stents where a systemic drug administration was not successful due to low tissue drug levels at the target coronary artery site. In comparison, drug-eluting stents enable a prolonged local delivery of drugs, which are embedded in and released from a polymeric stent coating. Significant reduction of in-stent restenosis has been achieved by using drug-eluting stents (a reduction to less than 10%), and several commercialized products are available in clinical applications (Table 2.1) [8-11]. The superior performance of drug-eluting stents over bare-metal stents in controlling in-stent restenosis further reduces the need for reintervention in the treated vessel [12].

Table 2.1 Examples of FDA approved drug-eluting stents in the United States.

Trademark	Drug eluted	Coating polymer
Taxus™ (Boston Scientific)	Paclitaxel	poly(styrene-b-isobutylene-b-styrene)
Cypher™ (Cordis, J&J)	Sirolimus	poly(ethylene-co-vinyl acetate); poly(*n*-butyl methacrylate)
Xience™ (Abbott)	Everolimus	Poly(n-butyl methacrylate); poly(vinylidene fluoride-c-hexafluoropropylene)

The pathways leading to in-stent restenosis is quite complex and several major steps have been identified as inflammation, granulation, extracellular matrix remodeling, and vascular smooth muscle cell proliferation and migration [13]. While a complete understanding of the exact mechanisms in restenosis formation is still in progress, detailed overview of the currently well-accepted mechanisms is available in several reviews [9, 13, 14]. Among those steps in the pathways, the growth and migration of vascular smooth muscle cells is considered as the key process that results in neointimal

proliferation after vascular injury [11]. In order to prevent the growth of restenosis, a period of at least three weeks of continuous release of an antirestenotic drug is suggested [8]. Based on the understanding of the mechanisms, drugs that can target and inhibit different stages in the pathways are selected to be eluted.

Despite the promising initial results, in-stent restenosis still occurs and non-uniform stent strut distribution has been reported to correlate with more restenosis growth in sirolimus-eluting stents [15]. Thickest restenosis at maximum inter-strut angle was reported and is suspected to be caused by a decrease in local drug delivery. Wall shear stress has also been proposed to correlate with the non-uniform restenosis growth [16, 17]. Less restenosis occurred with higher wall shear stress, probably by reducing the accumulation of macrophages which furthers prevents migration of smooth muscle cells and restenosis formation.

Long-term adverse side effects have also been reported with existing drug-eluting stents, with the most concern towards the late in-stent thrombosis [18]. Late in-stent thrombosis is a blood clot forming complication that is rarely seen in bare-metal stents [19]. Several factors are considered to be related to this event. The drugs that target to inhibit the smooth muscle cell proliferation also impair the re-endothelialization process, which causes a delayed re-endothelialization process and may eventually lead to late in-stent thrombosis. The delay in re-endothelialization suggests a necessity of an optimal release profile to achieve drug concentrations that are sufficient to inhibit the proliferation of smooth muscle cells without influencing the re-endothelialization process of the endothelial wall [20]. Another factor is that the biodurable polymer coatings used

are not totally inert and causes hypersensitivity reactions after the complete release of drug [10, 21, 22]. Development of more biocompatible stents are needed [10]. A slowly degrading coating is potentially advantageous in provoking less inflammatory reactions while being able to maintain a sustained release of drugs.

Biodegradable polymers like poly (D,L-lactic acid) (PLA) and poly (lactic acid-co-glycolic acid) (PLGA) are considered to have great potentials for the design of next generation drug-eluting stents. Some attempts have been made to develop totally biodegradable stents. Such stents can reduce restenosis effectively, but a considerable inflammatory response has been observed in the long term due to the degradation of the whole stent [23]. A biodegradable coating, which involves less polymeric material and correspondingly releases less polymers during coating degradation, may be more advantageous. In an extensive study of stent coating with the most applied polymers (five biodegradable and three biodurable), PLGA was found to induce less inflammatory response [24].

2.2.2 Drugs and Their Physiochemical Properties

Sirolimus and paclitaxel are two of the most commonly incorporated drugs in drug-eluting stents and both are very effective in inhibiting the in-stent restenosis [13, 20, 22]. The molecular structures of sirolimus and paclitaxel are illustrated in Figure 2.2. Sirolimus, also called rapamycin, acts by binding to the cytosolic proteins FKBP12 (FK506-binding protein 12), which subsequently binds to a specific cell cycle regulatory protein mTOR (mammalian target of rapamycin) and inhibits the cell proliferation. Paclitaxel reversibly binds to microtubules and promotes the formation of extremely

stable and nonfunctional microtubule bundles, which further inhibits the mitosis. Additionally, both sirolimus and paclitaxel can also bind non-specifically to proteins in the extra cellular matrix and hydrophobic tissue microenvironments [25]. When delivered simultaneously, paclitaxel and sirolimus do not interfere with the other's specific binding, but competition for general binding sites seem to exist [26]. Other drugs in the Limus family such as everolimus and zotarolimus, which also bind to FKBP12 proteins and are even more hydrophobic than sirolimus, are also used [10, 20].

Sirolimus (molar mass 914 g/mol)

Paclitaxel (molar mass 854 g/mol)

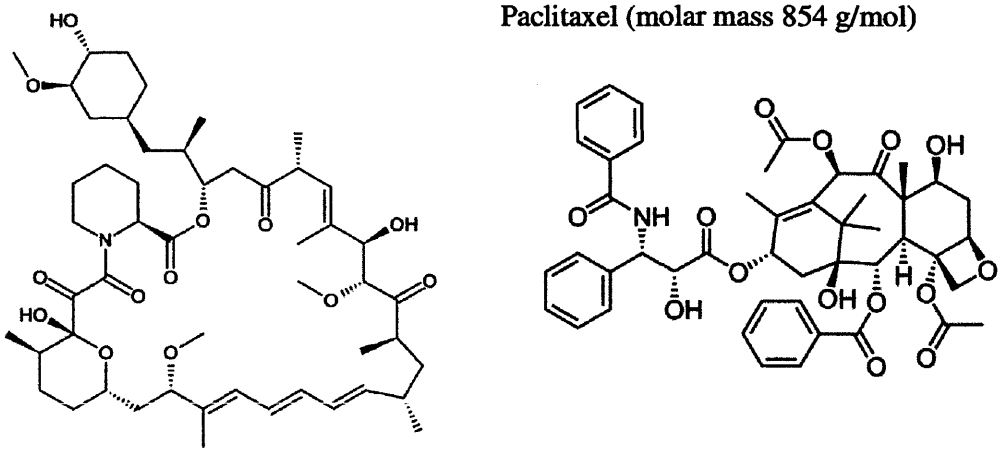

Figure 2.2 Molecular structures of sirolimus (left) and paclitaxel (right). Both drugs are very hydrophobic.

High drug hodrophobicity is necessary to retain the drug in the vascular wall and minimize the drug depletion into the circulation [27]. Hydrophilic drugs such as heparin and dextran, even though biologically potent, are rapidly cleared and therefore ineffective. Both sirolimus and paclitaxel are very hydrophobic drugs with intermediate molecular weight (Figure 2.2) [10]. Strong partitioning into the vascular wall were observed for

both sirolimus and paclitaxel with the drug concentrations 30 to 40 times higher than in the bulk solution [25]. Such tissue partitioning and retention is achieved by the specific binding of drugs with tissue elements and is beneficial for transvascular drug transport, deposition and distribution [28, 29].

The different mechanisms of specific binding and spatial distribution of binding sites lead to different arterial transport properties and distinct transmural profiles of paclitaxel and sirolimus distribution [25, 28]. Sirolimus distributes uniformly within the vascular layers, while paclitaxel exhibits heterogeneous distribution and accumulates more in the adventitia. The difference suggests paclitaxel to be less effective as the media and intimal layers are the primary origin of the cellular components of in-stent restenosis. Both FKBP12 (sirolimus binding site) and microtubules (paclitaxel binding site) have similar cellular concentration of ~ 10^{-5} M [25]. In diseased or injured arteries, the lesion complexity induces changes in the distribution of drug-binding proteins and alters drug distribution [30].

Anisotropic drug diffusivity in the arterial wall is observed and modulated by the arterial ultrastructure, which affects local drug delivery and arterial drug distribution [31]. The diffusivity anisotropy is mostly contributed by transmural obstruction due to the orientation of flat shape of smooth muscle cells. Diffusion in the arterial wall is highly anisotropic for both paclitaxel and sirolimus, with the diffusivity in the planar direction exceeding transmural diffusivity by as large as two orders of magnitude. The diffusivity difference is reported to remain relatively constant for small molecular weight dextran and gradually decrease for dextran molecules larger than 70 kDa [31].

2.3 Drug Release in Drug-Eluting Stents

Drugs used in drug-eluting stents are usually embedded in a polymer matrix in order to avoid bulk release of drug and toxic reactions. In one special case sirolimus was directly coated onto a microporous stent surface [32]. Drug release in both biodurable and biodegradable polymer coatings are discussed.

2.3.1 Biodurable Coating

Biodurable polymeric coatings are used in current FDA approved drug-eluting stents (Table 2.1). The drug release in those devices is dominated by the diffusion mechanism, while different coating layer configurations are seem in the devices [33]. Release with different drug loadings and coating configurations were tested for both sirolimus in Cypher™ stents and paclitaxel in Taxus™ stents. Cypher™ stents used a fast release and a slow release configurations [34]. Both configurations were based on a sirolimus-embedded poly (ethylene-co-vinyl acetate) coating, whereas the slow release configuration has an additional top layer which contains no drug and acts as a drug diffusion barrier. The fast-release configuration released the entire drug loading within 15 days *in vitro*, while the slow-release configuration required more than 90 days for complete sirolimus release. In Taxus™ stents paclitaxel was embedded in poly (styrene-b-isobutylene-b-styrene) at three different loadings to achieve slow, medium and fast releases [35, 36]. All three configurations had initial drug concentrations in the polymer matrix that were much higher than the drug solubility. An initial drug burst was observed in all release profiles, followed by a very slow release via diffusion. Incomplete drug

release were observed in moderate- and slow-release configurations over a considerably long period.

For both Cypher™ and Taxus™ stents, slow-releasing profiles are more favorable than fast release in restenosis outcomes [34]. However, neither of the stents can deliver a good amount of drug beyond 30 days, even though a substantial amount of drug remains in the polymeric coating. This limitation is a result of the very slow drug diffusion through the polymer matrix.

2.3.2 PLGA Biodegradable Coating

Compared with biodurable coating, biodegradable coating like PLGA allows a complete release of embedded drug by degradation and erosion of the polymers. The release profiles in PLGA systems typically contains a slow diffusion-controlled release stage and an accelerated release phase by the combined effect of polymer degradation, erosion and drug diffusion [37].

PLGA stent coating has been studied for *in vitro* release kinetics of various drug agents. PLGA polymer composition, film thickness and drug loading were examined in detail for the release of dexamethasone [38]. Release rates are slower in the dip coated films than in the spray coated ones. Paclitaxel-containing PLGA layers were filled into the holes on a Conor stent and *in vitro* paclitaxel release was controlled by adjusting drug loading as well as placement of blank PLGA layers [39]. Placing blank PLGA layers can reduce initial burst (top or bottom layers) or change the late phase drug release (intermediate layers). A PLGA film containing green fluorescent protein plasmid DNA

was prepared on a coronary stent by coating multiple thin layers of the materials solution [40]. Release of more than 50% of the loaded DNA occurred in the first hour of *in vitro* incubation followed by a zero order release.

Curcumin was mixed with PLGA at the molecular level using an ultrasonic atomization spray method and the release profiles behaved linearly at all low, medium, and high doses [41]. The coating was also observed to be very smooth and uniform before and after the expansion. Rapamycin-eluting stents were prepared using the same procedures, where release profiles, polymer matrix erosion and swollen rates were determined [42]. In a following study, four drugs were prepared in PLGA stent coatings and two release behaviors were observed [43]. Rapamycin (sirolimus) has a biphasic release which includes an initial burst, while the other three drugs heparin, curcumin, and emodin exhibited linear release profiles. A bi-layer structure where the top coating used different molecular weight PLGA and contained less rapamycin effectively prevented the initial burst effect and prolonged the release period.

At loadings of 2%, burst effect was absent in both rapamycin and paclitaxel release from PLGA stent coating [44]. The release showed an initial slow stage controlled by diffusion and a more rapid phase by degradation and erosion. Percentage release profiles of sirolimus from a PLGA coating was indistinguishable at loading of 1% and 2%, and addition of PEG in the coating accelerated release [45]. The unaffected release kinetics was probably explained by the low loading of sirolimus, which permitted a dissolved state in the coating.

An accelerated *in vitro* release method of everolimus was also proposed, which used acetonitrile in the release media to achieve 80% of everolimus release within 24 hours [46]. This method, however, removed the impact of degradation on release kinetics, which is a key factor in modulating the in-body releasing process.

Homogeneous degradation of a PLGA stent coating was observed, which caused 80% polymer molecular weight loss and 60% weight loss of the coating in 60 days [47]. Significant swollen of the coating occurred after one month's degradation. However in another study heterogeneous degradation was reported for both 10 μm and 100 μm PLGA films [48]. Molecular weight of PLGA decreased immediately by degradation upon placement in PBS, and faster degradation occurred in PLGA 50:50 compared with PLGA 75:25 due to the higher content of glycolic units. The immediate degradation in molecular weight was reported elsewhere, and erosion seemed to speed up after a plateau [45]. Porous structure was clearly seem on the PLGA coating surface after 21 days. The weight loss of a PLGA coating (molecular weight 95800, 10 μm thick) appeared a linear profile and swollen of the coating by water absorption started to increase significantly after day five [42].

CHAPTER 3

LITERATURE REVIEW OF MODELING EFFORTS

Drug release kinetics from the coating and arterial drug deposition and distribution are important for the understanding of the precise drug pharmacokinetics. Such information is, however, very limited or sometimes unavailable in experiments. Modeling and simulation studies have been involved to gain insights in the DES delivery systems, which can promote the understanding of the device function and facilitate the improvement of device efficacy. This chapter reviews the modeling work in the literature on drug release in biodurable coatings, intravascular drug delivery from stents, and drug release in PLGA systems.

3.1 Drug Release in Biodurable Coatings

Drug release from a biodurable coating is usually a diffusion-controlled process. Several analytical models are available for describing *in vitro* drug release [33, 49]. A well-known model for release from a biodurable coating is the Higuchi equation (Equation 3.1) for planar drug release systems with drug loading much higher than the solubility [50].

$$M_t = A\sqrt{2D(C_0 - C_s)C_s}\sqrt{t} \tag{3.1}$$

Here the cumulative amount of drug released M_t is dependent on the initial drug concentration C_0, drug solubility C_s, area of the coating A, and drug diffusivity D. The equation was derived based on a pseudo-steady-state approach and assumed

homogeneously dispersed drug in the polymer, fast drug dissolution compared to diffusion, and sink boundary condition. Distinguishable from other empirical equations, the coefficient in the Higuchi equation has physical meanings.

Another model (Equation 3.2) was derived using Fickian diffusion for drug loadings less than solubility [49]. M_∞ is the total amount of drug released as time approaches infinity. A dependency on the square root of time is seem for short time approximation, same as in the Higuchi equation. The expression is valid for the first 60% of release. The solution of Fickian diffusion in cylindrical coordinates was also fitted to experimental data using diffusivity as a fitted parameter for both *in vitro* and *in vivo* conditions [51].

$$\frac{M_t}{M_\infty} = 4\left(\frac{Dt}{\pi L^2}\right)^{1/2} \tag{3.2}$$

The above equations are limited to non-swelling biodurable polymer systems. A generalized equation, known as Peppas equation (Equation 3.3), was proposed to fit drug release with a empirical coefficient k and an exponent of time dependency between 0.5 and 1 [52].

$$\frac{M_t}{M_\infty} = kt^n \tag{3.3}$$

Mechanistic models have also been developed and solved numerically. Two modes of drug transport was used for the release of dispersed everolimus, where fast release occurred through a percolated structure and slow release occurred through the

non-percolated polymer phase [53]. In the majority of the intravascular delivery models, drug release from coating was simplified as a simple diffusion process at some initial drug concentrations (which assumes dissolved drug state) or a continuum pharmacokinetics [54, 55]. Coating parameters such as diffusivity in the coating, coating thickness and strut size were studied in detail with wide range values for the impact on intravascular drug release and arterial drug uptake [56].

Models describe drug release from a biodegradable stent coating are somehow limited. Effect of an degradable coating was analyzed by assuming total polymer erosion in domains containing low drug concentration and subsequent replacement of the domain by arterial tissue [57]. This scenario may correspond to a simplified case of surface erosion polymer. A good amount of work has been published for modeling drug release from PLGA microspheres, and this particular aspect will be discussed in detail in section 3.3.

3.2 Drug Delivery into the Arterial Wall

Drug transport in the arterial wall is primarily dependent on the diffusion, whereas convection has also been examined as a simultaneous transport mechanism. The convection is considered to arise from a transmural hydrostatic pressure gradient and the hydraulic conductivity of the arterial wall [27]. The effect of relative strength of the diffusive and convective forces was examined for both hydrophilic and hydrophobic drugs using continuum pharmacokinetic models [55]. Drug concentrations in the superficial arterial layer and average arterial drug were assessed at different Peclet numbers (the ratio of convective force to diffusive force). Little variability was observed

for hydrophobic drug compared to hydrophilic drug within the physiological Peclet number range of 0.1~10. In another model, the arterial wall was modeled as a porous media and drug delivery from the coating on multiple struts was examined under steady state blood flow [58]. A non-uniform filtration velocity within the arterial wall was induced by the strut obstruction, which facilitates accumulation of drug underneath a stent strut and reduces axial drug distribution. A one-dimensional multilayer porous structure of the arterial wall was also used in the derivation of an analytical solution of drug delivery from a uniform endothelial stent coating [59].

More recent studies solely considers diffusive drug transport in the arterial wall as opposed to a combination of diffusion and convection [57, 60]. In fact, convective transport was experimentally shown to be negligible in thin arteries [61]. The endothelial monolayer acts as a significant resistance barrier to both hydraulic flux and drug entry into the blood in the arterial wall [62]. Using a computational fluid dynamics and mass transfer model, the convection transport in the arterial tissue was demonstrated to be negligible [63].

Large concentration gradients in the arterial wall have been observed for both hydrophilic and hydrophobic drugs in DES drug delivery [55]. Hydrophilic drug was cleared very fast and did not retain in the arterial wall. Hydrophobic drug accumulated in the arterial wall and suffered concentration gradient only in the transmural direction when the stent struts were evenly placed, but circumferential concentration gradient was observed when struts were extremely non-uniformly displaced. Anisotropic diffusivity in the arterial wall was modeled in some work, with circumferential diffusivity ten times as

high as the transmural diffusivity [55, 58]. However a detailed analysis of the impact of different drug anisotropy properties on drug release rate and arterial drug distribution was not seem.

3.2.1 Drug-Arterial Tissue Interaction

Drug-arterial wall tissue interaction is usually described by first order reversible binding reactions [57, 64, 65]. Heparin deposition and distribution in the artery was modeled with heparin-tissue binding in a one-dimensional model [64]. Two scenarios were simulated assuming local binding equilibrium, one with an initially uniformly loaded heparin in the vascular wall and the other with heparin initially loaded in an endovascular hydrogel coating. Very fast clearance of heparin from the vascular wall was also observed in the simulation results. Continuous endovascular coating containing a hydrophilic drug was also assumed in another 1-D model, where a detailed comparison between drug binding and non-binding was examined for arterial drug uptake [65].

3.2.2 Blood Flow

The impact of blood advection on drug release and deposition was studied using steady state fluid dynamics. One major role of blood flow is drug dissipation into the blood by convection [54, 58]. Interestingly, varying the blood flow velocities did not change the drug release profiles from the coating when the strut embedment is fixed [58]. The amount of drug in the arterial wall and drug distribution pattern were also observed to have negligible dependency on the blood flow velocity and drug diffusivity in the blood [54]. In contrast, the diffusivity in the coating and arterial wall were shown to govern the

transport of drug in the arterial wall after stent deployment. These findings suggest a fast drug uptake by advection at the lumen interfaces and justify the appropriate usage of a sink condition at the blood stream boundary for hydrophilic drugs [66]. Steady state blood fluid dynamics was also used in other studies for intravascular drug delivery from DES [56, 60].

In an computational fluid dynamics and mass transfer model, the drug uptake by blood stream was shown to be reabsorbed at the blood-arterial tissue interface and contribute to total drug deposition in the arterial tissue [67]. The strut obstruction induced a recirculation zone of blood at the downstream of the stent strut, and served as a secondary source of arterial drug uptake. Drug deposition via contact of stent coating and the arterial wall was less than the contribution from flow-mediated re-deposition of drug from blood stream. In a following study by the same authors, the pulsatile behavior of blood flow was included [63]. The above findings are interesting, while there is limitation in the models which used a continuous drug concentration at the lumen and arterial wall interfaces and did not discriminate the drug partitioning. More importantly, drug depleted into the blood stream is very likely to bind with various proteins in presence, which will dramatically reduce or even eliminate the re-deposition process.

3.2.3 Stent Geometry and Placement

Different strut appositions (fully embedded, half embedded, and non-embedded) were examined for the drug delivery and distribution in the arterial wall [54]. Fully embedded strut resulted in a higher concentration of drug in the arterial wall as less drug was depleted the blood flow, while half embedded strut showed a more uniform drug

distribution over time. Similar results was observed in another study [58]. These results, however, were based on a equal partitioning of the drug in the coating and the blood, which is reasonable for hydrophilic drug but can deviate significantly for hydrophobic drugs.

Fully embedded stent struts was assumed in a comparison study of a drug-eluting stent and a endovascular bi-layer gel paving stenting [68]. Not surprisingly, more uniform drug distribution in the arterial wall was achieved with a endovascular gel paving. Overlapping struts were simulated and the amount of drug eluted into the local arterial tissue had only slight increase compared with the increase in total drug loading in the struts [67]. The number of stent struts and the arterial wall coverage by the stent coating were also presented in a model for their effect on the arterial drug distribution [69].

3.2.4 Other Factors

Local lesion complexities may also change drug release and deposition. Simulations indicated that thrombus surrounding a stent strut elevated the arterial drug deposition by reducing drug washout, and subsequently increased arterial drug availability [60]. The effect is proportional to the size of peristrut thrombus.

The mechanics of stent implantation, expansion and function was also studied computationally. The expansion of a stent in a coronary artery and following drug release was studied using mechanical and fluid dynamics simulation [70]. Wall shear stress has been studied using computational fluid dynamics and a correlation between wall shear stress and restenosis was seem [16, 17]. Wall shear stress distribution caused non-

uniform distribution of restenosis thickness in a cross-section of stented artery, and higher wall shear stress induced less restenosis growth. Wall stress distributions after stent insertion and deployment were simulated and compared for three different stent designs [71]. Such studies do not directly involve drug release, but are useful in the improvement of the mechanical-side of drug-eluting stents. Detail discussions are not included here since the focus of this thesis is on intravascular drug delivery rather than the mechanics.

3.3 Drug Release in PLGA Systems

Mathematical modeling for drug delivery in PLGA systems are reviewed and discussed in two aspects: polymer change (degradation and erosion) and drug transport.

3.3.1 Modeling PLGA Degradation and Erosion

While degradation and erosion are sometimes used interchangeably, a good clarification is that degradation is a chemical process which describes the scission of polymer backbones and formation of monomers and oligomers, while erosion is a physical phenomena designates the loss of material resulted from the monomers and oligomers leaving the polymer [6].

Surface erosion and bulk erosion are identified as two types of erosion mechanisms [5, 6]. Poly (esters) including PLA and PLGA are described by bulk erosion. Poly (anhydrides) is a group of polymer that undergoes surface erosion predominantly. The primary distinction between the two mechanisms was proposed to be dependent on

the relative rate of water diffusion into the bulk polymer compared with the degradation of the polymer backbone, and a critical dimension exists for each polymer type [72]. For poly (esters) a length scale of 0.1 m is needed for the polymer to lose bulk erosion property.

In PLGA or PLA microspheres, heterogeneous bulk erosion was observed where the particle interior underwent fast erosion, also known as autocatalytic effect [73]. The autocatalytic effect is attributed to the entrapment of monomer and small oligomers in the interior, which creates a more acidic environment and accelerates degradation reactions. Such an effect is dependent on the particle size, where in small PLGA microspheres homogeneous erosion is seem due to the short diffusion length and the lack of an acid concentration gradient. Various critical sizes of observing autocatalytic effect are proposed [73].

In the mathematical modeling of PLGA degradation and erosion, mechanistic approaches are most commonly employed using governing equations of reaction and diffusion [74]. A combined bulk random scission and end scission model were proposed to describe both the molecular weight changes and erosion rate in PLGA microsphere seem in experiments [75]. Assuming homogeneous and first order degradation kinetics, the effect of polymer molecular weight change was analytically incorporated into the drug release in PLGA films [76]. However, no mass loss was accounted in the model. Similar first order degradation models are used in some other models [77, 78]. In a 'shrinking core' approach, where a biodegradable core was coated by a biodurable shell, a degradation model based on the zero, first and second order moments of the molecular

weight distribution was developed to describe the molecular weight change [79]. Later on, the same model was extended by adding a monomer diffusion term for a transition between reaction-controlled and diffusion-controlled states [80].

Although autocatalytic effect is well recognized experimentally, it is rarely described in mathematical models. An early transport-reaction model considered the catalytic effect of embedded acid anhydride in the interior of bulk erodible polymer matrix [81]. A similar unsteady mass balance model was developed for the study of a stent coating, where three species of polymers PLA, oligomer, and monomer were described [82]. Only the lactic acid monomer was considered to contribute to the autocatalytic effect.

The autocatalytic effect was introduced into a computational degradation model of aliphatic polyesters by adding an acid concentration dependency on the rate constants [83]. A threshold of dissolvable oligomer size was assumed in the calculation of the polymer molecular weight change and weight loss. The model explicitly tracks polymers of all lengths and can take into account of different copolymer composition and crystallization effect. One disadvantage is, however, that many polymer details are needed for the model input parameters. The model also implicitly assumes a homogeneous autocatalytic effect in the polymer matrix due to the lack of transport equations. In a following work, a simple analytical expression was derived for describing the number average molecular weight change [83]. No weight loss and constant volume were assumed.

Some other models use probabilistic approaches such as cellular automata method or Monte Carlo method [73, 74]. Those methods are appropriate for describing degradation specially when polydispersity and chain length are considered. However the effects of diffusion is difficult to be included, and a combined Monte Carlo model for degradation and diffusion transport model was seen [74].

3.3.2 Modeling Drug Release in PLGA Systems

Drug delivery has been the most intention of modeling PLGA degradation and erosion. While there are a bulk of work for experimental drug release in PLGA systems, good mathematical models are sought for drug release which can be used for predictions and pre-experimental design.

As both polymer molecular weight and porosity change in an eroding PLGA system, the drug diffusivity for transport is also greatly affected. However, constant drug diffusivity has been commonly incorporated in modeling drug release [75]. Obtaining the correct diffusivity, although intricate, is a key to model the drug release in PLGA systems.

Several expressions considering varying drug diffusivity dependent on polymer molecular weight are used [37]. A diffusivity inversely dependent on polymer molecular weight was used in modeling mifepristone release from PLGA films using pseudo steady state assumption [76]. Analytical solutions was derived and the first part of the release in the expression is similar to the classic Higuchi model for release in biodurable polymer films. An inversely linear relationship between diffusivity and polymer molecular weight was used in another model [77]. However, the expression is doubtable as it shows

inconsistency with the initial diffusivity before degradation. In a more recent study, the dependence of drug diffusivity on molecular weight was determined in monodisperse PLGA microspheres and an empirical correlation was proposed [78]. The correlation was subsequently used in the Fickian diffusion equation for modeling piroxicam release. Similar approach was seem previously for determining an relationship between initial PLA molecular weight and apparent drug diffusivity [84]. An exponential relationship between the diffusivity and the concentration of undegraded PLA was also seen [82].

Even though not seem in the PLGA literature, effective diffusivity through a porous polymer was proposed to be dependent on factors including porosity, tortuosity, and drug partition coefficient [85]. When the solute size is comparable to the pore size, a hindered diffusion transport is observed with an reduction in the effective diffusivity known as restrictivity [86, 87]. Theoretical expressions based on free volume assumption are also derived. A summary of the expressions is available in [49].

CHAPTER 4

MODELING INTRAVASCULAR DRUG DELIVERY FROM STENTS WITH BIODURABLE COATINGS[1]

4.1 Introduction

Drug-eluting stents have shown great benefits in reducing in-stent restenosis after angioplasty procedures compared with bare metal stents [8-11]. The device enables a prolonged local delivery of drugs, such as sirolimus or paclitaxel, which are embedded in and released from the polymeric stent-coating and can interrupt certain stages in in-stent restenosis formation [13, 20, 22]. Significant work has been carried out on stent design [88], *in vitro* drug release from polymeric stent-coating with various configurations including drug type and loading, coating polymer type and molecular weight, and coating thickness [33-36, 38], physiochemical drug properties [22, 25, 28, 89], *in vivo* examination of drug delivery and arterial drug uptake [28-31, 61, 62, 90], and in-stent restenosis formation [15-17, 39, 91]. Nevertheless, the various factors lead to complexities in stent design and evaluation and impede the development of drug-eluting stents.

Modeling and simulation methods promote the understanding of drug-eluting stent function and can facilitate the improvement of device efficacy. Drug release from

[1] Work published as: X. Zhu, D. W. Pack and R. D. Braatz, *Computer Methods in Biomechanics and Biomedical Engineering,* vol. 17, p. 187-198, 2014 (published online in April 2012).

coating and drug-vascular tissue interactions were studied in one-dimensional models [53, 64, 65]. Analytical solution for drug diffusion in one-dimensional multi-layer wall structure was also derived [59]. Convective and diffusive transports of drug in the arterial wall have been assessed for both hydrophilic and hydrophobic drugs [55]. The effects of thrombus [60], blood flow [57, 92], stent coating [56], and strut position [67] on stent-based drug delivery have been investigated for a single strut in the axial profile of the artery using a coupled computational fluid dynamics and mass transfer model. In a cross-section model, drug elution from a fully embedded stent strut was found to be most effective with a bi-layer gel paved stent [68]. Models with multiple struts have also been developed to study the impact of different strut configurations (half, fully, and not-embedded) and diffusivities on arterial drug uptake [54, 58]. Mechanics and fluid dynamics simulation has also been done to study stent expansion and interaction with coronary artery [70].

Additional questions arises as in in-stent restenosis has been experimentally observed to be more likely to occur in stented coronary arteries with non-uniformly distributed struts, and the maximum thickness occurred at the site with maximum inter-strut angle in the artery cross-section [15]. Knowledge of the spatiotemporal drug uptake in the arterial wall can provide some insights into this observation. This chapter mathematically models the integrated process of (1) the delivery of a hydrophobic drug from a drug-eluting stent with bio-durable polymeric coating and (2) drug distribution in the arterial wall with reversible binding. The drug delivery and distribution are studied in a detailed manner for implications on improving device efficacy and reducing in-stent restenosis for drug-eluting stents. Development of such a model can potentially be used

for the optimal stent design *in silico* in the future to avoid sub-optimal stent designs and undesirable outcomes in patient treatments.

4.2 Model Development

4.2.1 Description of the Implanted Stent

The drug-eluting stents studied in this paper have a bio-durable polymeric coating and delivers a hydrophobic drug, which is the case for FDA-approved stents such as Cypher™ stents (Cordis, Johnson & Johnson) and Taxus™ stents (Boston Scientific). The cross-section of the coronary artery with an implanted eight-strut stent is illustrated in Figure 4.1a. The cross-section for each strut is assumed to be square with strut dimension a having a typical value from Cypher stents [88]. The struts are assumed to be distributed evenly in the lumen with same degree of strut embedment, L_p, in the arterial wall, which is within the range of no-embedment to total embedment in previous studies [54, 58, 68].

A single strut section can be separated and studied using the symmetry, as indicated by dotted lines in Figure 4.1a. Based on the small thickness of the coronary artery wall (L_x ~ 200 μm) compared to the diameter of the lumen (2.5-3.5 mm), the single strut section can be modeled as a rectangular arterial wall domain, as in Figure 4.1b. The domain can be further reduced to half to increase the computation speed by symmetry. The inter-strut distance (distance between the centers of two adjacent struts), L_y, is estimated for an eight-strut stent in a 3-mm wide coronary artery. The transmural

and circumferential directions are labeled as the x and y axes, respectively. Blood flow has a direction into the paper plane.

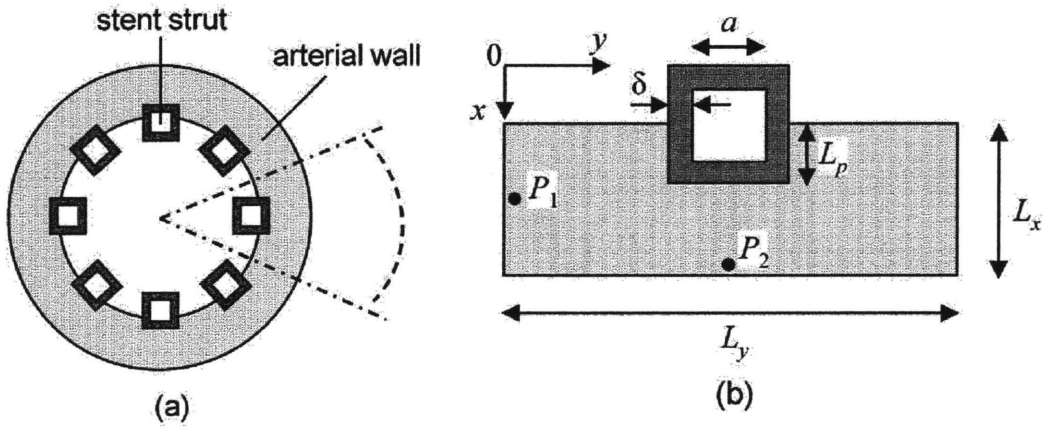

Figure 4.1 (a) Cross-sectional view of an implanted stent in a coronary artery. Dashed lines show a reduced domain by symmetry. (b) Extracted single strut domain with partial embedment into the arterial wall.

Parameters defining the spatial dimensions are labeled in Figure 4.1b, with their values summarized in Table 4.1. The coating thickness δ has values in the literature within the range of 5-50 μm [39], and a value of 50 μm is used consistent with previous modeling work [54, 58]. Strut embedment in the wall can range from no embedment to total embedment [54, 58, 68], revealing slightly different uniformity in drug distribution and higher amount of drug in the arterial wall with increased degree of embedment. In this work the depth of strut embedment into the wall L_p is used with a value close to half-embedment.

Table 4.1 Model Parameters and Values

Dimensions		
strut dimension	a	140 μm [88]
strut coating thickness	δ	50 μm [54]
strut embedment	L_p	no embedment ~ total embedment
coronary artery wall thickness	L_x	200 μm [64]
inter-strut distance	L_y	1000 μm*
Model parameters		
initial drug concentration in the coating	C_0	10^{-5} M [65]
coating drug diffusivity	D_1	0.01~1 $\mu m^2/s$[54]
isotropic vascular drug diffusivity	D_2	0.1~10 $\mu m^2/s$ [25]
transmural vascular drug diffusivity	D_{2x}	0.1~10 $\mu m^2/s$
circumferential vascular drug diffusivity	D_{2y}	1~100 D_{2x} [31]
association rate constant (binding)	k_a	10^4 $M^{-1}s^{-1}$ [89]
dissociation rate constant (unbinding)	k_d	0.01 s^{-1}
resistance at perivascular boundary	R_{wp}	5~100 s/μm [55]
initial binding site concentration	S_0	10^{-5} M [25]
partition coefficient at the perivascular boundary	κ_{wp}	1 [28]
partition coefficient at the coating-arterial wall interface	κ_{cw}	1 [56]

* estimated for an eight-strut stent in a 3-mm wide coronary artery

4.2.2 Mathematical Model

The drug delivery process is described by drug diffusion in the polymeric coating (Equation 4-1) and coupled drug diffusion and reversible binding in the arterial wall (Equations 4-2 & 4-3).

free drug in the coating

$$\frac{\partial C}{\partial t} = D_1 \frac{\partial^2 C}{\partial x^2} + D_1 \frac{\partial^2 C}{\partial y^2} \tag{4-1}$$

free drug in the arterial wall

$$\frac{\partial C}{\partial t} = D_{2x} \frac{\partial^2 C}{\partial x^2} + D_{2y} \frac{\partial^2 C}{\partial y^2} - k_a (S_0 - B) C + k_d B \tag{4-2}$$

bound drug in the arterial wall

$$\frac{\partial B}{\partial t} = k_a (S_0 - B) C - k_d B \tag{4-3}$$

Drug transport by diffusion has been identified as the dominant mechanism in the arterial wall [61] and convective drug transport in the wall is not considered, same as in most models [56, 60]. The coating drug diffusivity (D_1) studied has a range of 0.01-1 $\mu m^2/s$ [54, 65], and the isotropic vascular drug diffusivity has a higher range of 0.1-10 $\mu m^2/s$[25, 28]. Anisotropic vascular drug diffusivity is investigated, where the transmural vascular diffusivity (D_{2x}) has the same range as that of the isotropic vascular diffusivity, while the circumferential vascular diffusivity (D_{2y}) can be the same as the transmural diffusivity for large drug molecules or one or two orders larger in magnitude for decreasing drug molecule sizes [31]. Drug binding in the wall is described as a first-order reversible reaction, $C + S \underset{k_d}{\overset{k_a}{\rightleftarrows}} B$, characterized by an association (binding) rate constant k_a reacting free drug (C) with binding site (S) into bound drug (B), and a dissociation (unbinding) rate constant k_d [57, 64, 65]. The amount of available binding

sites S at each location within the wall can be tracked by the difference between the initial binding sites concentration S_0 and the bound drug concentration B. Reported values for the association (dissociation) rate constants k_a (k_d) [89] and binding site concentrations (S_0) [25] are used as in Table 4.1.

At each interface in Figure 4.1b (defined by the length dimensions), the boundary conditions are expressed in flux form. At the arterial wall-perivascular space interface, the flux is expressed as [55]

$$J_{wp} = \frac{1}{R_{wp}}\left(\frac{C_w}{\kappa_{wp}} - C_p\right) \tag{4-4}$$

where C_p is the perivascular drug concentration, C_w is the drug concentration on the arterial wall side of the interface, κ_{wp} is the partition coefficient (defined as $\kappa_{wp} = [C_w/C_p]_{\text{equilibrium}}$), and R_{wp} is the mass transfer resistance [55]. The boundary conditions at the lumen-coating interface and the lumen-arterial wall interface can be written in a similar way as Equation 4-4. While a washed-out boundary condition is usually adopted for a hydrophilic drug like heparin [64, 65], for hydrophobic drugs such as sirolimus and paclitaxel a zero-flux boundary condition is justified and used as described below.

For hydrophobic drugs like sirolimus and paclitaxel, studies [25, 30] have shown strong partitioning of the drugs into the arterial wall at the lumen-arterial wall interface, even in the presence of binding proteins or in serum [29]. These experimental observations and a high resistance imposed by the intima [62] can greatly damp the drug

depletion into the blood and result in a negligible drug flux into the lumen. In addition, the drug uptake by the bloodstream was found to be a very limited part of the drug initially stored in the polymer coating [57], while simulations have indicated that the blood flow rate and drug diffusivity in the blood have negligible effects on the amount of accumulated drug in the arterial wall [54]. Furthermore, it is the drug transported into the arterial wall that can be effective in suppressing restenosis [13]. Based on these facts, a simplification of neglected drug flux at the lumen-vascular wall and the lumen-coating interfaces is justified.

At the perivascular boundary, drug concentration in the perivascular space (C_p) is assumed zero and the mass transfer resistance (R_{wp}) has a reported range of 5-100 s/μm [55, 65]. Zero flux boundary condition applies to the other interfaces including the coating-strut interface and right/left wall boundaries (due to symmetry). The boundary conditions at the wall-coating interface are described by concentration partitioning and flux matching (Equations 4-5 & 4-6).

$$C_{\text{coating}} = \kappa_{cw} C_{\text{wall}} \tag{4-5}$$

$$-D_1 \left.\frac{\partial C}{\partial x}\right|_{\text{coating}} = -D_2 \left.\frac{\partial C}{\partial x}\right|_{\text{wall}} \tag{4-6}$$

$$-D_1 \left.\frac{\partial C}{\partial y}\right|_{\text{coating}} = -D_2 \left.\frac{\partial C}{\partial y}\right|_{\text{wall}}$$

Values of one are used for the partition coefficients at the coating-vascular wall interface (κ_{cw}) [56] and perivascular boundary (κ_{wp}) [28].

Initial conditions for simulation include uniformly dispersed drug in the polymer coating at concentration C_0, absence of both free and bound drug in the arterial wall, and uniform binding sites throughout the arterial wall at concentration S_0.

4.3 Numerical Simulation

The mathematical model was simulated using the finite volume method. To illustrate how the numerical scheme was developed, for a mesh cell of size Δx by Δy centered at (x, y), Equation 4-2 can be expressed as

$$\begin{aligned}\frac{d}{dt}\int_{x-\frac{\Delta x}{2}}^{x+\frac{\Delta x}{2}}\int_{y-\frac{\Delta y}{2}}^{y+\frac{\Delta y}{2}} C(x,y,t)dxdy = \\ J_x\Big|_{x-\frac{\Delta x}{2},y}\Delta y - J_x\Big|_{x+\frac{\Delta x}{2},y}\Delta y + J_y\Big|_{x,y-\frac{\Delta y}{2}}\Delta x - J_y\Big|_{x,y+\frac{\Delta y}{2}}\Delta x \\ -k_a\int_{x-\frac{\Delta x}{2}}^{x+\frac{\Delta x}{2}}\int_{y-\frac{\Delta y}{2}}^{y+\frac{\Delta y}{2}}\big(S_0 - B(x,y,t)\big)C(x,y,t)dxdy + k_d\int_{x-\frac{\Delta x}{2}}^{x+\frac{\Delta x}{2}}\int_{y-\frac{\Delta y}{2}}^{y+\frac{\Delta y}{2}} B(x,y,t)dxdy\end{aligned} \tag{4-7}$$

where J_x, J_y correspond to the fluxes in the x, y directions, respectively. Applying a forward-difference approximation for the time derivative with a time step Δt and mesh size $h = \Delta x = \Delta y$ results in

$$\begin{aligned}\frac{\overline{C}_{i,j}^{n+1} - \overline{C}_{i,j}^{n}}{\Delta t} = \\ \frac{1}{h}\Big(J_x\Big|_{i-h/2,j}^{n} - J_x\Big|_{i+h/2,j}^{n} + J_y\Big|_{i,j-h/2}^{n} - J_y\Big|_{i,j+h/2}^{n}\Big) - k_a\big(S_0 - \overline{B}_{i,j}^{n}\big)\overline{C}_{i,j}^{n} + k_d\overline{B}_{i,j}^{n}\end{aligned} \tag{4-8}$$

where superscript n is the time index, subscripts i, j are the indices for x, y coordinates of the mesh cell, $\pm h/2$ are the boundaries with neighboring mesh cells, and $\overline{C}$ and $\overline{B}$ are the average of the free- and bound-drug concentrations over the mesh cell centered at (i, j) at

time index n. The flux across boundary of two adjacent mesh cells was calculated by a second-order centered difference, *i.e.*, $J_x\big|^n_{i-h/2,j} = -D\dfrac{\overline{C}^n_{i,j} - \overline{C}^n_{i-1,j}}{h}$.

The numerical simulations were implemented in Matlab 2010b running on an Intel-based personal computer. The explicit numerical scheme used forward-time centered-space discretization [93]. Standard Von Neumann stability analysis of the numerical scheme and further consideration to avoid over-damping gave a criterion of $\dfrac{\Delta t}{h^2} D_2 \le \dfrac{1}{8}$. Similar procedures can be used to derive the stability condition for anisotropic diffusion as $\dfrac{\Delta t}{h^2}(D_{2x} + D_{2y}) \le \dfrac{1}{4}$. This criterion is a sufficient condition for numerical stability as the binding reaction terms in Equation 4-8 are overall negative. While satisfying the stability condition, each simulation was run at several decreasing time steps ranging from 2 s to 0.1 s with an optimized spatial discretization (14,000 mesh cells) until the release profiles in the coating were within the difference of 1%. The correctness of the Matlab implementation was also assessed by reducing the code to a 1D transmural diffusion problem at the high drug loading case, which was subsequently verified with analytical solution.

Values of the parameters used in the simulation are summarized in Table 4.1. Isotropic vascular drug diffusivity (D_2) was first investigated, followed by an anisotropic vascular drug diffusivity study.

4.4 Dimensional Analysis

Some insights of the system characteristics can be obtained by performing dimensional analysis. The characteristic lengths of the coating domain and the arterial wall domain are the coating thickness δ and lengths L_x and $L_y/2$, respectively. Define $\overline{C} = C/C_0$, $\overline{B} = B/S_0$, and non-dimensionalize Equations 4-1, 2, 3 to obtain Equations 4-9, 10, 11 in Table 4.2.

Table 4.2 Non-dimensionalized Equations

$$\frac{\partial \overline{C}}{\partial (t/\tau_1)} = \frac{\partial^2 \overline{C}}{\partial (x/\delta)^2} + \frac{\partial^2 \overline{C}}{\partial (y/\delta)^2} \qquad (4\text{-}9)$$

$$\frac{\partial \overline{C}}{\partial (t/\tau_2)} = \frac{\partial^2 \overline{C}}{\partial (x/L_x)^2} + G_1 \frac{\partial^2 \overline{C}}{\partial (2y/L_y)^2} - G_2\left(1-\overline{B}\right)\overline{C} + G_3\overline{B} \qquad (4\text{-}10)$$

$$\frac{\partial \overline{B}}{\partial (t/\tau_3)} = \frac{G_2}{G_3}\left(1-\overline{B}\right)\overline{C} - \overline{B} \qquad (4\text{-}11)$$

Characteristic time scales and dimensionless groups

$\tau_1 = \delta^2/D_1$	$\tau_2 = L_x^2/D_{2x}$	$\tau_3 = 1/k_d$
$G_1 = \dfrac{L_x^2/D_{2x}}{L_y^2/4D_{2y}}$	$G_2 = \dfrac{L_x^2}{D_{2x}} k_a S_0$	$G_3 = \dfrac{L_x^2}{D_{2x}} \dfrac{k_d S_0}{C_0}$

Three characteristic time scales appear, τ_1, τ_2, τ_3, corresponding to diffusion in the coating, transmural diffusion, and the binding reaction. An evaluation of the magnitude of the three groups gives $\tau_1 \sim 10^3$-10^5 s, $\tau_2 \sim 10^3$-10^5 s, and $\tau_3 \sim 10^2$ s, which indicate that reversible binding is very fast compared to diffusion.

The relative significance of diffusion and reversible binding in the wall is also implied by their corresponding dimensionless groups in Equation 4-10. Compared with the coefficient of transmural diffusion component (which is one), the reaction components have very large coefficients (known as Damköhler numbers), $G_2 \sim 10^2$-10^4 and $G_3 \sim 10^1$-10^3, which also implies that the binding reactions play a very strong role in the spatiotemporal dynamics. The competition between association and dissociation reactions is quantified by $G_2/G_3 = 10$ in Equation 4-11, which indicates a preference of association over dissociation.

The competition between transmural and circumferential diffusion in the arterial wall is implied by the dimensionless group G_1. With increasing D_{2y}, the group G_1 increases from $\sim 10^{-1}$ to ~10, revealing an increasing importance of circumferential diffusion in Equation 4-10 compared with transmural diffusion.

4.5 Results and Discussion

4.5.1 Drug Release Profiles in the Stent Coating

The drug is dissolved in the polymer matrix when the loading is equal to or less than the solubility, and the drug transport in the coating is purely diffusion controlled [94]. Due to the absence of drug aggregates, the dissolved drug concentration in the stent coating depletes gradually with the release.

The release rate decreases significantly with reduced coating drug diffusivity (D_1), when the isotropic vascular drug diffusivity (D_2) remains constant (see Figure 4.2).

Lower coating diffusivity is associated with prolonged drug release, which is in agreement with previous studies [54, 56]. Within the simulated range of coating diffusivity D_1, more than 90% of the total drug is released in the first 100 hr at a high D_1 value of 1 $\mu m^2/s$, while a two-order lower D_1 ensures a prolonged release of the drug by releasing less than 70% within 400 hr.

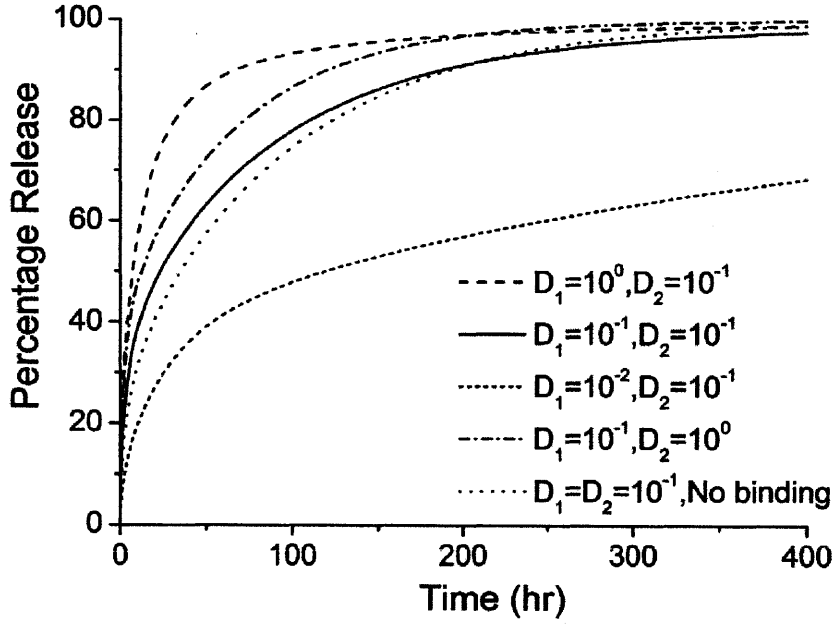

Figure 4.2 Drug release profiles in the stent coating at different diffusivities (with binding) and in non-binding case (the diffusivities are in units of $\mu m^2/s$).

Meanwhile, changes in the vascular diffusivity D_2 and the presence of binding in the wall both affect the drug release process. Compared to the same change in D_1, increment of an order in the magnitude of D_2 significantly enhances the release rate as well. Elimination of the binding reactions results in a slightly reduced release rate,

explained by the fact that with binding a greater concentration gradient is produced in the wall by transferring free drug into bound form [65], and thus faster drug transport from the coating-wall interface. These findings suggest a potentially significant impact of drug-arterial wall interactions on the drug release from an implanted stent. In a clinical application of an implanted stent, even more complexity may arise due to the physiological environment compared with the simplified domain in this model. This impact leads to a difference from *in vitro* release measurements carried out in buffer solutions. In particular, for a drug-eluting stent with hydrophobic drug, where the drug dissipation into blood is small or negligible, drug-arterial wall interactions can vary the release profiles greatly.

4.5.2 Spatially-Averaged Drug Concentration

Two types of drug forms exist in the arterial wall: free drug and bound drug. The temporal profiles for the spatial average of both drug concentrations in the arterial wall were simulated (that is, the integral of the concentration over the arterial wall domain in Figure 4.1b divided by its volume). The spatially-averaged bound-drug concentration was about an order of magnitude higher than that of free drug in Figure 4.3, which is consistent in magnitude with the ratio of their dimensional groups, $G_2/G_3 = 10$. This also implies the preferred association than dissociation in the reversible binding process. For each simulated diffusivity pair (D_1,D_2), the spatially-averaged bound- and free-drug concentrations have similar trends over time.

The spatially-averaged free- and bound-drug concentrations in the arterial wall approach quasi-steady values that reduce slowly for most (D_1,D_2) pairs (see Figure 4.3).

The time needed to reach peak concentrations for both bound- and free-drug can be estimated by the diffusion time in the transmural direction, τ_2. Evaluation with the real dimensions (reduced transmural distance due to strut embedment) in Figure 4.1b gives τ_2 = 33.6 hour for D_2 = 0.1 $\mu m^2/s$, which is in agreement with the peak positions for corresponding plots in Figure 4.3. Besides, noticeably the quasi-steady spatially-averaged drug concentrations are dominated by the diffusivity in the wall, D_2, rather than the diffusivity through the stent coating, D_1. While all three (D_1,D_2) pairs with the same D_2 (0.1 $\mu m^2/s$) achieved similar quasi-steady spatially-averaged drug concentrations, the fourth (D_1,D_2) pair with an order-of-magnitude higher D_2 (1 $\mu m^2/s$) had a much lower quasi-steady drug concentration (see Figure 4.3). Under quasi-steady conditions, both diffusion and binding achieve a dynamic equilibrium throughout the arterial wall, and with the drug dissipation in the arterial wall occurring through the perivascular space, the binding kinetics and the vascular diffusivity D_2 provide the tradeoff that specifies the quasi-steady spatially-averaged drug concentrations. Higher vascular drug diffusivity speeds the transport of free drug through the arterial wall and faster dissipation of drug at perivascular boundary.

While the quasi-steady spatially-averaged drug concentrations are similar for the same vascular diffusivity D_2, the spatially-averaged drug concentrations are higher in early times for increased stent coating diffusivity D_1 (see Figure 4.3). The higher D_1 results in faster initial drug transport through the stent coating into the arterial wall [54], before approaching quasi-steady spatially-averaged drug concentrations. These observations can provide some guidance in the design of the stent coating to maintain the vascular drug concentrations within the therapeutic window throughout the treatment.

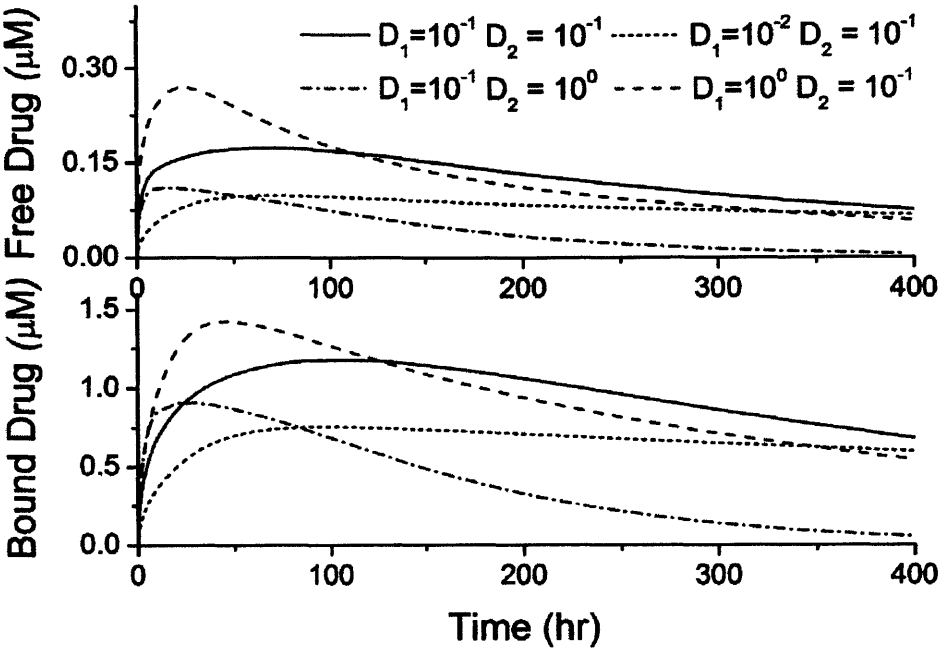

Figure 4.3 Spatially-averaged concentrations for the free- and bound-drug in the arterial wall for different coating and vascular diffusivities ($\mu m^2/s$).

4.5.3 Anisotropic Diffusivities in the Wall

The vascular drug diffusivity can be anisotropic in the transmural and circumferential directions in the coronary artery wall, mainly attributed by the flat shape of the smooth muscle cells [31]. For small drug molecules, the circumferential vascular diffusivity can be as high as orders of magnitude larger than the transmural diffusivity, but the anisotropy in the diffusivity gradually diminishes with increasing drug molecules. Although anisotropic diffusivity was accounted in some of the studies [55, 58], there has not been a full investigation on this property. Here diffusivity anisotropy in the arterial

wall is studied in detail for its impact on the drug concentration and distribution in the wall.

The spatially-averaged drug concentrations in the arterial wall were enhanced with increased circumferential vascular diffusivity D_{2y}, when the transmural diffusivity D_{2x} remains the same (see Figure 4.4). With increased D_{2y}, the diffusion in the circumferential direction competes over penetration through the arterial wall [31], reduces the penetrated drug concentration close to the perivascular interface and corresponding local drug dissipation. This allows a longer time for the arterial drug build-up and as a result the peak times for anisotropic cases are observed to be shifted slightly to the right compared to the isotropic case (Figure 4.4). Meanwhile, increased circumferential vascular diffusivity transports drug in the arterial wall away from the stent coating more quickly, resulting in faster drug release from the stent coating. These factors mentioned contribute to the enhanced spatially-averaged bound-drug concentrations at increased D_{2y}. In early times the spatially-averaged free-drug concentration is slightly lower at enhanced circumferential diffusivity due to the increased availability of binding sites within the arterial wall where drug has diffused. With the anisotropy ratio (ratio of circumferential diffusivity to transmural diffusivity, D_{2y}/D_{2x}) increased from 10 to 100, the corresponding increment in the quasi-steady drug concentrations becomes less significant. This observation is partly explained as that when the circumferential diffusion is very fast compared with transmural penetration, the latter becomes the dominant limitation for drug transport in the wall and dissipation at the perivascular side. More details are included in following discussions for Figure 4.5.

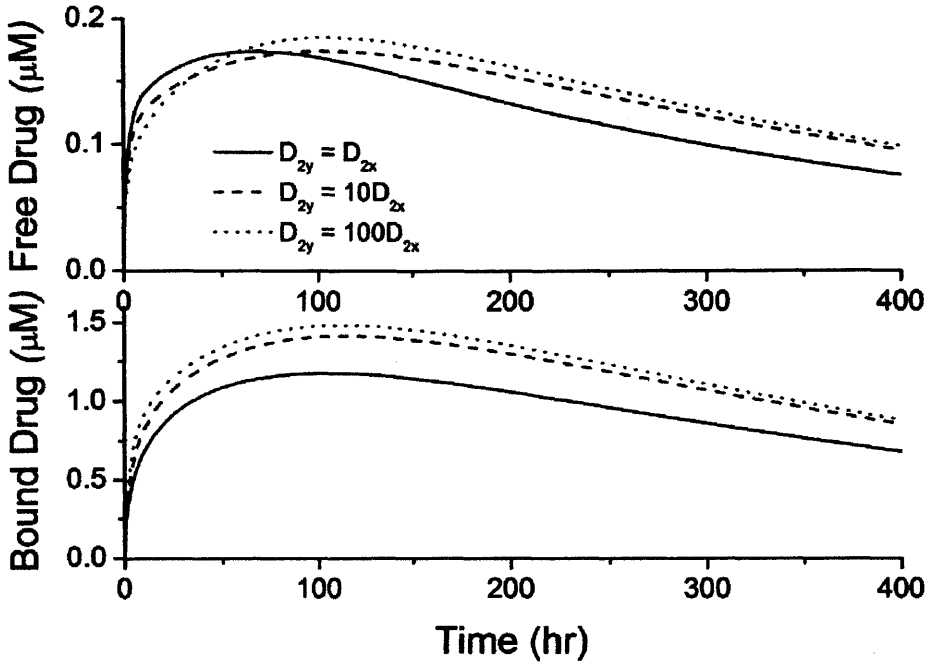

Figure 4.4 Spatially-averaged concentrations for the free- and bound-drug in the arterial wall at different circumferential diffusivities ($D_{2x} = 0.1\ \mu m^2/s$).

Anisotropic diffusivity changes the spatial distribution of drug in the arterial wall greatly (Figure 4.5). Depending on the particular value of the vascular diffusivity anisotropy ratio, drug concentrations can range from being highly non-uniform along the circumference of the arterial wall (Figure 4.5 A-1) to being highly uniform (Figure 4.5 C-1), whereas a concentration gradient always exists in the transmural direction. At very high anisotropy ratios, the drug concentrations can be well approximated as only being a function of time and depth in the transmural direction (Figure 4.5 C-1).

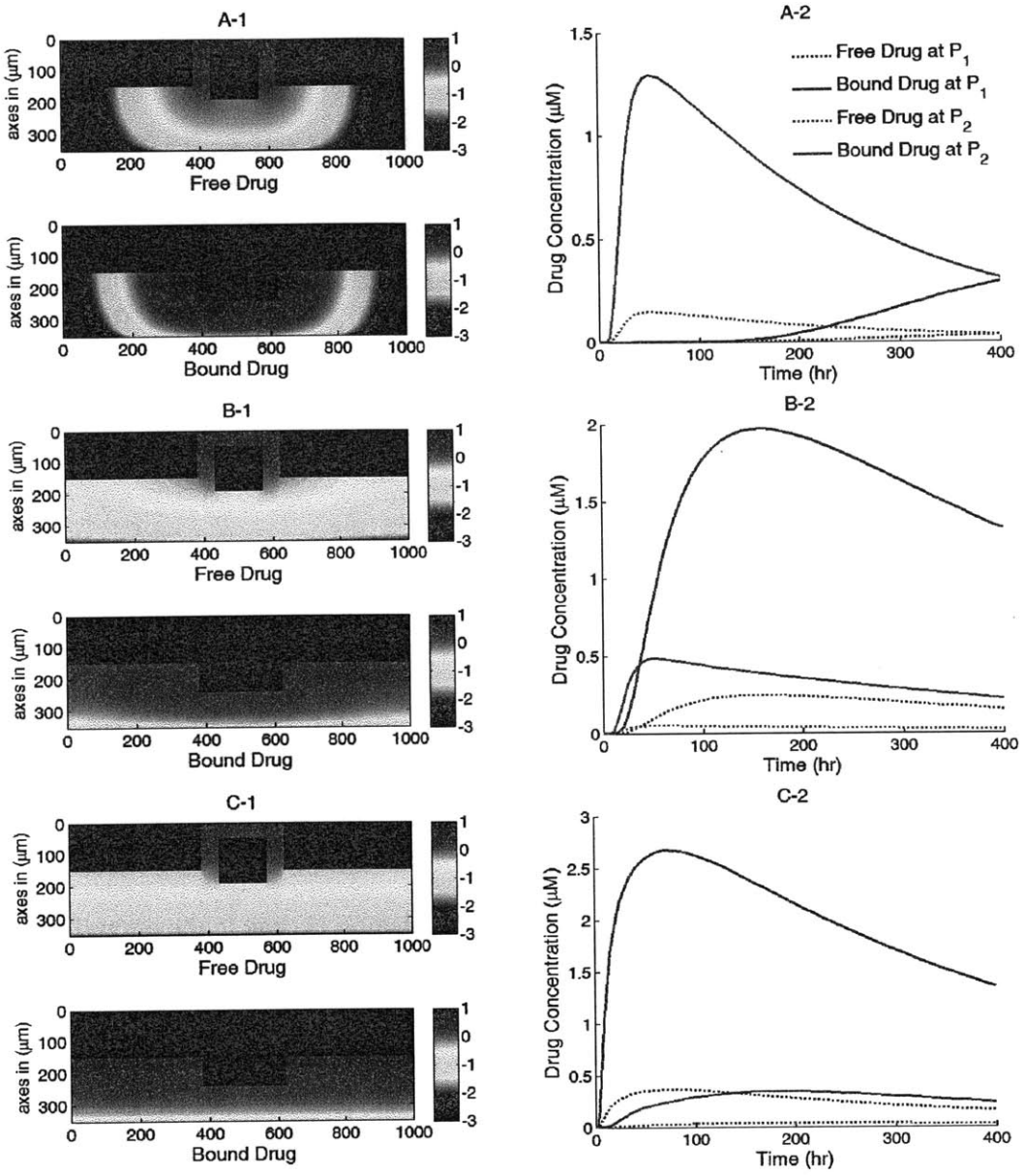

Figure 4.5 A,B,C-1: drug concentration fields at different circumferential diffusivities at 100 hr with low drug loading in the coating (logarithmic plots, $D_{2x} = 0.1\ \mu m^2/s$, x and y axis are dimensions in μm); A,B,C-2: time evolution of drug concentrations (μM) at point P_1 (blue) and point P_2 (red), free (--) and bound (—) drug. (A) $D_{2y} = D_{2x}$, (B) $D_{2y} = 10D_{2x}$, (C) $D_{2y} = 100D_{2x}$.

The time evolution of the drug concentrations at positions P_1 and P_2 (near the left and the perivascular boundaries in Figure 4.1b) are shown in Figure 4.5 as well. With increasing circumferential diffusivity D_{2y}, the free- and bound-drug concentrations at P_1 increase, and those at P_2 decrease. The reduced local drug concentrations at P_2 at increased circumferential diffusivity further reduces the drug dissipation at the perivascular boundary, resulting in the slightly higher spatially-average drug concentrations observed in Figure 4.4.

The first appearance of drug at P_1 and P_2 corresponds to the diffusion time in each direction (see right column in Figure 4.5). For isotropic diffusion in Figure 4.5A-2, the diffusion time in the circumferential direction is a lot longer than the penetration time. The drug distribution is very non-uniform in the circumferential direction when transmural penetration is already achieved, and areas with negligible drug concentrations exist far away from the strut (see Figure 4.5A-1). Similar results on free-drug concentration distribution have been reported in a model where drug binding was absent [55]. The lack of drug in upper layers far away from the strut in the circumferential direction can be a serious factor of restenosis occurrence, as high drug concentrations in the upper layers of wall is more important than penetration in suppressing restenosis [22]. This lack of drug in the upper layers of the arterial wall away from the stent strut after implantation also provides a potential explanation to the reported observation that the thickest restenosis occurs at the largest inter-strut angle site, where two sent struts are further apart due to uneven stent placement [15]. This finding could further contribute to the observed asymmetric neointimal thickness distribution in arterial cross-section, for

which higher wall shear stress was considered as an important factor to induce less neointimal growth [16, 17].

For $D_{2y} = 10D_{2x}$, the time evolution of the free- and bound-drug concentrations at the locations P_1 and P_2 in Figure 4.5B-2 shows comparable diffusion times with both positions initially receiving drug at a similar time. With even higher D_{2y} ($100D_{2x}$), the diffusion time in the circumferential direction is much shorter compared to that of penetration (see Figs. 5C-1 and 5C-2). In this case, a very fast coverage of drug in the upper media layers is achieved, and nearly uniform drug concentrations in the circumferential direction are produced. The potential adverse effect of unevenly placed struts could be greatly reduced, compared with isotropic diffusion. These simulations indicate that drugs with high diffusivity anisotropy in the arterial wall are preferable from the clinical point of view, in terms of achieving higher and more uniform drug concentration in the upper layers of the arterial wall.

4.5.4 High Drug Load ($C_0 >> C_s$)

In clinical applications high drug loadings are used that are very often orders of magnitude higher than the solubility in the matrix and most of the drug is dispersed in the polymer matrix in aggregated form [33]. While the drug is released from the stent coating, the dynamic equilibrium between drug aggregates and dissolved drug ensures a continuous drug supply. When reaching a dynamic equilibrium is fast compared to the release, the drug concentration can be assumed as constant at its solubility within the coating, similar to the continuum pharmacokinetics situation investigated in some works [92]. In this case, the spatially-averaged drug concentrations in the arterial wall achieve

quasi-equilibrium values (as in Figure 4.6) until the drug aggregates in the coating is eventually depleted. Shorter times are required to achieve quasi-equilibrium with increased circumferential diffusivity, and the quasi-equilibrium drug concentrations are enhanced. Due to the availability of the prolonged drug source, the trend of enhancement is more significant here than in Figure 4.4.

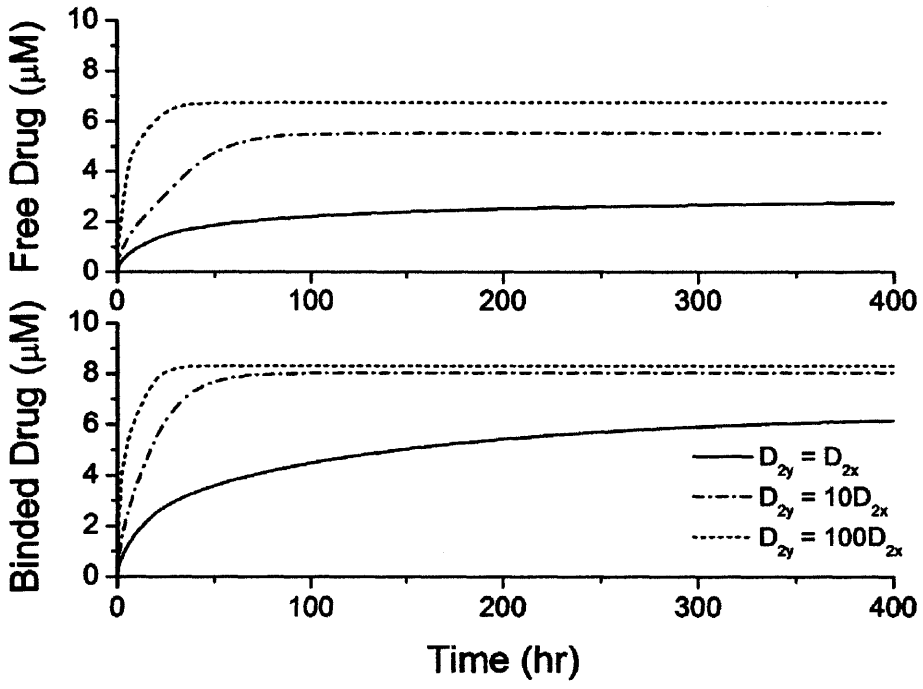

Figure 4.6 Spatially-averaged free- and bound-drug concentrations (μM) in the arterial wall under continuous drug release from the stent coating at high drug loading ($D_{2x} = 0.1\ \mu m^2/s$).

The drug distribution profiles for isotropic vascular diffusivity indicate that quasi-equilibrium has not yet fully established after 400 hours due to the slow diffusion in the circumferential direction (Figure 4.7A-1, 2). The low quasi-equilibrium drug

concentrations at sites far away from the strut in the circumferential direction lends support to the finding in the previous section that maximum restenosis thickness at maximum inter-strut angle is related to lack of drug in that position. Quasi-equilibrium was established quickly when the circumferential diffusivity D_{2y} is enhanced (cases B and C in Figure 4.7.). In Figure 4.7B-1, the free-drug concentration forms a clear gradient centered at the strut even at quasi-equilibrium, indicating non-uniformity of drug concentration in both circumferential and transmural directions. When D_{2y} is increased to $100D_{2x}$ in Figure 4.7C-1, the fast circumferential diffusion compared with penetration resulted in planar layers containing uniform equilibrium drug concentrations, and layers form a drug gradient downward the arterial wall, similar to Figure 4.5C-1.

The concentrations at boundary points P_1 and P_2 (as located in Figure 4.1b) in Figure 4.7 (A,B,C-2) have a similar initial trend as those in Figure 4.5, while reaching at constant quasi-equilibrium levels. In Figure 4.7C-2, the free-drug concentration at quasi-equilibrium is higher than that of the bound drug at P_1. A careful investigation of C-1 shows that this circumstance is true for a large vascular area neighboring the strut. Although part of the arterial wall has higher free-drug level than that of bound drug, the spatially-averaged concentration is still lower for free drug (see Figure 4.6), as expected from the preferred association to dissociation in binding. These simulations show that, while the spatially-averaged concentrations have higher bound-drug concentration than that of free drug, this observation does not necessarily hold for individual vascular sites.

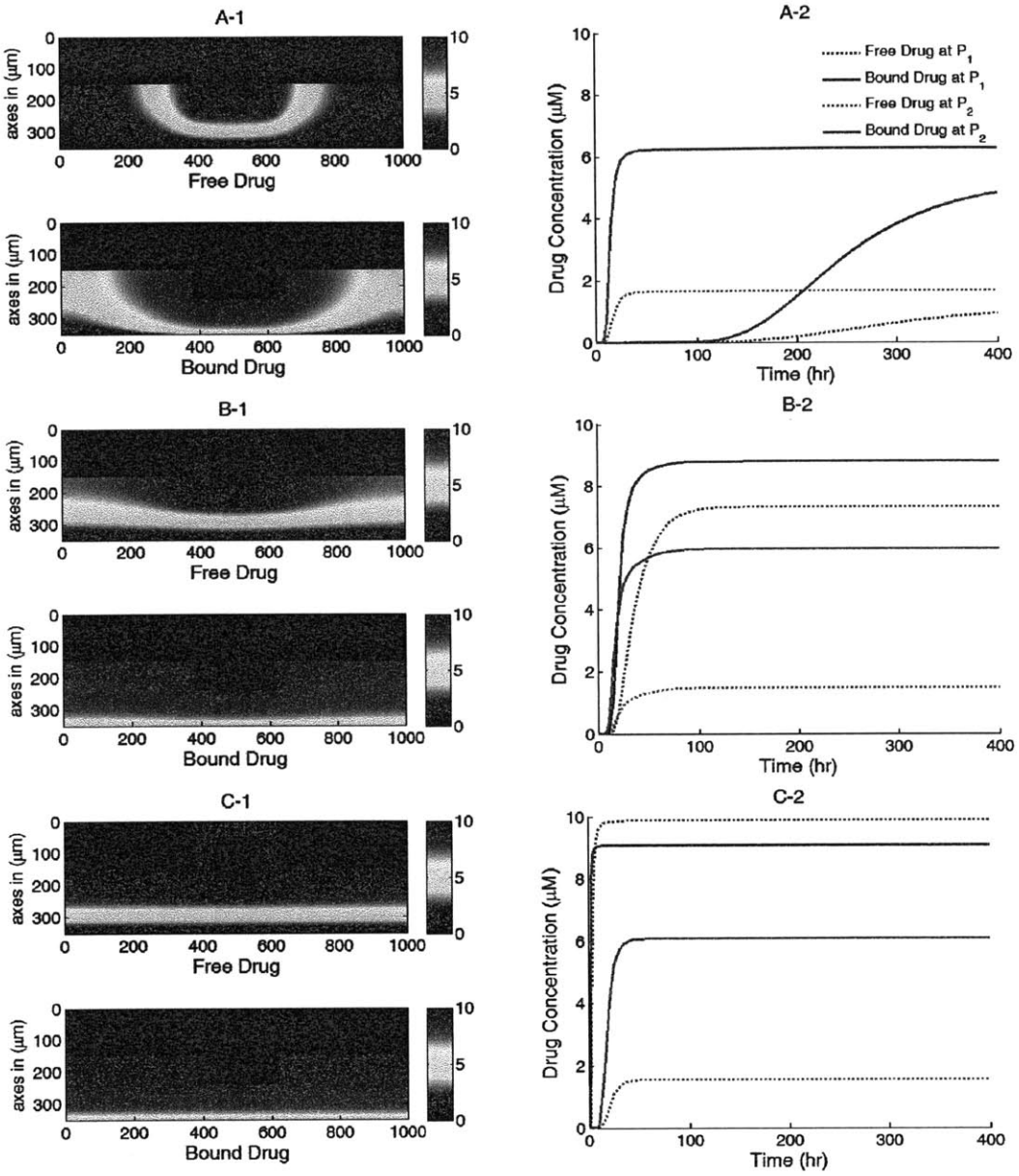

Figure 4.7 A,B,C-1: drug distribution profiles at different circumferential diffusivities at 400 hr with high drug loading in the coating (D_{2x} = 0.1 μm^2/s, x and y axis are dimensions in μm); A,B,C-2: concentration (μM) evolution at point P_1 (blue) and point P_2 (red), free (--) and bound (—) drug. (A) $D_{2y} = D_{2x}$, (B) $D_{2y} = 10D_{2x}$, (C) $D_{2y} = 100D_{2x}$.

The critical condition for the occurrence that free-drug concentration exceeds that of bound-drug can be derived. Assuming at equilibrium conditions, the rates of association and dissociation in Equation 4-3 are equal, $k_a C(S_0 - B) = k_d B$. This equation can be rearranged to solve for the free-binding-site concentration in terms of the free-drug concentration, $B = KCS_0/(KC+1)$, where $K = k_a/k_d$ is the binding equilibrium constant. For a higher concentration of free drug than bound drug, or $C > B$, the condition can be reduced to $C > S_0 - 1/K$. Because the highest free-drug concentration in the wall occurs at the coating-wall boundary, where $C = C_s/\kappa_{CW}$, and the inequality becomes Equation 4-12,

$$C_s/\kappa_{cw} > S_0 - 1/K \tag{4-12}$$

When this inequality is satisfied, higher free-drug concentration can occur in the region close to the strut. Furthermore, the relationship also defines the boundary of equal free- and bound-drug concentrations in this work, which is met by $C = S_0 - 1/K = 9$ μM.

4.4 Conclusions

The intravascular drug delivery of a hydrophobic drug from a drug-eluting stent and coupled drug binding and distribution in the arterial wall were modeled simultaneously. Dimensionless groups were derived to provide insights into the relative importance of directionally-dependent diffusivities and reversible binding on the spatiotemporal distribution of drug in the surrounding arterial wall. Drug release from a implanted drug-eluting stent is affected by the surrounding arterial wall via the vascular drug diffusivity

and reversible binding reaction, which implies a potentially large difference from *in vitro* release behaviors of a hydrophobic drug. Moreover, the average drug concentrations in the arterial wall at quasi-steady state are observed to be greatly determined by the vascular drug diffusivity rather than the coating drug diffusivity. Anisotropic vascular drug diffusivities result in slightly different spatially-averaged drug levels but very different spatial distributions, and higher free-drug concentration than bound-drug concentration can occur in the arterial wall. For the latter the critical condition of occurrence was derived as $C_s/\kappa_{cw} > S_0 - 1/K$. Higher circumferential vascular diffusivity reduces the drug gradient in the circumferential direction and produces more uniformly loaded drug layers, which can be beneficial in reducing in-stent restenosis after drug-eluting stent implantation. Simulation results as presented here provide insights as to how changes in drug properties (such as its directional diffusivities) influence spatial uniformity in the arterial wall and show potential guidance for designing drug-eluting stents with improved efficacy.

CHAPTER 5

MODELING DRUG RELEASE IN PLGA COATING COUPLED WITH POLYMER DEGRADATION AND EROSION[2]

5.1 Introduction

Drug-eluting stents (DES) are predominantly used in coronary angioplasty procedures for reducing in-stent restenosis. Their distinguished therapeutic effect is attributed to the prolonged local release of anti-inflammatory or antiproliferative drugs from a polymeric stent coating into the arterial wall [13]. Biodurable polymers are most commonly used for the stent coatings in DES, which release only part of the loaded drug and induce problems related to the intact polymer coating remaining in the arterial lumen after release (such as hypersensitivity reactions and late in-stent thrombosis) [33, 34]. The need of overcoming those problems has led to research on improving the DES techniques, and special attention has been paid on the evaluation of biodegradable polymers, in particular poly(D,L-lactic-co-glycolic acid) (PLGA), as alternative drug carriers [10, 95].

PLGA has been well recognized for its suitability in drug delivery due to its good biocompatibility and ability to achieve complete drug release as a result of degradation and erosion of the polymer matrix [37, 96]. While degradation and erosion are intricately connected, they correspond to different processes. Degradation is a chemical process that

[2] Work submitted as: X. Zhu and R.D. Braatz, A Mechanistic Model for Drug Release in PLGA Biodegradable Stent Coatings Coupled with Polymer Degradation and Erosion, *Journal of Biomedical Materials Research Part A*, under review.

involves scission of polymer backbones and formation of monomers and oligomers, and erosion is a physical phenomenon designating the loss of material resulted from the monomers and oligomers leaving the matrix [6]. Polymer molecular weight (MW) change and mass loss are the two measures for quantifying degradation and erosion, respectively. Degradation and erosion are coupled to each other, and they collectively regulate the drug release rate in the PLGA stent coating [37]. Experimental studies have been carried out for studying and designing PLGA stent coatings [39, 43, 45, 97], which are based on the trial-and-error procedures. Complementarily, mathematical models could provide guidance in device design and optimization prior to or in concert with experimental procedures. While the literature is considerably rich in mathematical models for drug release from biodurable stent coatings (to name just a few, [51, 53, 55]), there is limited work in modeling biodegradable stent coatings for drug delivery.

Modeling the PLGA degradation and erosion is a prerequisite for drug release modeling, and mechanistic approaches are most commonly employed, as described in papers on PLGA-based drug delivery systems such as microspheres [73, 74]. A simple and convenient approach for describing degradation, or the molecular weight change, uses first-order degradation models [76-78, 98]. Some other models generate a system of equations for all polymer chain lengths and compute the whole molecular weight distribution [75, 99]. Such approaches have high computational costs and require very detailed information for model initialization. As an alternative, a moments model adopts a "shrinking core" approach to significantly reduce the number of equations [79]. The moments model was extended by adding a monomer diffusion term for capturing the transition between reaction-controlled and diffusion-controlled states [80]. A limitation of

the moments model is often the closure problem of second or higher order moments, which requires advanced treatment [100, 101]. PLGA erosion, or mass loss, is important but yet limited modeling works are available in the literature. Among those works, a combined bulk random scission and end scission model was proposed for explaining the measured molecular weight change and mass loss in PLGA microspheres [75]. A threshold of dissolvable oligomer size has been assumed in the calculation of the measured polymer molecular weight and weight loss [99].

The autocatalytic effect, which occurs due to accumulation of acidic monomers and small oligomers in the interior of the PLGA matrix and results in a heterogeneous degradation rate, is also included by adding an acid concentration dependency on the rate constants [83]. Assuming no mass loss and constant volume, a simple analytical expression for the number average molecular weight in autocatalytic hydrolysis has been derived [83]. A mass balance model was also developed for three species (polymer PLA, oligomer, and monomer) where the monomer was considered to contribute to the autocatalytic effect [82]. Existing treatments of autocatalytic effect are summarized in a recent review [102]. Although interesting, the application of PLGA stent coating typically has a small characteristic length for which spatial non-uniformity of proton distribution disappears and the autocatalytic effect was not observed [97].

Accompanied and facilitated by PLGA degradation and erosion, drug release undertakes significant impact from the changing properties of the polymer matrix (porosity and PLGA molecular weight) and such factors need to be captured in the diffusion drug transport. For heparin release in PLGA microsphere, the pore size was

modeled and an induction time for drug release was calculated [75]. The model, however, used constant drug diffusivity for its drug release calculation. While macromolecular hydrophilic drugs are limited by diffusion through the pore space, relatively smaller hydrophobic drugs could diffuse through both the PLGA matrix and the pore space.

Table 5.1 Diffusivity dependency on molecular weight in literature models

Model Expression		Reference
$D(M) = D_0 \frac{M_0}{M}$	(5-1)	Charlier et al. [76]
$D(M_w) = D_0 + \frac{k}{M_w}$	(5-2)	Siepmann and Peppas [77]
$\ln D = -0.347x^3 + 01.394x^2 - 104.950x + 316.950$ $x = \ln M_w$	(5-3)	Raman et al. [78]
$D(M_n) = D_0 - k \ln M_w$	(5-4)	Wada et al.[84]

Several models have considered an effective drug diffusivity dependent on polymer molecular weight change (summarized in Table 5.1) [37]. The diffusivity was considered as being inversely proportional to the polymer molecular weight in an pseudo-steady state model for mifepristone release from PLGA films [76]. An inversely linear relationship between diffusivity and polymer molecular weight was also used [77, 98]. In a piroxicam release model, an empirical correlation was proposed by determining drug diffusivity in monodisperse PLGA microspheres with different molecular weights [78]. A similar approach was also used for determining a correlation between initial PLA molecular weight and apparent drug diffusivity [84]. Exponential dependency of the

diffusivity on the concentration of non-degraded PLA was also seem [82]. The aforementioned models, however, have not considered the contribution in the enhanced drug diffusion through erosion and increasing porosity.

A predictive model should take into account the coupled aspects of PLGA degradation, erosion, and drug release while maintaining the mathematical form as simple as possible. In this work, a PLGA degradation-erosion model is proposed based on the method of moments, from which an analytical solution for the PLGA mass loss (erosion) rate is derived. The degradation-erosion model predicts the molecular weight change and mass loss reported in different experiments. Drug transport in the PLGA coating is modeled by utilizing a varying effective diffusivity that incorporates the effects of PLGA molecular weight change, porosity change, and drug partitioning in the solid and liquid-filled pores to describe simultaneous transport through the polymer solid and the pore space. The coupled degradation-erosion model and the drug release model is solved and validated for *in vitro* sirolimus release data using model parameter values reported in the literature. The release model is also formulated as a parameter estimation problem and solved via optimization to obtain the parameters with the best fit. Parameter exploration in the model is also performed to investigate the impact on changing the release profiles.

5.2 Theory and Methods

Drug release from a PLGA stent coating is a joint outcome of drug diffusion and the coating degradation and erosion. Both biphasic and triphasic release profiles are observed, with the latter having an additional phase of initial burse release. Burst release is typically

found in large devices, which has been attributed to non-encapsulated drug or drug on the surface. The burst effect is conveniently removed through adjusting the fabrication technique and is not considered in this model [102].

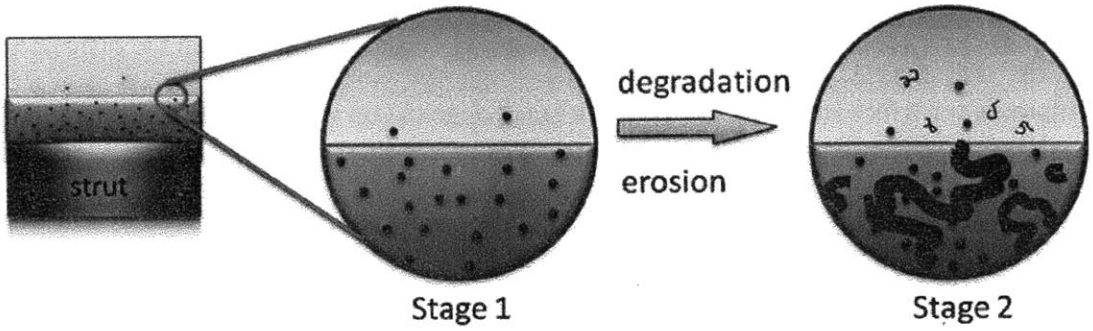

Figure 5.1. Two-stage scheme of coupled PLGA degradation, erosion, and drug release. Stage 1: slow release by diffusion through the matrix; Stage 2: enhanced released contributed by diffusion through both matrix and micro-porous structured formed by polymer matrix degradation and erosion.

The mathematical model focuses on the two releasing stages that are characteristic to PLGA drug release systems, involving an initial slow release and an enhanced release (Figure 5.1). The slow release (Stage 1 in Figure 5.1) is contributed by drug diffusion through the PLGA polymer solid phase at early times. For macromolecular drug, the diffusion release can be negligible due to small drug diffusivity. As polymer degradation continues and erosion start to occur with smaller products diffusing out of the matrix, pores are formed and opened up within the coating. Drug diffusion is accelerated by partitioning into and passing through the liquid-filled pores. Meanwhile, the molecular weight of PLGA polymers also decreases as a result of the degradation. Less molecular entanglement is present in the shorter PLGA chains, and drug diffusion

through the PLGA polymer phase is also enhanced. Combining the drug diffusion enhancement from both pores and reduced PLGA chain length, a faster release (Stage 2 in Figure 5.1) is observed.

Heterogeneous degradation and erosion could occur in Stage 2 when the diffusion distance is relatively large and diffusion for small degradation products is slower than the generation rates. The accumulation of the acidic degradation products (in particular monomers) can increase towards the interior of the PLGA device, to further catalyze degradation. This phenomenon, known as the size-dependent autocatalytic effect, leads to spatial non-uniformity and increases the complexity of drug release modeling. In the context of a stent coating, the coating thickness is on the order of 10 microns, which is small enough that the autocatalytic effect does not need to be considered [10].

Two key components in modeling drug release from PLGA stent coating are (1) capture of PLGA matrix change (porosity and PLGA molecular weight due to degradation and erosion, respectively) and (2) description of the effective diffusivity varying with the matrix evolution. Increasing porosity and decreasing molecular weight change the drug diffusion rate, and collectively contribute to simultaneous drug diffusion through the solid and porous phases. These aspects are modeled in the next two subsections, respectively.

5.2.1 PLGA Degradation and Erosion Model

The degradation reaction of PLGA polymer P_n of length n (number of monomer units) is described by

$$P_n \xrightarrow{k} P_i + P_{n-i} \tag{5-5}$$

where k is the reaction rate constant. The reaction assumes that the breakage of chemical bonds is random. Each polymer P_n can be generated via degradation of longer chains and consumed by breaking down into smaller chains.

In a PLGA stent coating, the change of polymer of length i is described by the diffusion-reaction Equation 5-6,

$$\frac{\partial P_i}{\partial t} = \frac{\partial}{\partial x}\left(D_i(M_w, \phi)\frac{\partial P_i}{\partial x}\right) + k(x)\left(-(i-1)P_i + 2\sum_{j=i+1}^{\infty} P_j \right) \tag{5-6}$$

where P_i is the concentration of polymer of length i, D_i is the effective diffusivity, and x is the coating thickness. The diffusivity of each polymer, D_i, is distinguished for different i, and is dependent on the average PLGA molecular weight M_w and matrix porosity ϕ. The reaction term describes all possible generation/consumption of polymer chains. In general the rate constant k can vary with position. For example, in the autocatalytic scenario, rate constant $k(x)$ is an explicit function of local proton concentration. Equation 5-6 is the general model form for describing the PLGA degradation and erosion process.

Modeling the stent coating using the full complexity of model Equation 5-6 for all polymer lengths is unrealistic, due to the complicated imperfectly known dependencies of diffusivity and rate constants on other factors, and computationally expensive, as a result of the huge number of partial differential equations. Existing models all utilize

simplifications by adopting various assumptions. The two main assumptions of our model are:

1. The diffusion of monomers (or neutralizing ions from the release buffer, if any) is fast at the length scale of the stent coating and therefore the pH gradient within the coating is negligible. As a result, the degradation reaction occurs homogeneously throughout the coating. This assumption eliminates the spatial dependency of rate constant k.
2. Because of their smaller size, the monomers diffuse through the coating much faster than the oligomers, and contributes to majority of the mass loss (erosion) in early times. Based on this fact, the second assumption considers that all monomers, and only monomers, contribute to mass loss at early times before disintegration of the coating matrix occurs.

Under the second assumption, the diffusion terms in Equation 5-6 for all polymer lengths can be separated from the degradation reaction. Leaving only the reaction terms in the equation, the model reduces to a set of ordinary differential equations that can be conveniently transformed utilizing the method of moments (see Appendix A for detailed description). With μ_n defined as the nth moment, the moments model is

$$\frac{d\mu_0}{dt} = k\left(\mu_1 - \mu_0\right) \tag{5-7}$$

$$\frac{d\mu_1}{dt} = 0 \tag{5-8}$$

$$\frac{dP_1}{dt} = 2k\left(\mu_0 - P_1\right) \tag{5-9}$$

where μ_0 stands for the total concentration (number) of polymer chains, μ_1 is the total mass (or total number of polymeric units) without consideration of mass loss, and P_1 is the concentration of monomers. Observe that μ_1 is a constant in Equation 5-8.

The moment model can be analytically solved to obtain (see Appendix A for the derivation),

$$\mu_0 = \mu_1 + \mu_1\left(\frac{1}{M_{n,0}} - 1\right)e^{-kt} \tag{5-10}$$

$$P_1 = \mu_1 + \mu_1\left(1 - \frac{2}{M_{n,0}}\right)e^{-2kt} + 2\mu_1\left(\frac{1}{M_{n,0}} - 1\right)e^{-kt} \tag{5-11}$$

where $M_{n,0}$ is the initial number-average molecular weight (MW). From Assumption 2 and the assumption that the weight change induced by the addition of water molecules is negligible compared to the weight of polymer, the fraction of mass loss, or erosion rate, is calculated by

$$r_{ML} = \frac{P_1}{\mu_1} = 1 + \left(1 - \frac{2}{M_{n,0}}\right)e^{-2kt} + 2\left(\frac{1}{M_{n,0}} - 1\right)e^{-kt} \tag{5-12}$$

By definition, the number-average MW is given as the total number of monomer units divided by the total number of chains,

$$M_n = \frac{\mu_1}{\mu_0} = \frac{1}{1+\left(\frac{1}{M_{n,0}}-1\right)e^{-kt}} \tag{5-13}$$

As time t approaches infinity, Equation 5-13 indicates that the number-average MW approaches one, which corresponds to complete degradation. Considering the loss of monomers, the modified number-average MW is

$$M_n = \frac{\mu_1 - P_1}{\mu_0 - P_1} = 1 + \frac{1}{1 - \frac{M_{n,0}-2}{M_{n,0}-1}e^{-kt}} \tag{5-14}$$

The weight-average MW is, however, not solved by the moments model because of the closure problem encountered on the second moment (illustrated in Appendix A). Alternatively, the commonly used first-order degradation model is adopted for modeling the weight-average MW change,

$$M_w = M_{w,0}\, e^{-k_w t} \tag{5-15}$$

where $M_{w,0}$ is the initial weight-average MW.

5.2.2 Drug Transport Model

The drug transport in the coating proceeds by diffusion mechanism. Assuming that the drug is uniformly dispersed in the coating, the drug release is described by

$$\frac{\partial C}{\partial t} = \frac{\partial}{\partial x}\left(D_e\left(M_w, \phi\right)\frac{\partial C}{\partial x}\right) \tag{5-16}$$

where D_e is the effective drug diffusivity that is dependent on the evolving molecular weight and porosity.

As a consequence of the degradation and erosion, the key in predicting the drug release is finding a good description of the evolving effective diffusivity. As mentioned in the introduction, existing models typically consider only part of the affecting factors empirically (e.g., influence of molecular weight change, Table 5.1). In this model, an effective drug diffusivity is derived that incorporates the diffusivity in the polymer phase (D_s), the diffusivity in the liquid-filled pores (D_l), porosity (ϕ), and drug partitioning between the liquid-filled pores and solid PLGA phase (κ):

$$D_e = \frac{(1-\phi)D_s + \kappa\phi D_l}{1-\phi+\kappa\phi} \tag{5-17}$$

where the derivation is in Appendix B. The diffusivity in the polymer phase (D_s) further depends on the changing molecular weight. The various models summarized in Table 5.1 all correspond to this particular aspect. According to reptation theory in polymer physics, this diffusivity correlates with the average molecular weight (e.g., weight-average MW) through the scaling law [103],

$$D_s = D_{s0}\left(\frac{M_w}{M_{w,0}}\right)^{-\alpha} \tag{5-18}$$

with a theoretical value of power α equal to 2.

A comparison of the power law model (5-18) with the literature fit in model (5-3) is illustrated in Figure 5.2 for initial diffusivities measured in piroxiam-releasing

monodisperse PLGA microspheres. The power law model (5-18) matches the experimental data with $\alpha = 1.714$ and $R^2 = 0.9999$. Extending the models to the low molecular weight region, the predicted diffusivity is much more reasonable for the power law model (5-18) and stays within the physical range. Based on the analysis, the power law model (5-18) is adopted for modeling D_s.

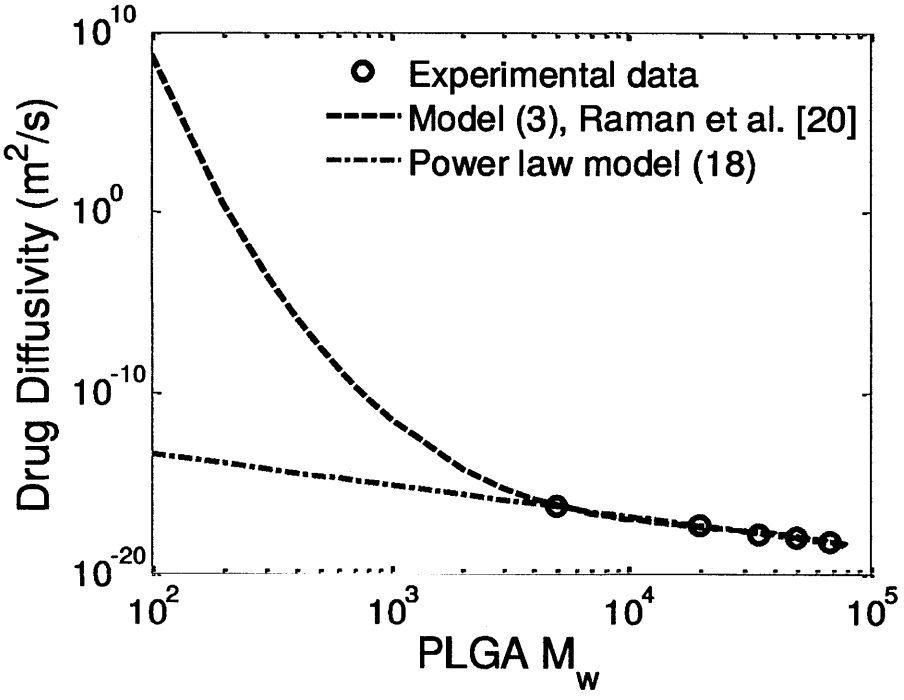

Figure 5.2 Estimation of the dependency of drug diffusivity in the polymer phase on the PLGA average molecular weight. The power law model gives a more physically reasonable prediction at low molecular weights than the model (Equation 5-3).

Equation 5-17 can be verified with two simple scenarios. When no pores exist, or $\phi = 0$, the expression reduces to D_s, which is the drug diffusivity in the polymer solid. At

the other extreme with the porosity of one, or $\phi = 1$, the expression reduces to the aqueous drug diffusivity D_l.

A quick note is that in Equation 5-17, the effect of geometric factors was not included. Such factors include the tortuosity, which describes how tortuous the pore connections are, and constrictivity, which is a hindering effect if the pore size is comparable to the drug molecule size [85, 87]. Parameters for such factors are typically empirical, and could be incorporated with existing formulas [86]. In this work, the factors of tortuosity and constrictivity are assumed constant. According to the knowledge of the authors, this is the first time in the literature that such an effective diffusivity formula is developed to describe simultaneous drug transport through degrading polymers and eroding pores in a stent coating, while taking into account the key controlling factors.

5.3 Results and Discussion

In this section, the degradation and erosion model as well as the drug release model are validated by comparing with experimental data reported in the literature. Three distinguished experiments independently done in different groups are utilized for model validation. The information of the three sets of experiments are labeled and summarized in Table 5.2.

Table 5.2 Sources and information of the experimental data used for model validation

Label	PLGA Composition (LA:GA)	PLGA weight-average MW	Reference
Dataset 1	50:50	37954	Batycky et al. [75]
Dataset 2	53:47	7.69×10^4	Wang et al. [45]
Dataset 3	Unreported	Unreported	Xi et al. [97]

5.3.1 Predicting PLGA Erosion

The erosion model as derived in Equation 5-12 describes the mass loss as a function of time and initial number-average MW. The model parameter, degradation rate constant k, is determined from the half-time of the number-average molecular weight decay. A reported value in the literature is used, with $k = 2.5 \times 10^{-7} s^{-1}$ (half-time is 35 days) [75]. The measured mass loss in all the three datasets falls on the model prediction (Figure 5.3).

It is interesting to note that, even though the initial PLGA number-average MW is different in all three data sets, their model predictions overlap. The explanation lies in the insignificance of the term $1/M_{n,0}$ compared with 1 in Equation 5-12, due to the typical large initial number-average MW in PLGA polymers. Consequently, Equation 5-12 is further simplified as

$$r_{ML} = 1 + e^{-2kt} - 2e^{-kt} \tag{5-19}$$

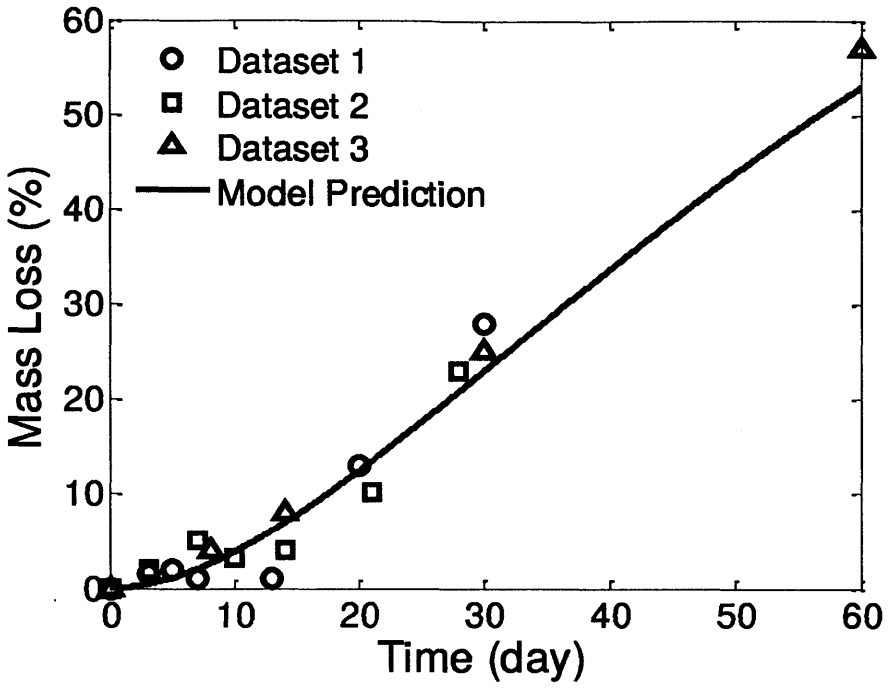

Figure 5.3 Weight loss predicted by the analytical erosion model matched the three experimental datasets.

To the knowledge of the authors, it is the first time in the literature that an analytical model is proposed for describing mass loss in PLGA polymer thin films.

5.3.2 Predicting PLGA Degradation

In theory either the number-average MW or weight-average MW can be used for characterizing the degradation. Compared with weight-average MW, the number-average MW is significantly affected by the presence of low MW polymers such as monomers and oligomers. The low MW polymers are, however, difficult to be detected due to the resolution limitation of equipments. As a result, the number-average MW measurements in PLGA degradation only represents contributions from polymers with size larger than

the lower detection limit [75]. The limit for PLGA is suggested to be oligomers with 9 polymeric units. As a result, the comparison of the number-average MW model (Equations 5-13 & 5-14) with experiments becomes difficult. As expected, model equations would predict much faster decay in number-average MW than what would be observed in experimental measurements.

Experimental determination of the weight-average MW is more robust as it is less influenced by the exclusion of small degradation products in the measurement. In the weight-average MW model, as described in Equation 5-15, the model parameter k_w is distinguished with parameter k used in the erosion model and the number-average MW change. While k corresponds to the reaction rate constant and is estimated via the half-time for the decay of the number-average MW, k_w is conveniently obtained through the half-time for weight-average MW decay. The k_w is acquired as $k_w = 7.5 \times 10^{-7} \mathrm{s}^{-1}$ through the same experimental source for k [75]. Similar values are reported in other experimental studies [78, 98].

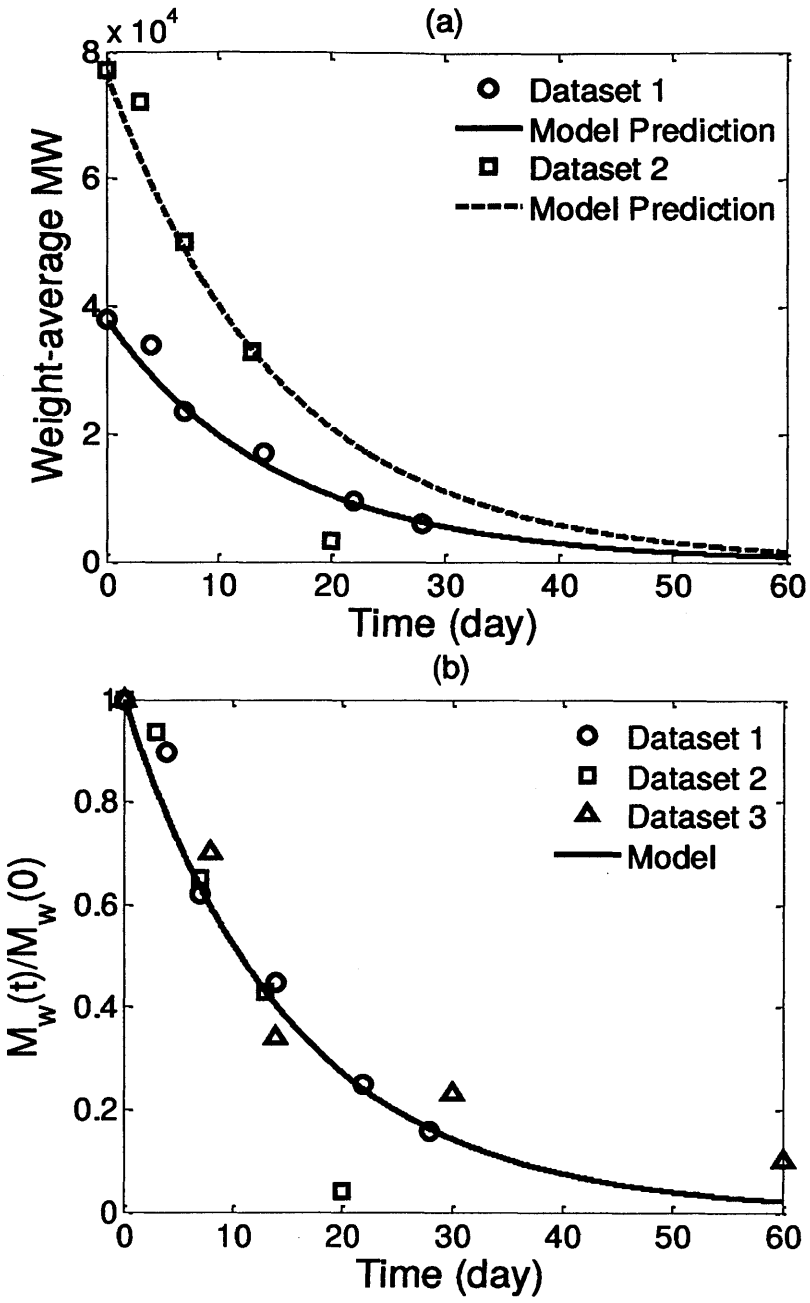

Figure 5.4 Molecular weight change predictions using the degradation model. (a) Model prediction for weight-average MW in data set 1 and data set 2. (b) Normalized weight-average MW in all three data sets compared with model prediction.

The degradation model predicting the weight-average MW is compared with the experimental datasets in Figure 5.4. Figure 5.4(a) plots the experimental measurements for two data sets. The model predictions are nearly perfect for data set 1, from which the model parameter k_w was determined. The model predictions for data set 2 are satisfactory except for Day 20, where the particular data point is much lower than the model prediction. While the abrupt drop is proposed to be associated with the increase in mass loss at the same time point [45], the occurrence is unclear as no measurement was available for later times. The normalized molecular weight change is plotted for all three datasets in Figure 5.4(b). For data set 3, although the initial molecular weight is unknown, the model predicts the molecular weight change fairly well for the entire time course up to 60 days.

5.3.3 Predicting Sirolimus Release from PLGA Coating

To model the drug release, the effective drug diffusivity (4-17) requires information input for average MW and porosity. The average MW can be directly obtained via incorporating the validated first-order degradation model in the previous section. By assuming constant volume of the coating matrix and the same density for PLGA polymers of different lengths, the porosity is related to the mass loss (4-19) via

$$\phi = \phi_0 + \left(1-\phi_0\right)\left(1+e^{-2kt}-2e^{-kt}\right) \tag{4-20}$$

where ϕ_0 is the initial porosity.

The complete set of equations for describing the drug release is summarized in Table 5.3 for clarity. As a demonstration, the model is solved for predicting *in vitro*

sirolimus release from PLGA stent coating. The wash out boundary condition is utilized on the external surface of the stent coating. The initial porosity is assumed to be zero. As both sirolimus and piroxiam are hydrophobic drugs with small molecule size, the power law model (5-18) for D_s and $\alpha = 1.714$ are adopted for modeling sirolimus from Section 2.1.

Table 5.3 Summary of complete set of equations for the drug release model

Drug Transport	$\frac{\partial C}{\partial t} = \frac{\partial}{\partial x}\left(D_e\left(M_w, \phi\right)\frac{\partial C}{\partial x}\right)$	(5-16)
Effective diffusivity	$D_e = \frac{(1-\phi)D_s + \kappa\phi D_l}{1-\phi+\kappa\phi}$	(5-17)
Diffusivity in polymer solid	$D_s = D_{s0}\left(\frac{M_w}{M_{w,0}}\right)^{-\alpha}$	(5-18)
PLGA average MW	$M_w = M_{w,0}\,\mathrm{e}^{-k_w t}$	(5-15)
Porosity change	$\phi = \phi_0 + \left(1-\phi_0\right)\left(1+e^{-2kt}-2e^{-kt}\right)$	(5-20)

The model is solved using the numerical method of lines. The spatial dimension (x) is discretized, which results in a system of ordinary differential equations (ODE). The system of ODEs is conveniently solved using a standard ODE solver in Matlab (ode15s). The numerical procedure is straightforward and details are not included here [104].

Sirolimus release of two loadings (1% and 2% loadings) was used for comparison (Figure 5.5). The predicted sirolimus release in the model matches the experimental data quite closely. Because the loadings are relatively low, the drug could be considered as in

a dissolved state. As a result, the percentage release profiles overlap for the two loadings both experimentally and in the model. Only three parameters are used in the drug release model: the drug diffusivity in the initial PLGA solid (D_{s0}), aqueous drug diffusivity (D_{l0}), and drug partitioning coefficient (κ). The values of the parameters are directly obtained from ranges reported in the literature (summarized in Table 5.4). The model predictions capture the biphasic release behavior, and describes the process of simultaneous diffusion through polymer solids and the liquid-filled pores.

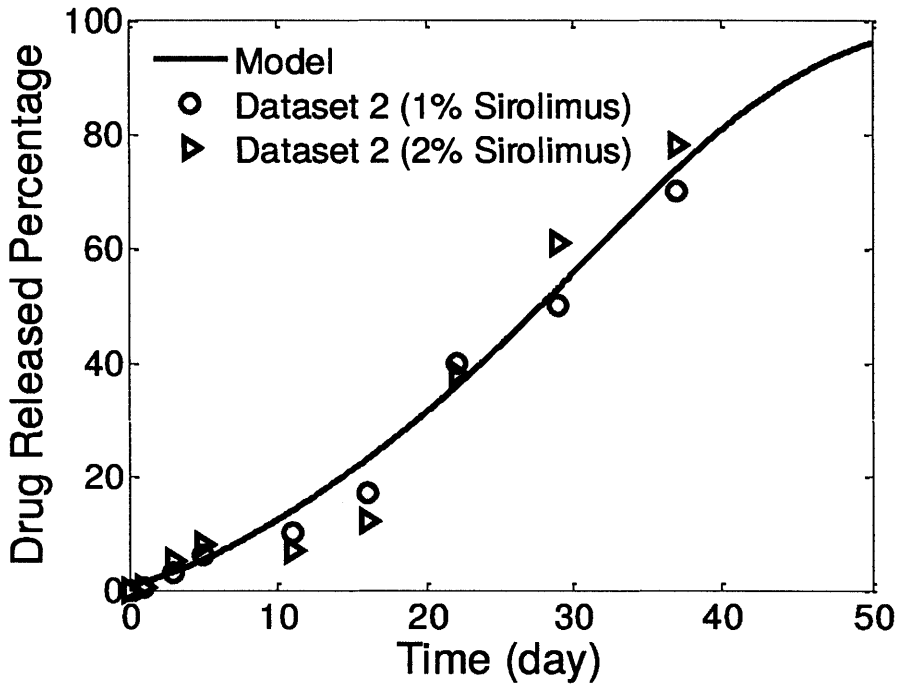

Figure 5. 5 Model prediction matches experimental data of sirolimus release from PLGA coating.

In order to obtain the parameters that best fit the experimental data, the model is also formulated as a parameter estimation problem. The parameter estimation defines an

objective function that minimizes the summed square error (SSE) between values of model predictions and experimental data,

$$SSE = \min\left\{\sum(\text{Model Prediction} - \text{Data})^2\right\} \tag{5-20}$$

and is conveniently solved using the optimization toolbox (fmincon) in Matlab. The parameter values obtained via optimization are very close to the initial values used in the model (Table 5.4). The small difference indicates that the parameter values are optimal and further supports the validity of the model.

Table 5.4 Model parameters and estimated values via optimization

Model Parameters	Initial Values	Estimation via Optimization	Reference Range
Partition coefficient κ	10^{-4}	1.0035×10^{-4}	10^{-6} ~ 10^{-3} [105, 106]
Initial diffusivity in PLGA polymer $D_{s0}(\mu m^2/s)$	10^{-5}	9.9826×10^{-6}	10^{-6} ~ 10^{-4} [78, 98]
Diffusivity in aqueous phase $D_{l0}(\mu m^2/s)$	50	49.6386	10 ~ 10^3 [103]
MW change model parameter a	1.714	1.7179	~2 [103]

The drug release model in this work is also compared with existing models (Figure 5.6). Using a constant diffusivity in the polymer coating results in a very limited release. Including the MW dependency in the diffusivity results in significant

enhancement in the drug release. However, the discrepancy between that model and our model indicates that the contribution from diffusion through the pores described in our model is significant. As the comparison suggests, the simultaneous diffusion through the polymer solid and the pore space is the most appropriate mechanism for describing sirolimus release in PLGA stent coating, and is only captured in our proposed model.

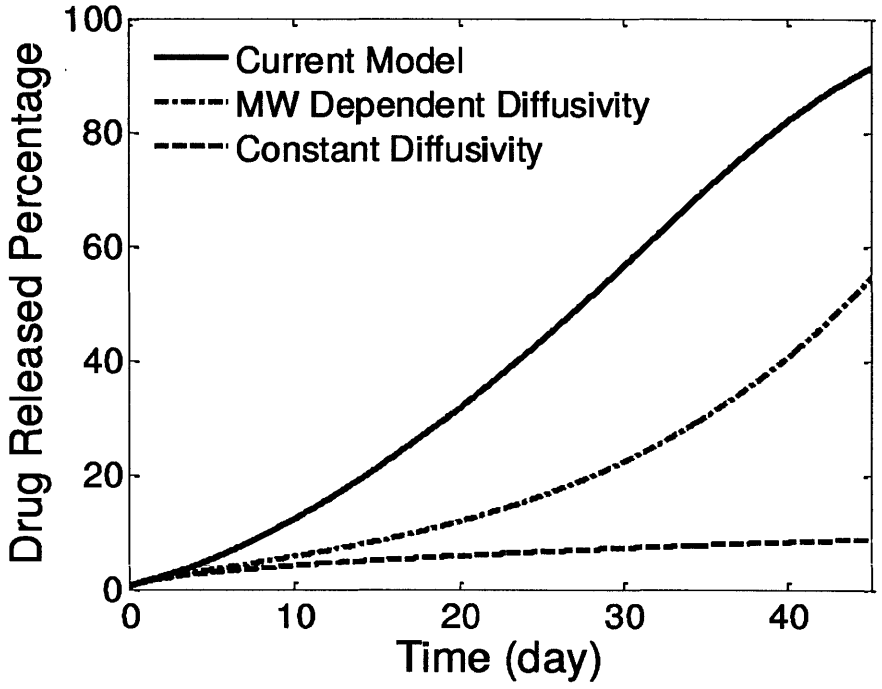

Figure 5.6 Sirolimus release profiles predicted in different models.

5.3.4 Analysis of the Hydrophobicity Parameter on Release Rate

The partitioning coefficient (κ) reflects the hydrophobicity of the drug. The smaller the partition coefficient, the less water-soluble the drug is and the higher the tendency that the drug prefers to stay within the polymer solid. The effect of the partitioning coefficient is illustrated in Figure 5.7 by fixing the other parameters (e.g., drug diffusivities in the

polymer solids and aqueous phase). With higher partitioning coefficient value, faster release is predicted. The release profiles all exhibit biphasic characteristics. For all release profiles, the release profiles have the lower bound specified by the curve corresponding to $\kappa = 0$.

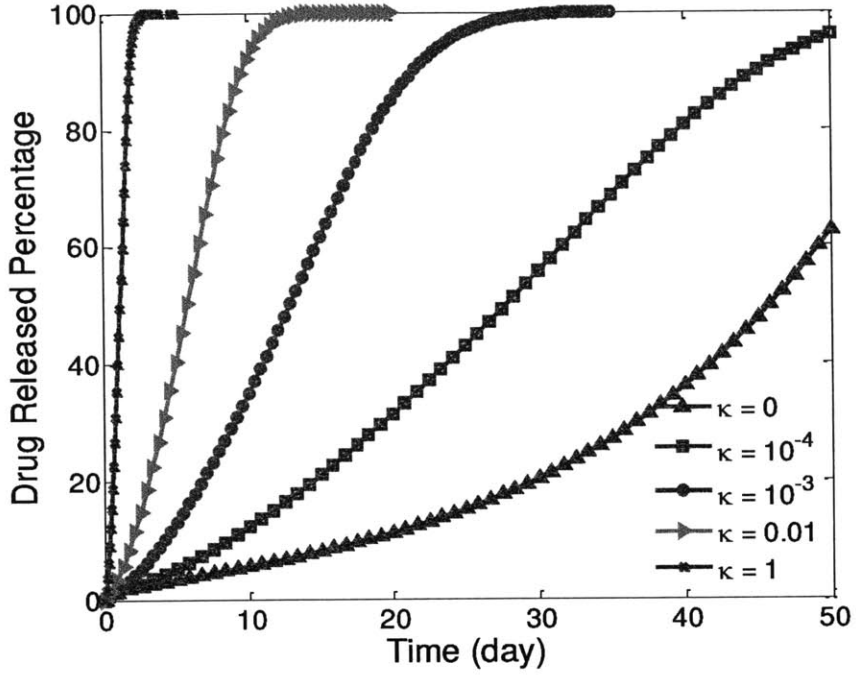

Figure 5.7. Impact of drug hydrophobicity on the drug release behaviors in PLGA stent coating.

5.3.5 Limitations and Possible Extensions of the Model

The model developed in this work considers the various important factors that collectively regulate the drug release in PLGA stent coatings. While demonstrating successful predictions, the model does have limitations and it is worthwhile for further

research in several aspects that could produce even better predictability and extended applicability.

The first limitation lies in the simplifications adopted in the development of the effective drug diffusivity. As pores are formed randomly throughout the polymer matrix, the path through the pores could zigzag and the tortuosity effect may be significant. Correspondingly, the diffusivity contribution corresponding to the pores would be reduced. This modification would correct the higher predicted release than measured data at times around 10 to 20 days in Figure 5.5. Usually included as an empirical factor, the tortuosity effect could be potentially incorporated if sufficient information was available.

While this work focuses on hydrophobic drug with relatively small size, which are typically used in drug-eluting stent applications (i.e., sirolimus, with MW of less than 1 kDa), the model application could be extended to the release of macromolecular hydrophilic drugs (such as proteins or genes). In such situations, another factor besides the tortuosity effect, called *constrictivity*, would become important. The constrictivity describes the delay and hindrance in diffusion through pores when the pore size is comparable to the drug molecule size, and expressions for describing the factor are available. As a result, utilization of the constrictivity effect would require knowledge of the pore sizes in the coating.

In the erosion model, only monomers were included as the source for weight loss so that simple analytical expression could be derived. In reality, dimers, trimers, and other oligomers may all contribute to the weight loss to varying extents. Even though treated with simplification in this work, the autocatalytic effect could have some

influence in PLGA stent coating systems. Capture of those details in the degradation and erosion model may offer extra benefits in improving the drug release prediction.

5.4 Conclusions

This chapter develops a complete model set for describing the PLGA degradation and erosion and coupled drug release from PLGA stent coating. An analytical and simple expression for the PLGA mass loss was derived for the first time in the literature, as well as analytical expression for the number-average MW change. The mass loss model and the first-order degradation model are validated with experimental data from the literature.

Simultaneous drug diffusion through polymer solid with changing average MW and liquid-filled pores was modeled, and an effective drug diffusivity model was derived taking into account various factors including polymer MW change, diffusivity in the polymer, diffusivity in the liquid-filled pores, and drug partitioning between solid and liquid phases. The model was demonstrated for sirolimus release from PLGA stent coating and predicted experimental data in the literature. Comparison of the proposed model with existing models revealed the significance of simultaneous sirolimus diffusion through polymer solid and pore space. The impact of drug hydrophobicity was also demonstrated using the model.

The mechanistic model developed here has potential for application to the design of PLGA coatings for drug-eluting stents. The model can also be extended for applications to other PLGA-based drug delivery systems. The limitations are also discussed that provides guidance in possible model improvements.

5.5 Appendix A. Derivation of the Differential Moment Equations

Under the assumptions in Section 2, the partial-differential equations are reduced to ordinary differential equations. The change of polymers of different length is given by,

$$\frac{dP_1}{dt} = 2k_n \sum_{j=2}^{N} P_j \tag{5-A1}$$

$$\frac{dP_2}{dt} = -k_n P_2 + 2k_n \sum_{j=3}^{N} P_j \tag{5-A2}$$

$$\frac{dP_3}{dt} = -2k_n P_3 + 2k_n \sum_{j=4}^{N} P_j \tag{5-A3}$$

$$\vdots$$

$$\frac{dP_i}{dt} = -(i-1)k_n P_i + 2k_n \sum_{j=i+1}^{N} P_j \tag{5-A4}$$

$$\vdots$$

$$\frac{dP_{N-2}}{dt} = -(N-3)k_n P_{N-2} + 2k_n \sum_{j=N-1}^{N} P_j \tag{5-A5}$$

$$\frac{dP_{N-1}}{dt} = -(N-2)k_n P_{N-1} + 2k_n P_N \tag{5-A6}$$

$$\frac{dP_N}{dt} = -(N-1)k_n P_N \tag{5-A7}$$

Define the *n*th moment of the polymers as

$$\mu_n = \sum_{i=1}^{N} i^n P_i \tag{5-A8}$$

Physically, the zeroth moment corresponds to the total number of polymers in the system, while the first moment stands for conservation of polymer units.

Summing all equations (5-A1)–(5-A7) gives an equation for the zeroth moment,

$$\frac{d\mu_0}{dt} = \frac{d\sum_{i=1}^{N} P_i}{dt} = k_n \sum_{j=2}^{N} (j-1)P_j = k_n \left(\sum_{j=1}^{N} jP_j - \sum_{j=1}^{N} P_j \right) = k_n (\mu_1 - \mu_0) \tag{5-A9}$$

Similarly, the first moment is given by

$$\frac{d\mu_1}{dt} = \frac{d\sum_{i=1}^{N} iP_i}{dt} = -k_n \sum_{j=2}^{N} j(j-1)P_j + 2k_n \sum_{j=2}^{N} [1 + \cdots + (j-1)]P_j = 0 \tag{5-A10}$$

which implies that μ_1 is a constant.

The change of monomer is described by

$$\frac{dP_1}{dt} = 2k_n (\mu_0 - P_1) \tag{5-A11}$$

The second moment can be derived as

$$\frac{d\mu_2}{dt} = k_n \left(\frac{1}{3}\mu_1 - \frac{1}{3}\mu_3 \right) \tag{5-A12}$$

However, it is clear that the equations for the higher order moments do not have closure (that is, the differential equations for the *i*th moment are algebraic functions of higher order moments).

With initial condition $\mu_0(t=0) = \mu_1/M_{n,0}$, where $M_{n,0}$ is the initial number-average molecular weight, and $P_1(t=0) = 0$, Equations (5-A9) and (5-A11) are analytically solved to give

$$\mu_0 = \mu_1 + \mu_1\left(\frac{1}{M_{n,0}} - 1\right)e^{-kt} \tag{5-A13}$$

$$P_1 = \mu_1 + \mu_1\left(1 - \frac{2}{M_{n,0}}\right)e^{-2kt} + 2\mu_1\left(\frac{1}{M_{n,0}} - 1\right)e^{-kt} \tag{5-A14}$$

5.6 Appendix B. Derivation of the Effective Drug Diffusivity

Consider one-dimensional transport in a small control volume consisting of polymer matrix and pore space (Figure 5.B1). The drug transport is contributed by both diffusion through the pore space and diffusion through the polymer solid.

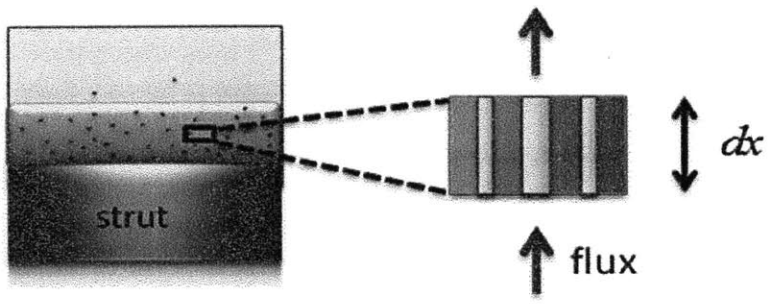

Figure 5.B1. Illustration of one-dimensional drug diffusion through pores and polymer solid in a small control volume.

The drug transport through the polymer solid is given by

$$\frac{\partial((1-\phi)VC_S)}{\partial t} = (1-\phi)AD_S\nabla C_S\Big|_{x=x}^{x=x+\Delta x} - A'J_{SL} \qquad \text{(5-B1)}$$

and the drug transport through the pore space is given by

$$\frac{\partial(\phi VC_L)}{\partial t} = \phi AD_L\nabla C_L\Big|_{x=x}^{x=x+\Delta x} + A'J_{SL} \qquad \text{(5-B2)}$$

where A' is the interface area between the solid and pore space within the micro control volume, J_{SL} is the flux through the solid and liquid interface, and C_S and C_L denotes the concentration within the polymer solid and the liquid filled pores, respectively.

Summing Equations 5-B1 and 5-B2 gives an expression for the total drug diffusion,

$$V\left(\frac{\partial((1-\phi)C_S)}{\partial t} + \frac{\partial(\phi C_L)}{\partial t}\right) = A\left((1-\phi)D_S\nabla C_S\Big|_{x=x}^{x=x+\Delta x} + \phi D_L\nabla C_L\Big|_{x=x}^{x=x+\Delta x}\right) \qquad \text{(5-B3)}$$

Note that the interfacial diffusion terms cancel due to the opposite signs. Assuming that the drug is in partitioning equilibrium between the pore phase and solid polymer phase gives

$$C_L = \kappa C_S \qquad \text{(5-B4)}$$

where κ is the partition coefficient. Substituting Equation 5-B4 into 5-B3 gives

$$V\left(\frac{\partial\left((1-\phi)C_S + \phi C_L\right)}{\partial t}\right) = A\left((1-\phi)D_S + \kappa\phi D_L\right)\nabla C_S\Big|_{x=x}^{x=x+\Delta x} \qquad \text{(5-B5)}$$

The average drug concentration over the entire control volume is given by

$$C_{ave} = (1-\phi)C_S + \phi C_L \tag{5-B6}$$

As ϕ is only a function of time (uniform degradation throughout the coating),

$$\nabla C_{ave} = (1-\phi+\phi\kappa)\nabla C_S \tag{5-B7}$$

Substituting 5-B6 and 5-B7 into 5-B5 gives

$$V\frac{\partial C_{ave}}{\partial t} = A\left(\frac{(1-\phi)D_S + \kappa\phi D_L}{1-\phi+\kappa\phi}\right)\nabla C_{ave}\Big|_{x=x}^{x=x+\Delta x} \tag{5-B8}$$

For infinitesimal Δx,

$$\frac{\partial C_{ave}}{\partial t} = \left(\frac{(1-\phi)D_S + \kappa\phi D_L}{1-\phi+\kappa\phi}\right)\nabla^2 C_{ave} \tag{5-B9}$$

Correspondingly, the average concentration in the coating is described by

$$\frac{\partial C_{ave}}{\partial t} = D_e \nabla^2 C_{ave} \tag{5-B10}$$

where D_e is the effective diffusivity defined as

$$D_e = \frac{(1-\phi)D_S + \kappa\phi D_L}{1-\phi+\kappa\phi} \tag{5-B11}$$

CHAPTER 6

INTEGRATED MODEL FOR INTRAVASCULAR DRUG DELIVERY FROM A PLGA-COATED STENT[3]

6.1 Introduction

Drug-eluting stents are commonly used in the coronary angioplasty procedures to both provide structural support and release drug molecules locally at the implanted arterial site for preventing adverse outcomes (such as in-stent restenosis) in the patients [9, 13, 95]. Biodurable (or non-erodible) polymers are the predominant type of stent coatings for carrying active drug compounds, whereas recent studies have suggested issues potentially related to the slow drug release in the biodurable coatings and the hypersensitivity to the permanent presence of polymer coating in the arterial wall [10, 18, 19, 34]. Improving the design and performance of drug-eluting stents is a long-term research topic. Among the various research directions, the utilization of biodegradable polymer coatings in place of the biodurable coatings has been proposed [20, 33]. In particular, biocompatible poly(lactic-co-glycolic acid) (PLGA), and allows tunable drug release rates based on different polymer molecular weights, has received a high amount of interest in ongoing drug-eluting stents research [39, 40, 43, 45, 47]. While most studies were carried out for examination of release under *in vitro* conditions, further evaluation of PLGA stent coating for *in vivo* evaluations of implanted stents are necessary and are typically significantly more costly.

[3] Work published as: X. Zhu and R.D. Braatz, Modeling and analysis of drug-eluting stents with biodegradable PLGA coating, *Journal of Biomechanical Engineering*, 2014. doi:10.1115/1.4028135

Mathematical models and simulations have been widely employed in the research of drug-eluting stents ranging from *in vitro* drug release evaluation to intravascular delivery investigations. Especially, models for studying the intravascular drug delivery process can help to acquire detailed information about the drug release, delivery, and distribution into the arterial wall, and can provide additional insights into the stent-based drug delivery systems. Some models simplifies the stent coating into a source term for providing drug concentrations, and focus on investigating the arterial drug distribution surrounding the stent struts without explicitly modeling the drug transport in the stent coating. Such models were used in the analysis of convective and diffusive drug transport comparison in the arterial wall [55], mechanics of stent expansion and drug distribution [70], and impact of blood flow on drug deposition in the arterial wall [63, 67]. Other models have incorporated the biodurable coating to model the drug release from the coating and subsequent drug uptake in the arterial wall. In those models where the biodurable coating is explicitly modeled with a constant drug diffusivity, drug release and arterial drug distribution have been investigated considering the effects of drug diffusivities in the coating and in the arterial wall [54, 56, 107, 108], coating thickness [56], the strut embedment [54] and compression [109], reversible drug binding [65, 108], and multi-layer structure of the arterial wall [58, 59].

So far little modeling work has been published on intravascular drug delivery using biodegradable stent coatings. A degradable stent coating has been modeled by artificially switching the values of drug diffusivity in the coating reservoir based on a pre-defined drug concentration threshold [57], which does not mechanistically model the coating erosion process. While various models have been proposed for describing the *in vitro* drug release coupled with polymer degradation and/or erosion in PLGA drug delivery systems (for microspheres [37, 74, 102] and thin film stent coatings [82, 110]),

such mechanistic models have not been utilized to model the intravascular drug delivery from a PLGA stent coating.

This chapter presents a mathematical model that describes the integrated process of drug release in PLGA coating and subsequent drug delivery, distribution, and drug pharmacokinetics in the arterial wall. A mechanistic model for drug release in the PLGA coating is adopted that couples the drug diffusion to the PLGA degradation and erosion (Chapter 6, [110]), and the adopted model is integrated with an arterial wall model where the drug pharmacokinetics in the arterial wall is modeled as a reversible binding process (Chapter 5, [108]). The integrated model further incorporates drug internalization for cellular drug uptake, interstitial fluid flow, and strut embedment as model factors. For drug diffusion in the arterial wall, an anisotropic drug diffusivity is considered and is analytically calculated based on the structural properties of the arterial wall. The model is simulated using the finite element method. The simulations first compare the biodegradable PLGA coating with a biodurable coating for stent-based drug delivery. For a stent with PLGA coating, the model simulations further investigate the impact of drug internalization, interstitial fluid flow in the arterial wall, and stent embedment on drug release in the coating, arterial drug levels, and arterial drug distribution. Development of such a detailed integrated model helps to provide insights into the design and evaluation of biodegradable PLGA coated drug-eluting stents for intravascular drug delivery.

6.2 Model Development

In the model scheme, an implanted stent is studied in the artery where the stent struts are evenly placed in the cross-section of the lumen (Figure 6. 1(a)). The strut-arterial wall configuration is based on a previous study of a biodurable polymer coating carried out by the authors [108] and is typical for stents applications [55]. The blood flow is in the

direction into the paper plane. Typical square-shaped stent struts are considered [56, 58, 88]. Due to symmetry, a single stent strut with its surrounding arterial wall domain is extracted for the study to reduce computational cost. The extracted model domain is illustrated in Figure 6. 1(b), where half of the stent strut is embedded into the arterial wall. Different from the previous study of biodurable coatings in Chapter 5, here the curvature of the arterial wall is retained rather than simplified as being flat. The Cartesian coordinate system (noted as x, y) is used for describing the domains including the square-shaped stent strut and the stent coating, and the cylindrical coordinate (noted as r, θ) is adopted for the curved arterial wall domain.

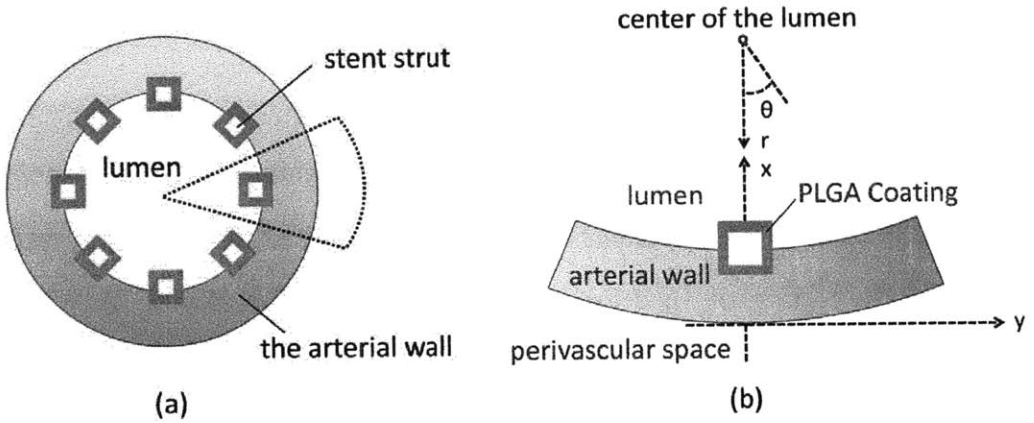

Figure 6.1 (a) Cross-sectional view of an implanted stent in a coronary artery. (b) Schematic of a single stent strut with PLGA coating half-embedded into the arterial wall. Cartesian coordinate (x, y) and cylindrical coordinate (r, θ) are both illustrated.

The mathematical models for important phenomena governing the drug delivery process are described in the following subsections. The model for describing drug transport in the biodegradable PLGA coating was adapted from Chapter 6, and the model for drug transport and pharmacokinetics in the arterial wall was developed based on

Chapter 5 for biodurable coating [108]. The integrated model provides a tool for evaluating PLGA-coated drug-eluting stents for intravascular drug delivery.

6.2.1 Drug Transport in the PLGA Coating

The drug release in the PLGA polymer coating is a process coupled to the degradation and erosion of the PLGA polymer matrix. Degradation represents the chemical process that breaks down the polymer chains and results in decreasing PLGA molecular weight, and erosion is the physical process characterized by the polymer mass loss [6]. Both degradation and erosion can facilitate drug molecule diffusion, as molecular weight reduction induces less entanglement of polymer chains in the PLGA bulk, and the mass loss creates pore space. For PLGA microsphere systems, a good number of mathematical models have been proposed in the literature to describe the degradation and erosion process of PLGA microspheres and to take into account the degradation and/or erosion contribution in the drug release process [37, 74, 102]. The proposed models typically incorporate a variable drug diffusivity that depends solely on the PLGA molecular weight change [76, 78, 84, 98]. An exponential dependency of drug diffusivity on the concentration of undegraded PLA was also seem in a model for PLA stent coating [82]. In a recent work of the authors, a model was proposed for drug release in PLGA stent coating that considers contributions to the effective drug diffusivity from both degradation and erosion of PLGA [110], where the importance of dual contributions in the effective drug diffusivity was validated and demonstrated for *in vitro* sirolimus release from PLGA coating. The model is utilized here to describe the drug diffusion in the PLGA coating coupled to polymer degradation and erosion; readers interested in the detailed derivation of the mathematical model are referred to [110].

The drug diffusion through both the polymer bulk with decreasing PLGA molecular weight and the pore space with increasing pore volume fraction in the matrix is described by incorporating an effective drug diffusivity. The drug transport in the PLGA coating is modeled by

$$\frac{\partial C}{\partial t} = D_{1,e}\frac{\partial^2 C}{\partial x^2} + D_{1,e}\frac{\partial^2 C}{\partial y^2} \tag{6-1}$$

where $D_{1,e}$ is the effective drug diffusivity in the PLGA coating and is described by

$$D_{1,e} = \frac{(1-\phi)D_{s0}\left(M_w/M_{w0}\right)^{-a} + \kappa\phi D_{l0}}{1-\phi+\kappa\phi} \tag{6-2}$$

The effective diffusivity is a function dependent on the changing PLGA molecular weight M_w and the evolving coating porosity ϕ. D_{s0} is the initial drug diffusivity in the PLGA polymer before degradation, D_{l0} is the drug diffusivity in the aqueous phase, M_{w0} is the initial polymer molecular weight, a is the dependency of drug diffusivity on PLGA molecular weight, and κ is the drug partition coefficient between PLGA solid and aqueous phase (defined as concentration in aqueous phase divided by concentration in the solid phase at equilibrium).

The PLGA molecular weight change is described by a first-order decay model given by [76, 78, 98]

$$M_w = M_{w0}\mathrm{e}^{-k_w t} \tag{6-3}$$

The porosity change, which is related to the mass loss of the coating, was analytically derived as [110]

$$\phi = \phi_0 + (1-\phi_0)\left(1 + e^{-2k_n t} - 2e^{-k_n t}\right) \tag{6-4}$$

where ϕ_0 is the initial porosity in the PLGA polymer matrix and is assumed zero.

In Equations 6-3 and 6-4, the k_w and k_n are degradation rate constants corresponding to weight- and number-average molecular weight change, respectively, and their values were experimentally measured [75]. Equations 6-1 to 6-4 provide the complete set of equations for describing drug transport in the PLGA coating. As PLGA undergoes bulk erosion, the coating experiences mass loss while the integral structure is maintained. The coating structure has been reported to maintain integrity during the entire degradation period, until much later time after complete elution of the loaded drug [47]. Therefore, the coating domain can be considered as intact for the time span of interest.

6.2.2 Drug Transport in the Arterial Wall

Once released into the arterial wall, the drug molecules are exposed to the physiological environment in the arterial wall. While drug molecules diffuse within the arterial wall, various drug-tissue interactions occur that affect the arterial wall drug transport, distribution, and drug uptake [25, 111]. The drug-arterial wall interaction has been commonly modeled as a reversible binding reaction of the drug molecules with binding sites present in the arterial wall, as shown in Equation 6-5 [57, 65, 108, 111]. In the process, bound drug C_B is formed by associating free drug C_F with the available binding sites S. The bound drug is immobilized and only the free drug can diffuse. The reversible binding process, however, does not provide a mechanism for drug consumption (e.g. drug uptake by tissue cells), which can be characterized by drug internalization [112-114]. To take this factor into account, drug internalization (Equation 6-6) is modeled in this model

which assumes that, once drug molecules are associated with binding sites, the cells take up and metabolize drug molecules as a first-order reaction. The internalization step, as a result, regenerates a binding site S for every internalized drug molecule C_I:

Drug binding: $$C_F + S \underset{k_d}{\overset{k_a}{\rightleftarrows}} C_B \tag{6-5}$$

Drug internalization: $$C_B \xrightarrow{k_i} S + C_I \tag{6-6}$$

The drug transport and interactions in the arterial wall are described for the three drug forms in Equations 6-7, 8, 9. The cylindrical coordinate system is used for the arterial wall domain for handling the curvature (Figure 6.1(b)):

Free drug C_F: $$\frac{\partial C_F}{\partial t} + v_r \frac{\partial C_F}{\partial r} = \frac{1}{r}\frac{\partial}{\partial r}\left(rD_r \frac{\partial C_F}{\partial r}\right) + \frac{D_\theta}{r^2}\frac{\partial^2 C_F}{\partial \theta^2} - k_a\left(S_0 - C_B\right)C_F + k_d C_B \tag{6-7}$$

Bound drug C_B: $$\frac{\partial C_B}{\partial t} = k_a\left(S_0 - C_B\right)C_F - k_d C_B - k_i C_B \tag{6-8}$$

Internalized drug C_I: $$\frac{\partial C_I}{\partial t} = k_i C_B \tag{6-9}$$

where S_0 is the initial concentration of binding sites in the arterial wall. Among the three drug forms, only the free drug is able to diffuse within the arterial wall (Equation 6-7). The equation describes two different drug diffusivities in the arterial wall: D_θ in the circumferential direction and D_r in the transmural direction. A convective transport term is also included for investigation of the potential impact of transmural interstitial flow in the arterial wall with velocity v_r, which is driven by the pressure difference between the lumen and the perivascular space [115]. For correspondence to scenarios where drug internalization and interstitial fluid flow were not modeled, the factors can be turned off

by setting the internalization rate constant k_i and the interstitial fluid flow velocity v_r to zero.

Because of the elongated shape of smooth muscle cells and the consequent anisotropic arterial wall property, arterial drug diffusion in the transmural direction is hindered, which results in a much smaller apparent drug diffusivity in the transmural direction than that of the circumferential direction [31]. The anisotropic drug diffusivity in the arterial wall has been investigated and revealed impact on drug delivery and distribution in a few studies, where the anisotropic ratio was either treated as a parameter or had empirical values [55, 58, 108]. Theoretical quantification of the drug diffusivity anisotropic ratio, however, does not seem to be published in the literature. In this model, the anisotropic diffusivity is analytically quantified by adopting the expression for estimating effective diffusivity in periodic composite with impermeable flakes [103],

$$\frac{D_\theta}{D_r} = \frac{1}{1+\alpha^2\phi_F^2/(1-\phi_F)} \tag{6-10}$$

where α is the aspect ratio of smooth muscle cells (defined as the smaller cell dimension in the circumferential direction divided by the cell thickness in the transmural direction) and ϕ_F is the volume fraction of smooth muscle cells in the arterial wall. With the volume fraction of smooth muscle cells measured as 60–70% [116], and consider an aspect ratio of 3 [117, 118], the expression estimates an anisotropic diffusivity ratio D_θ/D_r of 9.1–15.7. The estimated range correspond to the reported values (around 10) fairly well [55]. For larger aspect ratio of the cells, even higher anisotropic ratio could be expected through the estimate of expression. In this work, an anisotropic ratio of 10 is used throughout the simulations.

6.3 Numerical Simulation

With appropriate boundary conditions and initial conditions, the integrated model can be solved for the domain described in Figure 6.1(b). For the simulation studies, zero drug concentration is assumed at the coating-lumen interface considering a wash-out condition by the bloodstream, and also at the perivascular interface considering drug clearance [55, 65]. At the arterial wall-lumen interface, the drug flux into the lumen is assumed as zero considering the barrier effect of the endothelial layer and the typically high hydrophobicity for drugs used in drug-eluting stents (such as sirolimus and paclitaxel) that lead to very limited drug dissipation into the bloodstream from the arterial wall [54, 57, 108]. The no flux boundary condition is also applied to the left and right boundaries based on symmetry, and at the coating-strut interface. At the coating-arterial wall interface, an equal flux constraint and equal concentration partitioning are applied. For the initial conditions, the drug is initially uniformly distributed only in the coating.

While the models proposed here are generally applicable, the model parameters can vary depending on the different drugs. For the simulation studies, the model parameters are based on sirolimus. However, little information for drug internalization is available. In order to investigate the internalization factor, a range of its rate constant values is considered with respect to the dissociation binding rate constant (Section 3.2). The dimensions defining the model domain and the model parameters are summarized in Table 6.1.

The mathematical model with domains shown in Figure 6.1(b) was implemented in COMSOL 4.2, which is a simulation platform based on the finite element method. The model domains consist of a single stent strut with coating and the surrounding arterial wall with curvature. The coating and arterial wall domains are meshed as illustrated in

Figure 6.2, where the actual mesh for simulations was much finer. Considering the much smaller scale of the coating domain, a finer mesh in the coating than the arterial wall is used. Boundary layers with smaller mesh-size are also imposed at interfaces with non-zero flux (coating-lumen interface, coating-arterial wall interface, and perivascular interface) to improve the simulation accuracy.

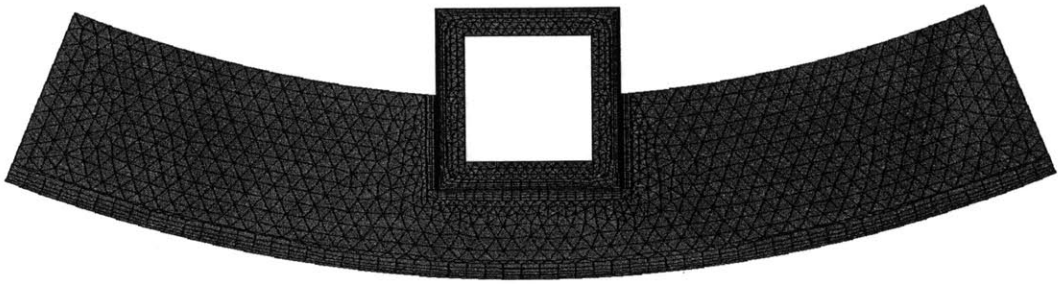

Figure 6.2 Illustrated mesh of the model domain. (The actual mesh used in simulation is much finer.)

A thorough mesh convergence test was carried out for determining the mesh sizes for model simulations (Figure 6.3). The convergence test is performed with constant drug diffusivities in the coating and in the arterial wall, and the relative error was calculated for the drug release profile based on an extremely fine reference mesh. The reference mesh uses sizes of 0.2 μm for the coating and 2 μm for the arterial wall, and contains 2 million cells.

In the convergence test, the relative errors were similar and stayed under 0.5% for different mesh size of the arterial wall domain, while the mesh size of the coating is remained the same at 1 μm (Figure 6.3(a)). Choosing a mesh size of 5 μm for the arterial wall domain, a mesh size of 0.5 μm was selected for the coating (Figure 6.3(b)). The final mesh gives relative error of less than 0.1% and contains 257,712 cells.

Table 6.1 Summary of Model Parameters

Parameters of the model domain		
Outer diameter of the artery	3 mm	[54]
Thickness of the arterial wall	200 μm	[65, 112]
Thickness of the stent strut	140 μm	[88]
Thickness of stent coating	30 μm	[39]
Mesh size for the arterial wall	5 μm	
Mesh size for the coating	0.5 μm	
Mesh size for the boundary layers	0.2 μm	
Parameters of the mathematical model		
Drug diffusivity in the initial PLGA polymer, D_{s0}	10^{-5} μm^2/s	[98, 110]
Drug diffusivity in the aqueous phase, D_{l0}	50 μm^2/s	[103, 110]
Transmural drug diffusivity in the arterial wall, D_r	10^{-1} μm^2/s	[25]
Anisotropic ratio of drug diffusivity in the arterial wall, D_θ/D_r	10	as derived
Association rate constant, k_a	10^4 L/mol · s	[89, 111]
Dissociation rate constant, k_d	10^{-2} 1/s	[89, 111]
Internalization rate constant, k_i	0 or as mentioned	
Weight-based PLGA degradation rate constant, k_w	7.5×10^{-7} 1/s	[75]
Number-based PLGA degradation rate constant, k_n	2.5×10^{-7} 1/s	[75]
Molecular weight dependency of diffusivity, a	1.714	[78, 110]
Drug partitioning coefficient, κ	10^{-4}	[106, 110]
Interstitial flow velocity in the arterial wall, v	0 or as mentioned	
Initial drug concentration in the coating, C_0	10^{-5} mol/L	[65, 108]
Initial binding site concentration in the arterial wall, S_0	10^{-5} mol/L	[25]

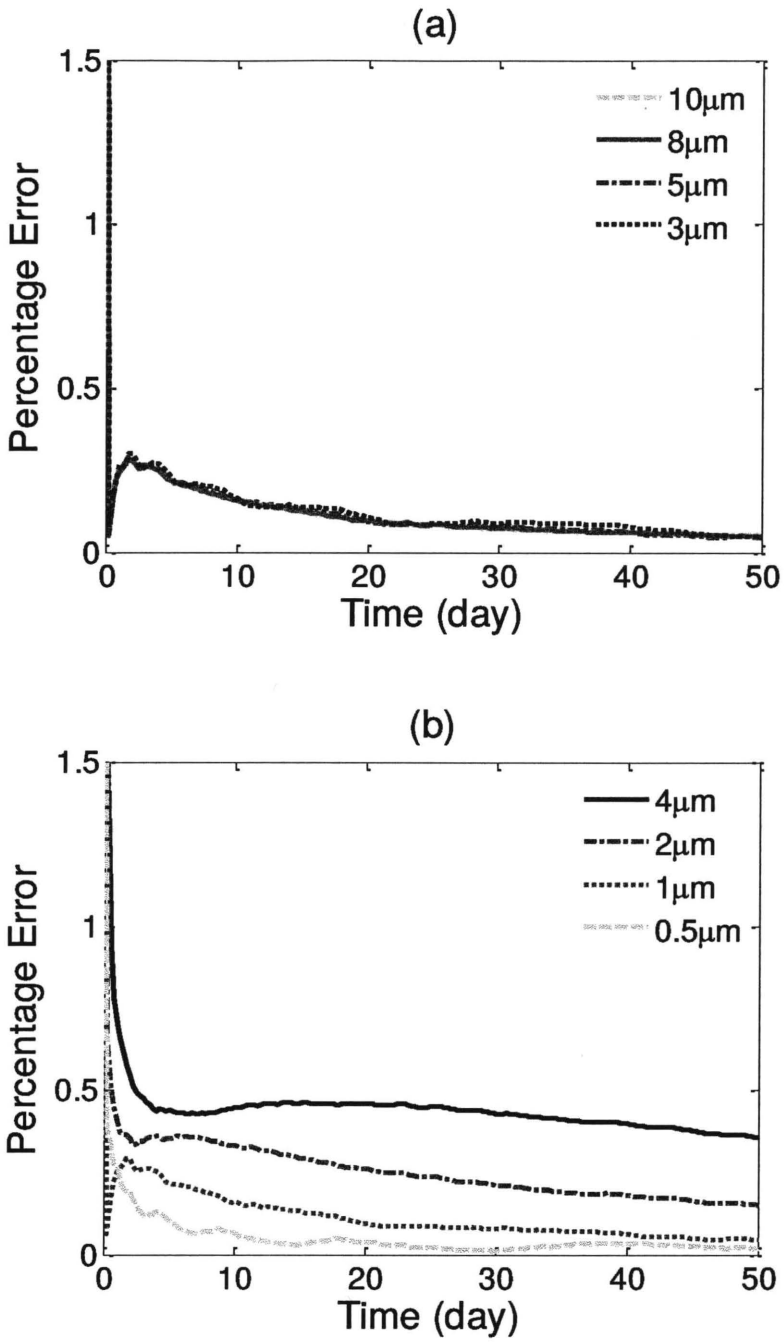

Figure 6.3 Percentage relative error of different mesh sizes compared with the extremely fine reference mesh. (a) Varying mesh size in the arterial wall with constant mesh size of 1 μm in the coating; and (b) Varying mesh size in the coating with constant mesh size of 5 μm in the arterial wall.

6.4 Results and Discussion

In this section, the model simulations first compare the intravascular drug delivery from a biodegradable PLGA coating with that from a biodurable polymer coating. Following that, using the model developed for PLGA-coated stent, the drug internalization rate, interstitial fluid flow, and strut embedment are individually investigated for their impact on the drug transport and distribution. In the model simulations, unless mentioned, half strut-embedment is considered and the internalization rate constant k_i and the interstitial fluid flow velocity v_r are both set to zero, for the purpose of comparing with previous modeling work and inspecting the impact of individual model factors.

The simulation results are reported for drug release profiles in the coating, average drug levels in the arterial wall for the different drug forms, and the spatial drug concentration distribution in the arterial wall. Specifically, the average drug concentration in the arterial wall is defined as the spatial average of each drug form. The three means of characterizing the drug delivery process are consistent with other modeling works, while offering the possibility for potential comparison with future experimental measurements.

6.4.1 Comparing PLGA Coating with Biodurable Coating

In model simulations, the PLGA coating is compared with a biodurable coating for stent-based intravascular drug delivery. In the biodurable stent coating case where the polymer coating stays intact, the drug diffusivity in the coating remains constant at the initial drug diffusivity in the polymer (D_{s0}). The rest of the model parameters are the same for the two scenarios. In the drug release profiles in the coating (Figure 6.4), the two scenarios start with similar release rates in the first two days when the PLGA degradation and erosion are insignificant. Following that, the drug release in the PLGA coating quickly

exceeds that of the biodurable coating as a result of the increasing degradation and erosion of the coating. The characteristics of the release profiles in intravascular delivery are in good correspondence to what was reported for *in vitro* release [45, 110]. In the simulation comparison, the total drug release is achieved in the PLGA coating at around day 30, while the biodurable coating has only released 20% of its loading and remains at very slow releasing rate.

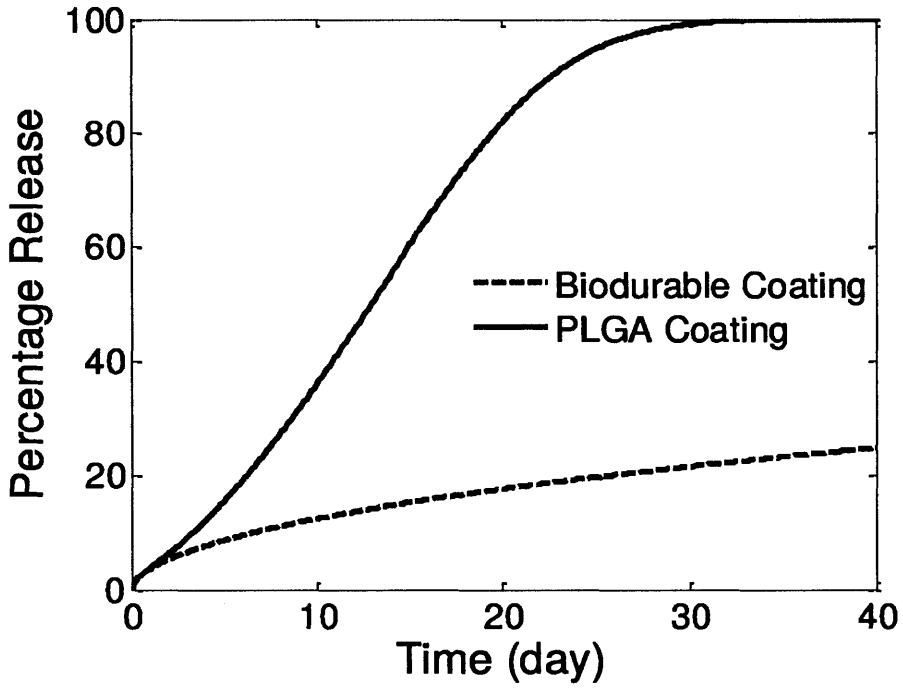

Figure 6.4. Comparison of simulated drug release profiles for the PLGA stent coating (solid red) and the biodurable coating (dash blue). (half strut embedment, $k_i = 0$, and $v_r = 0$)

Corresponding to the difference in the release profiles in the PLGA coating and the biodurable coating, the average drug concentrations in the arterial wall starts off with similar levels for both free drug and bound drug (Figure 6.5). The peak drug concentrations appear very early in the biodurable coating case at around day four, and

the drug levels gradually decrease. In the PLGA coating case, the drug levels keep increasing as a result of accelerated drug release by degradation and erosion in the coating, and do not arrive at the peaks until around day 22, just a few days prior to total drug release in the coating at day 30. Compared with the biodurable coating case, the drug levels in the PLGA coating case decreased much faster after the peak concentrations. The faster decrease is contributed by the higher drug levels in the arterial wall which leads to a fast drug clearance rate at the perivascular interface. In each case, the trends of concentration evolution for the free drug and the bound drug are highly identical, as a result of the fast reversible binding process in comparison with the drug diffusion [108].

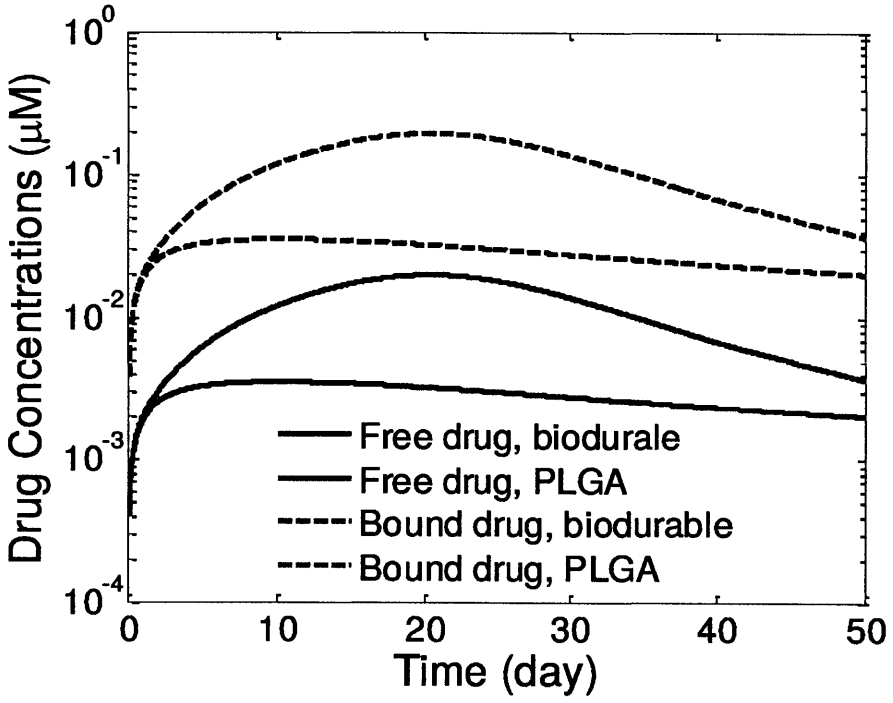

Figure 6.5 Spatially-averaged concentrations of free drug and bound drug in the arterial wall for the PLGA coating case and the biodurable coating case. (half strut embedment, $k_i = 0$, and $v_r = 0$)

Noticeably, the PLGA coating produces overall much higher drug levels in the arterial wall than the biodurable coating for a prolonged period, governed by the faster drug release rate in the coating. In coronary angioplasty procedures, a sustained drug level in the arterial wall for a prolonged period is necessary for reducing the restenosis. The biodurable coatings are typically found to be limited in sustaining a sufficiently high drug level in the arterial wall after the initial release period, because of the low drug diffusivity and slow drug release [34]. The simulations suggest that the requirement can potentially be achieved by using a degradable PLGA coating through the enhanced release by degradation and erosion.

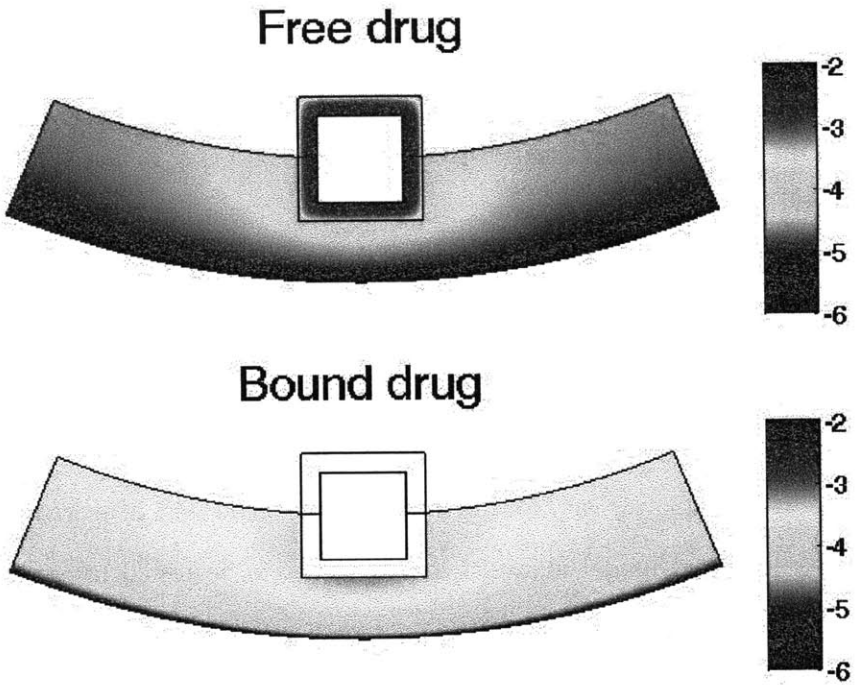

Figure 6.6 Drug concentration distribution in the arterial wall at 25 days for intravascular drug delivery from a PLGA stent coating. Color bar is in logarithmic scale (mol/m^3). (half strut embedment, $k_i = 0$, and $v_r = 0$)

The arterial drug distributions for both free drug and bound drug are shown for the PLGA coating case at day 25 (Figure 6.6), shortly after the drug levels have peaked in the arterial wall. The drug distribution is close to uniform in the circumferential direction, whereas in the transmural direction a gradient is clearly observed closer to the perivascular interface. The better uniformity in the circumferential direction is expected with the anisotropic drug diffusivity which results in fast drug diffusion in the circumferential direction. The observed arterial drug distribution pattern for the PLGA coating case is similar to previous studies of a biodurable coating [108]. The comparison indicates that while the PLGA coating ensures higher overall drug concentrations in the arterial wall than a biodurable coating, the arterial drug distribution pattern is not impacted.

6.4.2 Impact of Drug Internalization

The drug internalization describes the cellular uptake of drug molecules after they associate with the binding sites, and is an important mechanism for drug metabolism in the physiological environment [113, 114]. Only limited studies have considered the impact of the internalization process on the stent-based drug delivery [112]. While the drug internalization rate may vary for the different drugs, and such data are lacking in the literature, the proposed model allows different values to be tested for examining and understanding the potential impact of drug internalization. Because the internalization process is in competition with the dissociation step of binding, values of the internalization rate are investigated based on its relative value to the dissociation rate constant.

To illustrate the drug internalization process, the average drug levels in the arterial wall are simulated and plotted in Figure 6.7 for the three drug forms using the

proposed drug internalization model, assuming a small internalization rate relative to the dissociation rate ($k_i = 10^{-4}k_d$). The simulation shows an initial build-up for bound drug, which peaks and then diminishes as the bound drug gets internalized. Eventually both free drug and bound drugs are converted to internalized drug. The drug binding and internalization kinetics are closely related to that of the well-recognized enzymatic reactions [119], where in this context the binding sites are acting like enzymes. Throughout the period, the available binding sites are at abundance in the arterial wall, as revealed by the much smaller average bound drug levels (< 0.15 μM) compared with that of the overall binding sites concentration (10 μM).

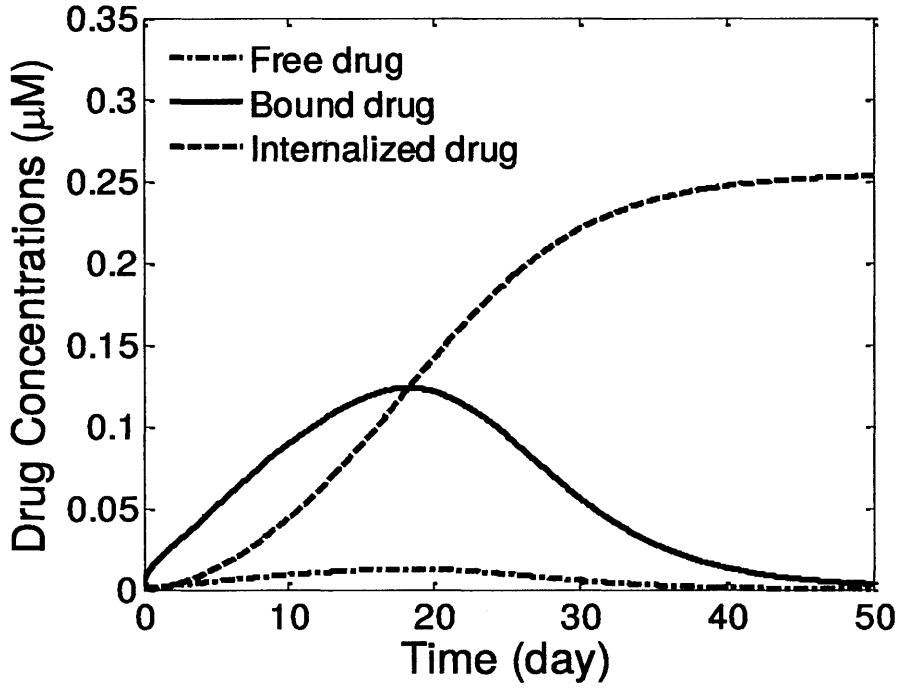

Figure 6.7 Average concentrations of free drug, bound drug, and internalized drug in the arterial wall for a relatively small internalization rate constant (half strut embedment, $v_r = 0$, and $k_i = 10^{-4}k_d$).

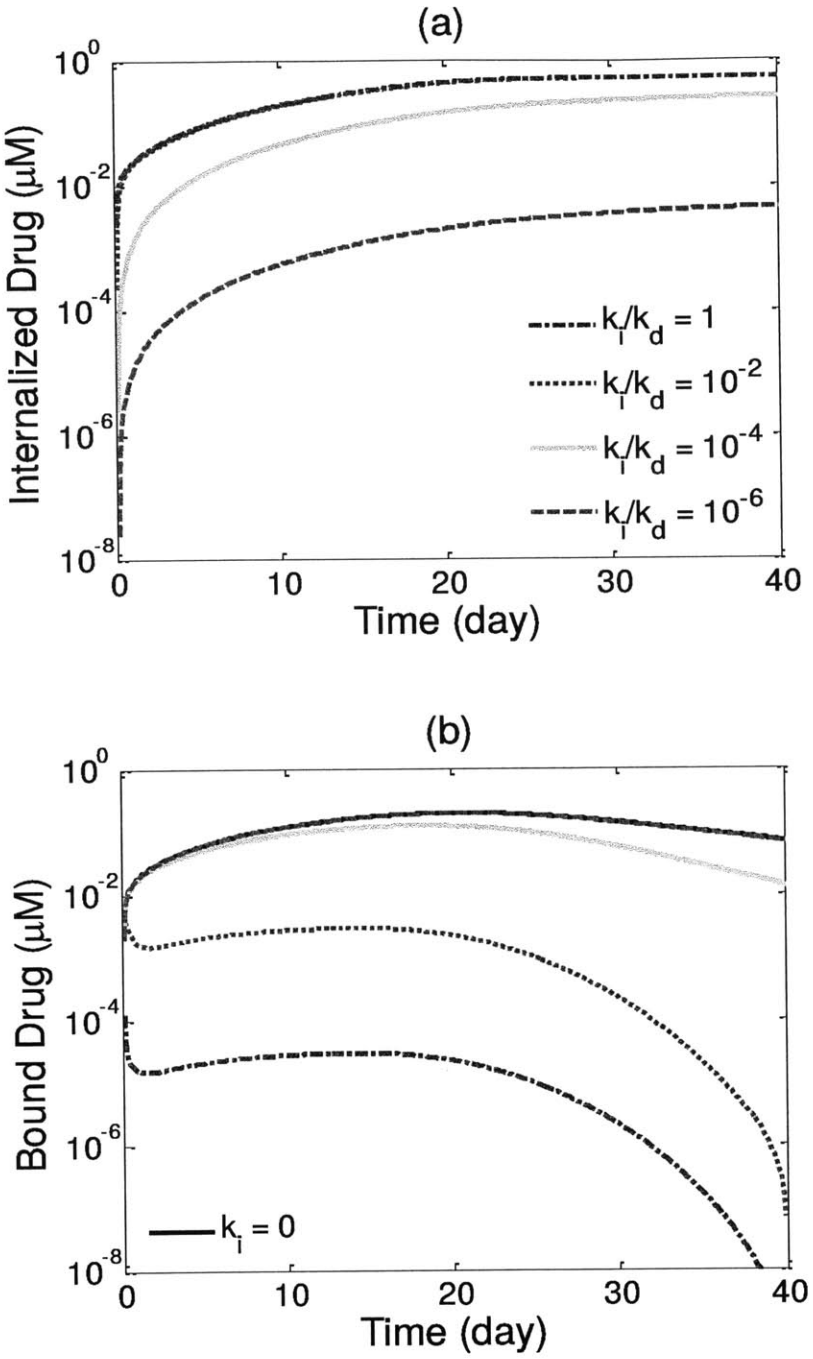

Figure 6.8. Average concentrations in the arterial wall for internalized drug (a) and bound drug (b) at different internalization rates. (half strut embedment and $v_r = 0$)

Different values for the internalization rate constant are examined to look at its impact on the drug delivery process and the conversion among the three drug forms. While the simulations have shown identical release profiles in the coating for the different internalization rates, Figure 6.8 reveals very different drug allocation among the different drug forms for internalized drug (Figure 6.8(a)) and bound drug (Figure 6.8(b)).

For very small internalization rate ($k_i = 10^{-6}k_d$), the bound drug level experiences little change compared with the no-internalization case and very low internalized drug level was generated. Increasing the internalization rate constant to $k_i = 10^{-4}k_d$, a two orders of magnitude increase in internalize drug level is observed, while the bound drug concentration only experiences a small decrease that is more noticeable at later times. The internalized drug level arrives at constant profiles once the internalization rate constant exceeds $k_i = 10^{-2}k_d$, whereas the profiles for the bound drug can still experience drastic decrease for k_i values from $10^{-2}k_d$ to k_d. In all cases, the free drug evolution followed identical trends as the bound drug as a result of the fast reversible binding process and is therefore not illustrated. The simulation results indicate that the arterial drug levels could have a sensitive response with respect to the different rates of drug internalization.

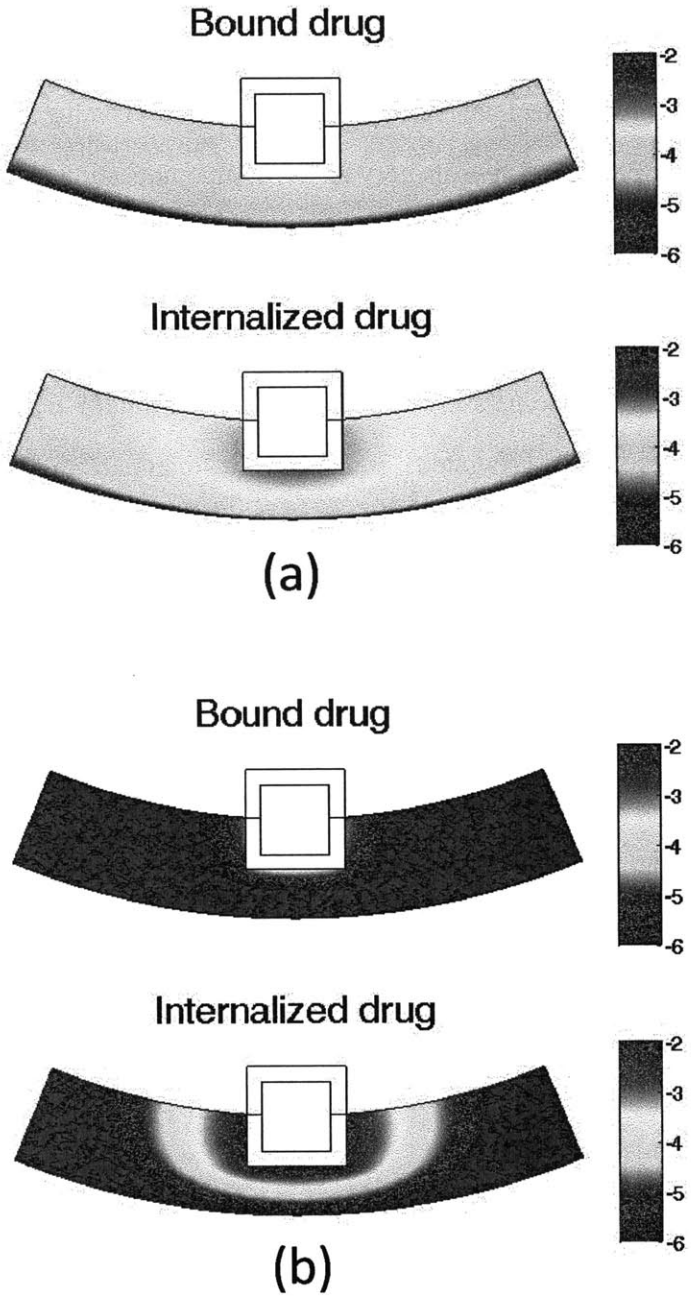

Figure 6.9 Arterial drug distribution at 25 days for (a) small internalization rate $k_i = 10^{-4}k_d$, and (b) fast internalization rate $k_i = 10^{-2}k_d$. Color bar is in logarithmic scale (mol/m^3). (half strut embedment and $v_r = 0$)

Furthermore, the internalization process changes the arterial drug distribution and significantly affects the drug availability in different regions of the arterial wall (Figure 6.9). At small internalization rate (Figure 6.9(a)), the arterial wall drug distribution is still close to uniform in the circumferential direction, similar to the case in the no-internalization case. The internalized drug distribution, however, exhibits gradient in both the circumferential and transmural directions and has higher concentration close to the proximity of the stent strut. With increased internalization rate (Figure 6.9(b)), the arterial distribution becomes highly non-uniform for both bound drug and internalized drug. In the circumferential direction, the drug levels at areas far away from the stent strut have decreased drastically.

As illustrated with the simulations, the consequences of drug internalization could lead to significantly modified arterial drug distribution and reduce the drug availability at arterial sites that are further away from stent strut. The simulations suggest that drug internalization could increase the likelihood of spatial non-uniformity in arterial drug distribution for stent-based drug delivery. As reported in previous studies, the spatial non-uniformity of arterial drug distribution is potentially linked to the growth of more in-stent restenosis at larger inter-strut angle [15, 108]. Interestingly, the internalization process could aggravate the potential adverse effect of low drug levels at arterial sites further away from stent strut in reducing in-stent restenosis. The amount of impact varies with the internalization rate constant and can be determined for a specific drug (such as sirolimus) when experimental characterization of the rate constant becomes available.

6.4.3 Impact of Interstitial Flow

The interstitial flow within the arterial wall is induced by the pressure difference between the lumen and the perivascular space and is typically very small (in the range of 0.01–0.1

μm/s [115]), and the convective transport term for inside the arterial wall is often left out in the drug transport models of drug-eluting stents [54, 67]. A detailed analysis has been carried out to depict the relative importance of convective transport to that of diffusive transport, where drug pharmacokinetics were absent and the impact of convection transport for a hydrophobic drug only starts to become apparent for Peclet number larger than 10 [55]. The interstitial flow velocities can be calculated by Darcy's Law if the pressure difference and the arterial wall permeability are known [120]. While the velocity may differ in different subjects, and the focus of the study was on the impact of the velocity on drug transport rather than accurate calculation of the velocity itself, a range of values reasonable for the system were used [115].

A thorough investigation of the impact of interstitial flow is carried out using our model. As described in Equation (7), the flow velocity is nonzero only in the transmural direction. While fluid momentum equations are not explicitly solved in this work, the fluid mass conservation equation (the so-called continuity equation) can be used to show that the velocity v_r is inversely dependent on the radius. Considering the small curvature of the arterial wall (that is, a thin wall thickness compared with the radius of the lumen), the variation of the velocity in the transmural direction is negligible, and a constant velocity is assumed in the investigation of the impact of interstitial flow on the drug transport. The simulations show that the drug release profiles in the PLGA coating is not affected by the interstitial fluid flow within the arterial wall for the reported interstitial flow velocities (figure not shown). The absence of variation in the drug release rate is a result of the significantly slower drug diffusion within the PLGA stent coating in comparison to the mechanisms for drug removal at the exterior of the coating, which are contributed by both the drug diffusion in the arterial wall and the wash-out boundary condition at the coating-lumen interface.

The average drug concentrations in the arterial wall, however, are significantly impacted by the presence of convection (Figure 6.10). From no interstitial flow to increasing flow velocity, the average drug concentrations for both free and bound drug decrease significantly. While the same drug release rates in the different scenarios indicate that the same amount of drug passed through the coating-arterial wall interface, the presence of interstitial flow increases the transport in the transmural direction and leads to faster drug clearance at the perivascular interface. With interstitial fluid flow, the peaking of the average drug concentrations shift towards earlier times. The Peclet number in the arterial wall is calculated as $P_e = vL/D_T = 20$ for interstitial flow velocity (v_r) of 0.01 μm/s and wall thickness (L) of 200 μm, which confirms the non-negligible impact of the interstitial flow in drug transport.

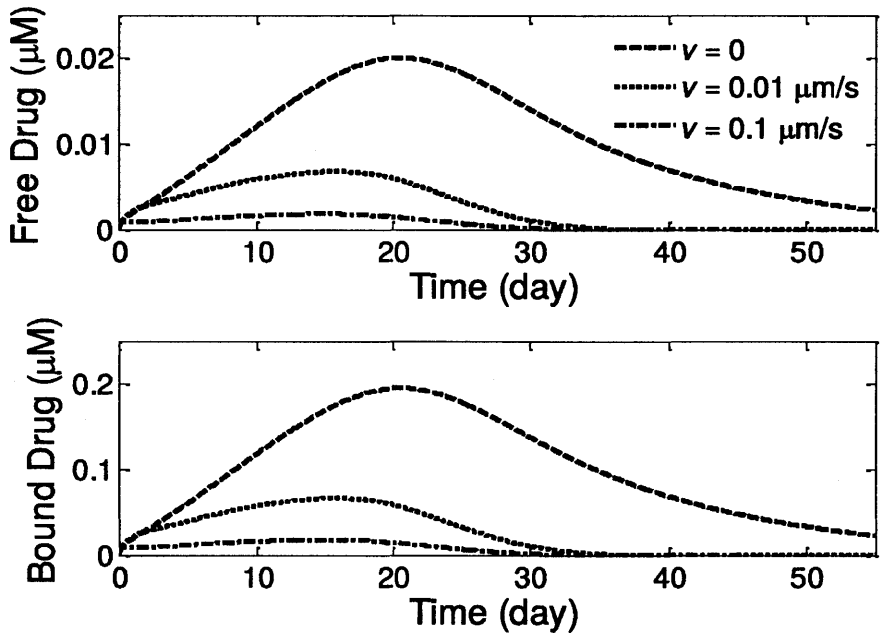

Figure 6.10 The average drug concentrations in the arterial evolution at different interstitial fluid flow velocities. (half strut embedment and $k_i = 0$)

The drug distribution shows greatly impaired drug uniformity in the circumferential direction as a result of the convection with even low interstitial flow velocity (0.01 μm/s) (Figure 6.11). Compared with the case with no interstitial flow (Figure 6.6), the convection results in highly non-uniform distribution in the circumferential direction. Interestingly, the interstitial flow enhances the uniformity in the transmural direction, especially for areas closer to the stent strut. However, the drug coverage in the upper layers are important for reducing in-stent restenosis [22]. Similar to the analysis on the drug internalization, the interstitial flow creates spatial non-uniformity of drug distribution and leads to lowered drug level at arterial sites further away from the stent strut, which could increase the chances of potential adverse outcomes such as in-stent restenosis growth.

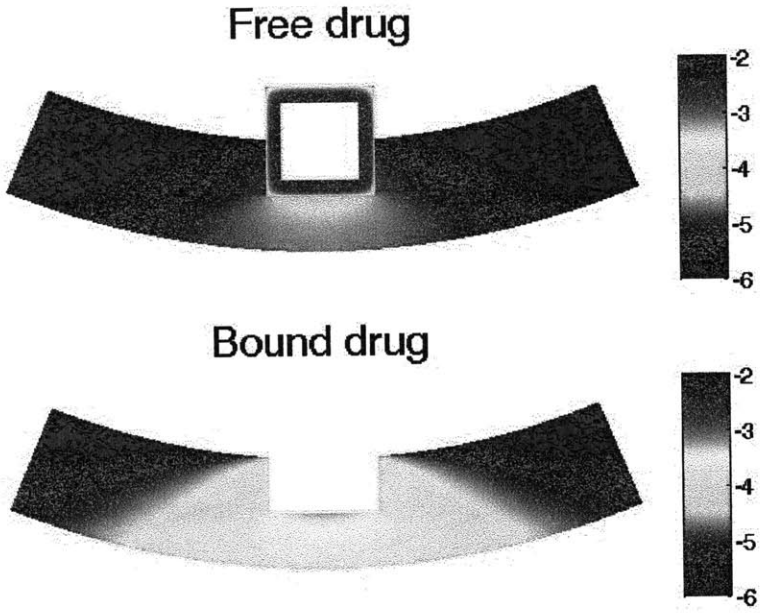

Figure 6.11. Arterial drug distributions for free drug and bound drug with transmural interstitial flow (v = 0.01 μm/s) at day 20. Color bar is in logarithmic scale (mol/m^3). (half strut embedment and $k_i = 0$)

6.4.4 Impact of Strut Embedment

The strut embedment in the arterial wall is another important factor that can affect the drug release in the stent coating and the drug delivery into the arterial wall. Investigation of strut embedment was previously carried out for a biodurable stent coating where the drug binding pharmacokinetics was absent [20]. The model simulations here considered three different scenarios of embedment: contact, half embedded, and fully embedded. The strut embedment was examined for its impact on the drug release in the PLGA coating and the arterial drug up-take. The arterial wall thickness is used as 300 μm in the simulations in this section.

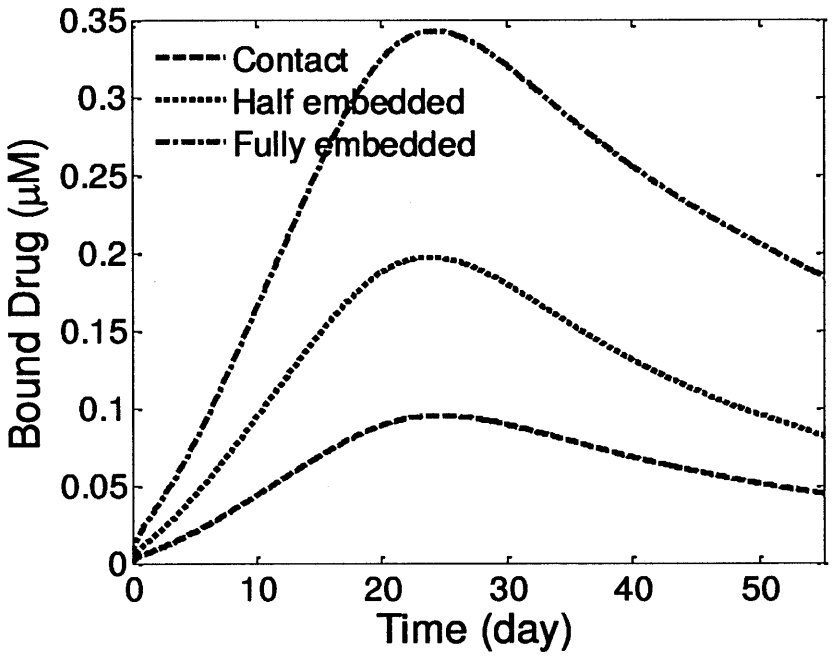

Figure 6.12. The average bound drug levels in the arterial wall for different strut embedment. ($k_i = 0$, and $\nu_r = 0$)

The simulations show that the drug release profiles in the PLGA coating for the three different strut embedment overlap with each other (figure not shown), similar to

what was observed in the cases for different interstitial flow and internalization rates. The observed negligible impact on the drug release profiles in the PLGA coating, again, is due to the rate-limiting step of drug diffusion within the PLGA coating.

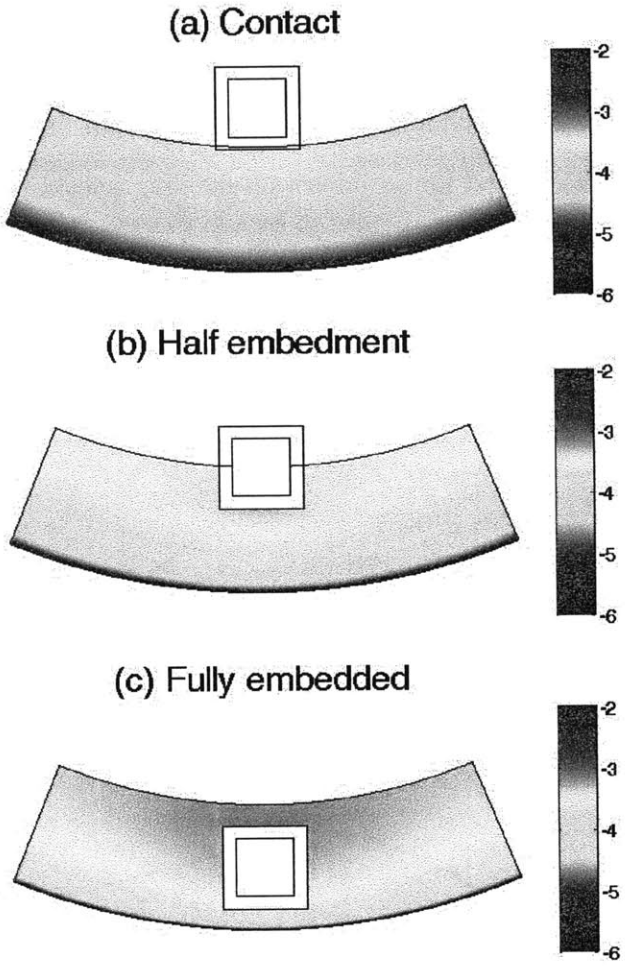

Figure 6.13 Bound drug distribution in the arterial wall at day 25 for (a) A contacting stent strut, (b) A half-embedded strut, and (c) a fully embedded strut. Color bar is in logarithmic scale (mol/m^3). ($k_i = 0$, and $v_r = 0$)

The average bound drug concentration in the arterial wall increases with more strut embedment (Figure 6.12), which is within expectation, because with more

contacting area of the coating with the arterial wall, more of the released drug gets into the arterial wall rather than that depletes into the blood stream. The enhancement of arterial drug levels for higher degrees of strut embedment is in agreement with findings in a previous study of a biodurable coating [54]. Interestingly, the drug concentrations all peak at the same time at around 24 days. The peak drug levels are roughly proportional to the ratio of the contacting area of the stent coating with the arterial wall. The fully embedded case has the highest average drug concentration throughout the time.

The arterial drug distribution for bound drug is shown for the three different strut embedments in Figure 6.13. A transmural drug concentration gradient is observed in all three cases, with the lowest drug concentration at the perivascular interface due to the drug clearance. In the fully embedded case, drug accumulates and results in the highest drug concentration in the upper layers of the arterial wall. While enhanced drug concentration in the upper layers may be beneficial, the increased degree of strut embedment also indicates more damage to the arterial wall during the stent expansion process, which could potentially counter the benefit of increased drug levels.

6.5 Conclusions

The model developed in this work considers a wide and detailed scope of physical, chemical, and biological processes involved in the intravascular drug delivery from a stent with PLGA coating. A mechanistic model for drug release in the biodegradable PLGA coating that couples the drug diffusion with PLGA degradation and erosion was adopted and integrated with subsequent drug transport and distribution in the arterial wall that takes into account anisotropic drug diffusivity and reversible drug binding in the arterial wall. Theoretical estimation of the anisotropic drug diffusivity was also proposed and analyzed with good correspondence to the literature.

The simulation comparison of PLGA coating and biodurable coating has confirmed the difference in drug release rates for intravascular drug delivery, in accordance with expectations gained from *in vitro* release studies. The comparison revealed the enhanced average drug levels in the arterial wall by utilizing a PLGA stent coating, while the simulations suggested similar patterns of arterial drug distribution compared to the biodurable coating case.

Simulation and analysis of factors including drug internalization, transmural interstitial fluid flow in the arterial wall, and strut embedment were carried out. Negligible change in the drug release profiles in the PLGA coating was observed in all cases, as a result of the slow drug diffusion within the coating compared with drug transport at the coating-lumen interface and coating-arterial wall interface. Higher average drug levels are observed for slower interstitial fluid flow velocities and higher degree of strut embedment. More importantly, each of the investigated factors can significantly change the drug distributions in the arterial wall, which can potentially influence the treatment outcomes. The presence of drug internalization irreversibly consumes and reduces the drug molecules for diffusion, and can localize drug concentrations in the arterial wall neighboring the strut. The transmural interstitial fluid flow, even at very slow velocity, depletes the drug levels at distant arterial sites by convection. Both the drug internalization and interstitial fluid flow can lead to low drug levels at distant arterial wall sites away from the strut, which can potentially impair the drug-eluting stent performance in reducing restenosis. For the different strut embedment, more strut embedment is found to induce higher drug concentration in the upper layer of the arterial wall.

While the different model factors were investigated individually in this study in order to acquire insights on their distinct impacts on the drug transport and distribution,

when more than one model factor are in consideration, a combination of their individual impact can be expected. For example, when both drug internalization and interstitial flow are present, they will both contribute to reduce the drug availability at the sites far away from the strut in the circumferential direction.

CHAPTER 7

CONCLUSIONS

The dissertation developed a mathematical model for describing the intravascular drug delivery and distribution from a drug-eluting stent with biodegradable coating, and used to the model simulations to relate to reported experimental observations and to provide insights into the system. The dissertation was completed in three steps.

In the first part of the dissertation, a model was developed for describing the intravascular drug delivery of a hydrophobic drug from a drug-eluting stent with biodurable polymeric coating. The drug transport and the coupled reversible drug binding in the arterial wall were modeled simultaneously. Drug diffusivities in the coating and in the arterial wall were investigated in detail for their impact on the drug release and arterial drug distribution. The average drug concentrations in the arterial wall at quasi-steady state are observed to be greatly determined by the vascular drug diffusivity rather than the coating drug diffusivity. In particular, anisotropic drug diffusivities in the arterial wall were studied in detail in model simulations, which result in slightly different spatially-averaged drug levels but drastically different spatial distributions. Higher free-drug concentration than bound-drug concentration can occur in the arterial wall, with the critical condition of occurrence derived as $C_s/\kappa_{cw} > S_0 - 1/K$. Higher circumferential vascular diffusivity reduces the drug gradient in the circumferential direction and produces more uniformly loaded drug layers, which can be beneficial in reducing in-stent restenosis after drug-eluting stent implantation. The simulation results provided insights

as to how changes in drug properties (such as its directional diffusivities) influence spatial uniformity in the arterial wall and show potential guidance for designing drug-eluting stents with improved efficacy. The developed model served as the framework for the dissertation.

In the second part of the dissertation, a mechanistic model was developed for describing the PLGA degradation, erosion, and coupled drug release from PLGA stent coating. An analytical expression for the PLGA mass loss was derived for the first time in the literature. The developed mass loss model and the first-order degradation model for molecular weight change were validated with experimental data from the literature. Simultaneous drug diffusion through polymer solid with changing average MW and liquid-filled pores was modeled, and an effective drug diffusivity model was derived taking into account various factors including polymer MW change, diffusivity in the polymer, diffusivity in the liquid-filled pores, and drug partitioning between solid and liquid phases. The model was demonstrated for sirolimus release from PLGA stent coating and predicted experimental data in the literature. Comparison of the proposed model with existing models revealed the significance of simultaneous sirolimus diffusion through polymer solid and pore space. The mechanistic model developed has great potentials for application in the design of PLGA coatings for drug-eluting stents. The model can also be extended for applications to other PLGA-based drug delivery systems.

In the last part of the dissertation, an integrated model was developed for intravascular drug delivery from a drug-eluting stent with PLGA coating. The mechanistic model for drug release in the biodegradable PLGA coating was adopted and

integrated into the model framework for drug transport and distribution in the arterial wall. Theoretical estimation of the anisotropic drug diffusivity was proposed and analyzed. A PLGA stent coating was compared with a biodurable coating in simulations. The comparison indicates that while the PLGA coating ensures higher overall drug concentrations in the arterial wall than a biodurable coating, the arterial drug distribution pattern is not impacted.

Simulation and analysis of factors including drug internalization, transmural interstitial fluid flow in the arterial wall, and strut embedment were carried out. Higher average drug levels are observed for slower interstitial fluid flow velocities and higher degree of strut embedment. More importantly, each of the investigated factors can significantly change the drug distributions in the arterial wall, which can potentially influence the treatment outcomes. The presence of drug internalization irreversibly consumes and reduces the drug molecules for diffusion, and can localize drug concentrations in the arterial wall neighboring the strut. The transmural interstitial fluid flow, even at very slow velocity, depletes the drug levels at distant arterial sites by convection. Both the drug internalization and interstitial fluid flow can lead to low drug levels at distant arterial wall sites away from the strut, which can potentially impair the drug-eluting stent performance in reducing restenosis. For the different strut embedment, more strut embedment is found to induce higher drug concentration in the upper layer of the arterial wall. When more than one model factor are in consideration, a combination of their individual impact can be expected.

Besides the factors investigated in detail in this dissertation, other factors related to the pathological conditions, such as plaque, thrombus, and regions of tissue compression due to the stent implantation, may change the drug transport properties in the arterial wall and can also play an important role in the efficacy of treatment with drug-eluting stents. While some studies have been carried out [60, 109], such factors were not investigated in this study and further research efforts are necessary. In addition, this dissertation was focused on modeling drug delivery and distribution in the circumferential direction for insights on potentially reducing the non-uniform circumferential restenosis growth [52], and extension of the developed model to 3D to include the drug transport in the axial direction may also be interesting for future investigations.

The developed model here provides the basis of a design tool for evaluating and studying a PLGA coating for stent applications, with the ease of adaptation to more sophisticated scenarios (e.g., consideration of more pathological conditions). Simulations using the model help to provide insights into the drug release and distribution by a stent with PLGA coating, as well as the potential impacts of various factors that can affect the efficacy of drug delivery. With the developed model, optimization of the model parameters, such as different stent strut geometries and coating thickness, can also be performed for exploration on the design of PLGA-coated drug-eluting stents.

APPENDIX CHAPTER 8

2D CONTRIBUTION MAP FOR FAULT IDENTIFICATION[4]

Abstract All control engineers should be able to detect and identify faults (that is, abnormal conditions in a system) from the analysis of large heterogeneous time series data sets. This education column provides an introduction to multivariable data-based methods for fault detection and fault identification, with the latter being the determination of system variables that contribute the most to a detected fault. For fault identification in statistical process monitoring, the contribution plot is the mostly commonly used tool, for quickly identifying the most affected variables. Contribution calculations are revisited in the context of principal component analysis and T^2 statistics, and a 2D contribution map is illustrated for the examination of time series data under faulty conditions. The 2D contribution map is compared to the traditional 1D contribution plot using simulated data from a realistic chemical process. The 2D contribution map demonstrates the potential to enable greater understanding of the fault and how its effects are propagated through the system.

8.1 Introduction

Faults inevitably occur in industrial systems, and become more prevalent as systems become increasingly large scale and interconnected. The closed-loop performance of the

---

[4] Work published as: X. Zhu and R.D. Braatz, 2D Contribution Map for Fault Identification, *IEEE Control Systems Magazine*, in press.

control system depends critically on the proper functioning of the process and control equipment, so faults need to be detected and diagnosed quickly from the real-time data collected from the system. Rapid detection and diagnosis can minimize downtime, increase the safety of plant operations, and reduce manufacturing costs. Statistical process monitoring (SPM) applies multivariate data-driven methods to process data for fault detection and diagnosis, and has been popular in both academic research and industrial practice over the past two decades [121-125]. Data-driven methods such as principal component analysis (PCA), partial least squares (PLS), and other modified methods are used to characterize the data collected during normal process conditions. Such methods are dimensionality reduction techniques that project the high-dimensional process data into much lower dimensional spaces. Fault detection is based on multivariate statistics, such as T^2 statistics for describing variations within the lower dimensional space and Q statistics for representing variations in the residual space, in which rigorously derived control limits are computed from the data [121-125].

Typical procedures in SPM involve a fault identification step after the detection of a fault to identify the most likely variables closely associated with the fault (that is, the "faulty variables") by analyzing each variable's contributions [125]. A contribution plot summarizes quantitative information about the potentially faulty variables. While useful, the traditional contribution plot only examines the contributions at one observation (time point), and multiple contribution plots are needed to illustrate multiple observations in time series data. In comparison, a 2D contribution map stacks multiple observations into one image to clearly illustrate the contribution of the variables over the entire faulty data

times series, which enables the fast identification of faulty variables within large heterogeneous data sets.

The next section is an introduction to principal component analysis [121-125], which is the most commonly used technique for fault detection and identification for large heterogeneous data sets. The 2D contribution map is presented as a more effective visualization than the commonly used 1D contribution plot used for fault identification. The methods are illustrated and compared through application to data collected from a well-known model problem known as the Tennessee Eastman process.

8.2 PCA and T^2 Statistic Revisited

Consider a data matrix $X \in \mathcal{R}^{m \times n}$ containing m observations of n process variables at the normal process conditions. The matrix X should be *autoscaled*, that is, each process variable should be pretreated by subtracting its mean and dividing by its standard deviation. PCA dimensionality reduction uses the singular value decomposition

$$\frac{1}{\sqrt{m-1}} X = U \Sigma V^{T} \tag{8-1}$$

where $U \in \mathcal{R}^{m \times m}$ and $V \in \mathcal{R}^{n \times n}$ are unitary matrices and $\Sigma \in \mathcal{R}^{m \times n}$ is a diagonal matrix containing the singular values in decreasing order ($\sigma_1 \geq \sigma_2 \geq \cdots \geq \sigma_{\min\{m,n\}} \geq 0$).

For each principal component i, its *loading vector* is given by the ith column vector of the matrix V, with the variance of the projected training data along the loading vector being equal to σ_i^2.

In the data modeling step, only a small number of the principal components, known as the *reduction order a*, are retained in the PCA model. Several methods are available for determining the value of *a*, including the percent variance test, the scree test, and cross-validation [121-125]. For demonstration purposes, this article uses the percentage variance test, which chooses *a* based on the lower dimensional space containing a specified minimum percentage of the total variance (for example, at least 95%).

Once the reduction order *a* is determined, the *loading matrix* $P \in \mathcal{R}^{nxa}$ is the first *a* column vectors in the *V* matrix.

For an observation $\boldsymbol{x} \in \mathcal{R}^{nx1}$, the *score vector* $\boldsymbol{t}$, which represents the data projection onto the principal components, is

$$\boldsymbol{t} = P^{T}\boldsymbol{x} \tag{8-2}$$

The T^2 statistic, which is a measure of how far the observation is from the center of the characterized normal data, can be calculated directly from the PCA representation by

$$T^2 = \boldsymbol{x}^{T} P \Sigma_a^{-2} P^{T} \boldsymbol{x} \tag{8-3}$$

where $\Sigma_a \in \mathcal{R}^{axa}$ is a diagonal matrix containing the first *a* rows and columns of Σ in (8-1).

The threshold for detecting abnormalities in new observations is given by the T^2 statistic

$$T^2_{\alpha}(\alpha) = \frac{a(m-1)(m+1)}{m(m-a)} F_{\alpha}(a, m-a) \tag{8-4}$$

where $F_{\alpha}(a, m-a)$ defines the upper $100\alpha\%$ critical point of the F-distribution with a and $m-a$ degrees of freedom. When the T^2 statistics of the new observations (for example, two consecutive observations) violate the threshold, a fault is alarmed.

Fault identification is carried out immediately after a fault is detected in the process data using the T^2 or any alternative fault detection statistic. The *contribution plot* quantifies the contribution of each process variable to the PCA scores (8-2) to identify the process variables that are most closely associated with, and potentially responsible for or a direct consequence of, the abnormal/out-of-control status. The procedure for the calculation of the contributions is [125]:

1. Given a vector of observations $\boldsymbol{x}$ (auto-scaled with the mean and variance of the training data) and its calculated score vector $\boldsymbol{t}$, the *contribution* of each process variable x_j to each t_i in the score vector $\boldsymbol{t}$ is calculated from

$$\text{cont}(i,j) = \begin{cases} \frac{t_i}{\sigma_i^2} P_{i,j} x_j & \text{if } \frac{t_i}{\sigma_i^2} P_{i,j} x_j \geq 0 \\ 0 & \text{if } \frac{t_i}{\sigma_i^2} P_{i,j} x_j < 0 \end{cases} \tag{8-5}$$

   where $P_{i,j}$ is the (i,j)th element of the loading matrix P.

2. The *total contribution* of the process variable j at the observation is calculated by

$$\mathrm{CONT}(j) = \sum_{i=1}^{a} \mathrm{cont}(i, j) \tag{8-6}$$

For each observation, the CONT is a vector whose length is equal to the number of process variables. In the traditional contribution plot, the CONT is plotted for the observation at which the fault is detected. For time series data, the procedure is repeated to generate one contribution plot at each observation. A 2D contribution map, which stacks the series of observations in one single colormap is a more convenient alternative for representing the information. The 2D contribution map is illustrated below for data from the Tennessee Eastman process.

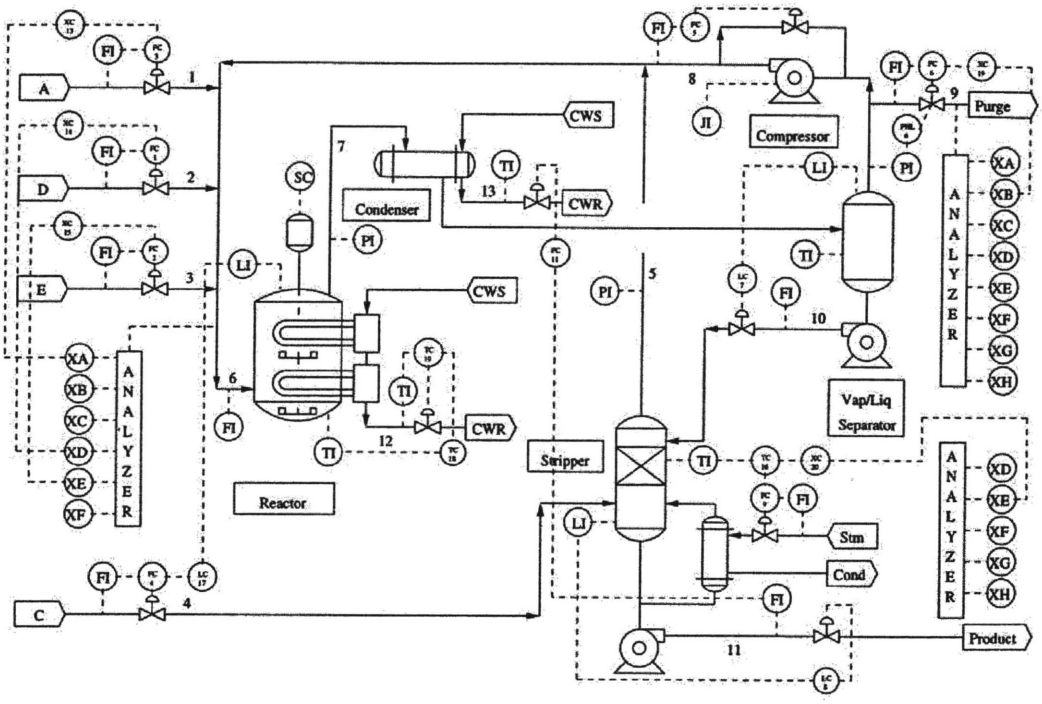

Figure 8.1 The Tennesse Eastman Process flow diagram with plant-wide control structure [2],[9].

8.3 Tennessee Eastman Process Example

The Tennessee Eastman process (TEP) is a realistic simulation of a chemical facility created by the Tennessee Eastman Company [126]. The TEP is widely used by researchers for evaluating process control and monitoring methods (for example, [123], [127], [128]). Figure 8.1 shows the TEP flow diagram with a plant-wide control structure, which has 41 measurements, 12 manipulated variables, and 21 preprogrammed faults. The process consists of three main units (a reactor, a separator, and a stripper), and produces two products (labeled G and H) from four reactants (labeled A, C, D, and E). The process is nonlinear, open-loop unstable, and contains a mixture of fast and slow dynamics. The closed-loop system is stable and provided acceptable performance over the entire operating regime when no faults occur in the system. Of the 21 preprogrammed faults, some faults are detectable and identifiable using classical single-variable control charts such as Shewhart, exponentially-weighted moving average (EWMA), and cumulative sum (CUSUM) whereas some faults are challenging for even the most advanced methods. Detailed descriptions of the process and the control structure, as well as a description of the classical control charts, are available in [123],[129].

In this example, the data under the normal operating conditions were used as the training data for PCA modeling, and the data collected during Fault #1 was used as the testing data for demonstrating the method (the data are available online at http://web.mit.edu/braatzgroup/TE_process.zip). Fault #1 is a step change in the A/C feed ratio in Stream 4 (Figure 8.1). The data set for normal operating conditions contains 500 observations equally sampled over 25 hours, and the data set for Fault #1 has 480

observations equally sampled during a 24-hour period. Based on the normal training data, a reduction order a = 36 was obtained to retain 95% of the variance. Figure 8.2, which shows the T^2 statistic of the training and testing data sets, indicates a fault detected at around hour 25, several sample times after the fault has occurred. The control limit shown as a blue line was calculated by (4) at the 99% confidence level.

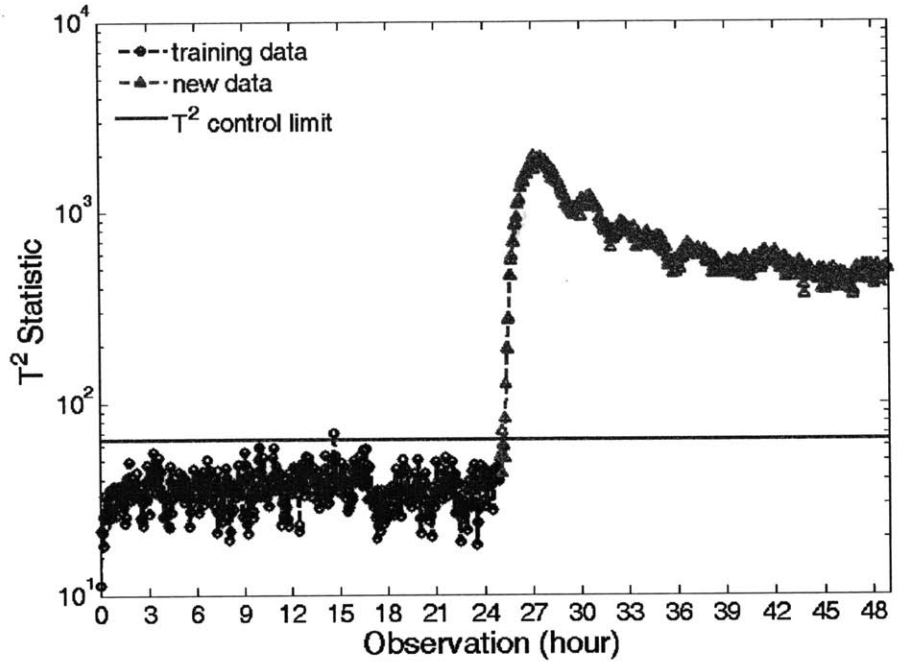

Figure 8.2 The T^2 statistic for normal training data (black) and faulty test data (red) indicates a fault detected after hour 25.

The traditional contribution plot in Figure 8.3 illustrates the contribution of process variables at the observation upon which the fault was detected (the fault was alarmed after two consecutive T^2 control limit violations, or 8 sampling points after the fault occurrence). The plot suggests the fault is most likely associated with process variable 16 (XMEAS 16, the stripper pressure). However, contribution plots for subsequent observations show

different variables having the largest contributions (Figure 8.4). In this circumstance, because of the dynamics of the closed-loop system, the most critical process variables associated with the fault was indeterminate using the 1D contribution plots.

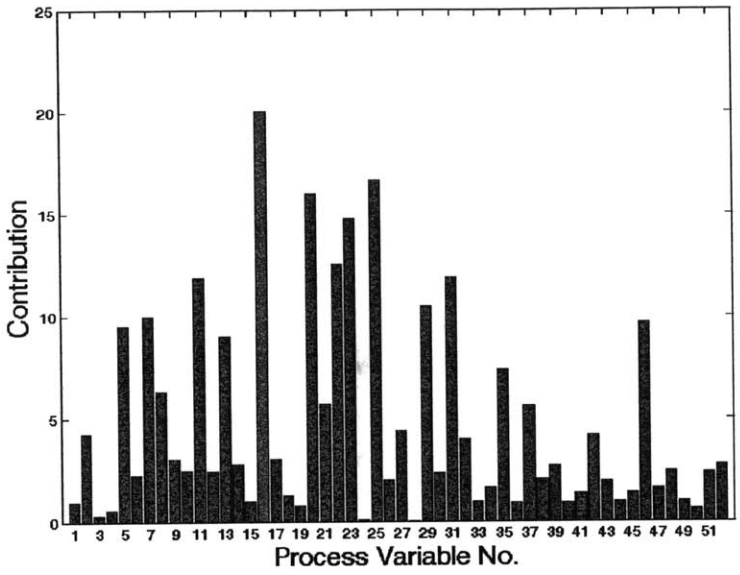

Figure 8.3 Traditional contribution plot of testing data set at the observation time point of fault detection.

The same contribution data plotted as the 2D contribution map in Figure 8.5 enables the reliable identification of the key process variables associated with the fault: XMEAS 1 (A feed, Stream 1) and XMV 3 (A feed flow, Stream 1), both of which show consistent strong bands of contribution. Fault #1 is involved with a feed ratio change of A/C in Stream 4, and a control loop changed the A feed in Stream 1 to compensate for the fault. The 2D contribution map indicates low initial contributions of all process variables at times right after the fault occurs, and how the effects of the fault are gradually propagated into XMEAS 1 and XMV 3.

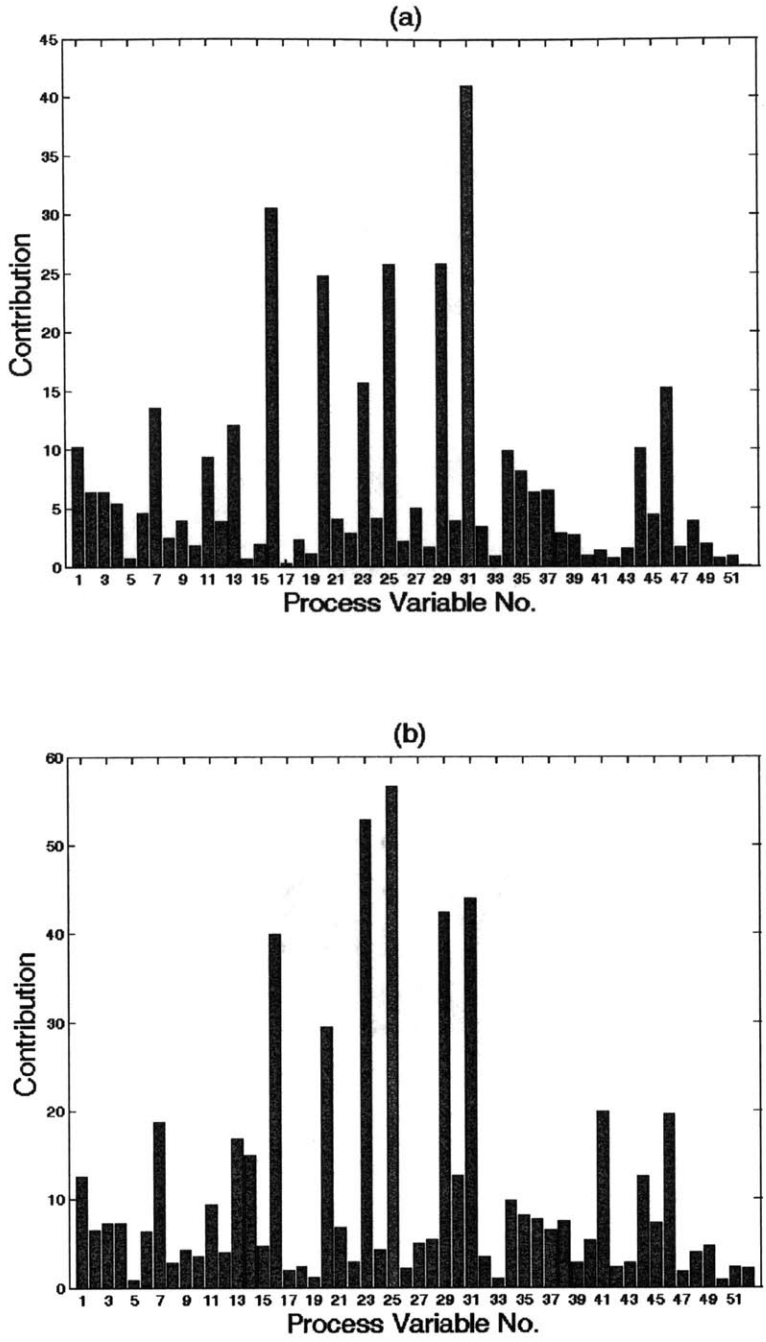

Figure 8.4 Different most faulty variables were picked out in the traditional contribution plot. (a) and (b) are 1 and 3 samples after the fault detection point in Figure 8.3, respectively.

Figure 8.5 shows that in the first few hours following the fault occurrence (hours 25-29), more than a dozen process variables show high contributions to the fault, which corresponds to the period when the closed-loop control system is trying to compensate for the fault. It is unlikely that a control engineer applying 1D contribution plots to observations in this time period will correctly determine the key faulty variables.

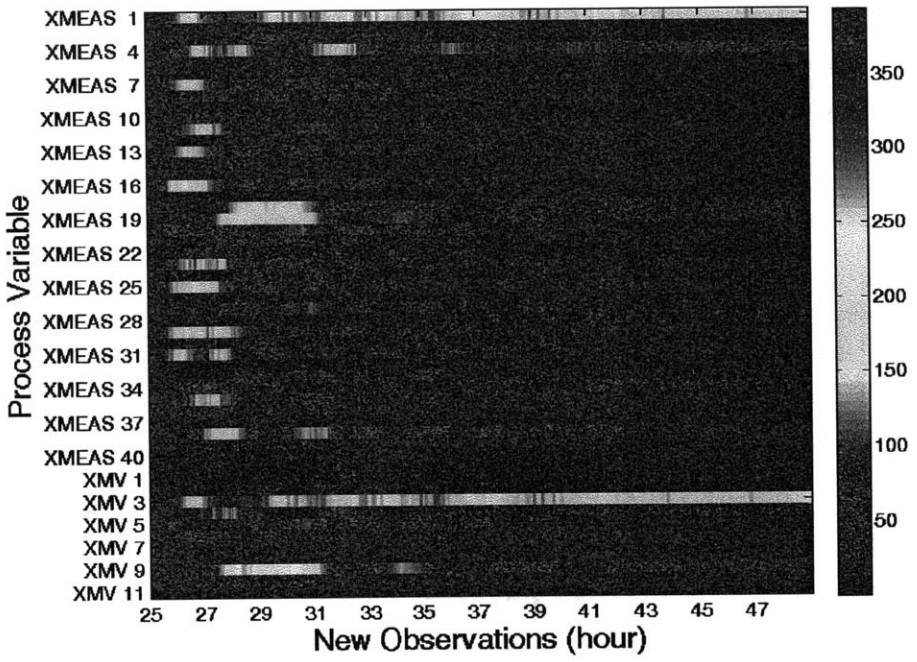

Figure 8.5 2D contribution map of the testing data (Fault #1) provides a visual identification of the most contributing variables in bright bands.

An inspection of Figure 8.5 indicates that the 1D contribution plot would correctly identify the variables associated with Fault #1 if the contributions were averaged over two hours, or the data were averaged over two hours before applying the 1D contribution plot. Averaging over long time windows, however, would directly conflict with the goal of correctly identifying the associated faulty variables quickly after the fault is detected.

Further, plotting multiple time series, as in the 2D contribution map, is generally more useful than plotting single snapshots as done in the 1D contribution plot, because the best time period for identifying faults is not known a priori and will vary depending on the different fault dynamics.

The 1D contribution plot will typically give comparable results when the fault response is fast and localized. For example, consider Fault #4, which is a change in reactor cooling water inlet temperature. The effect of this fault on the variables is simple enough that the contribution is concentrated on XMV 10 (reactor cooling water flow) from the point of fault occurrence, as shown in Figure 8.6, so the 1D contribution plot can also quickly identify the faulty variable.

The 2D contribution map and the 1D contribution plot are essentially two ways of presenting the same data. In fact, in Figure 8.5, each column corresponds to the 1D contribution plot at that observation time. The 2D contribution map, however, assembles the information to enable a more useful visualization for identifying the faulty variables. The 2D contribution map enables the human operators or control engineers to be better informed, to speed their ability to track down the precise nature and cause of the fault.

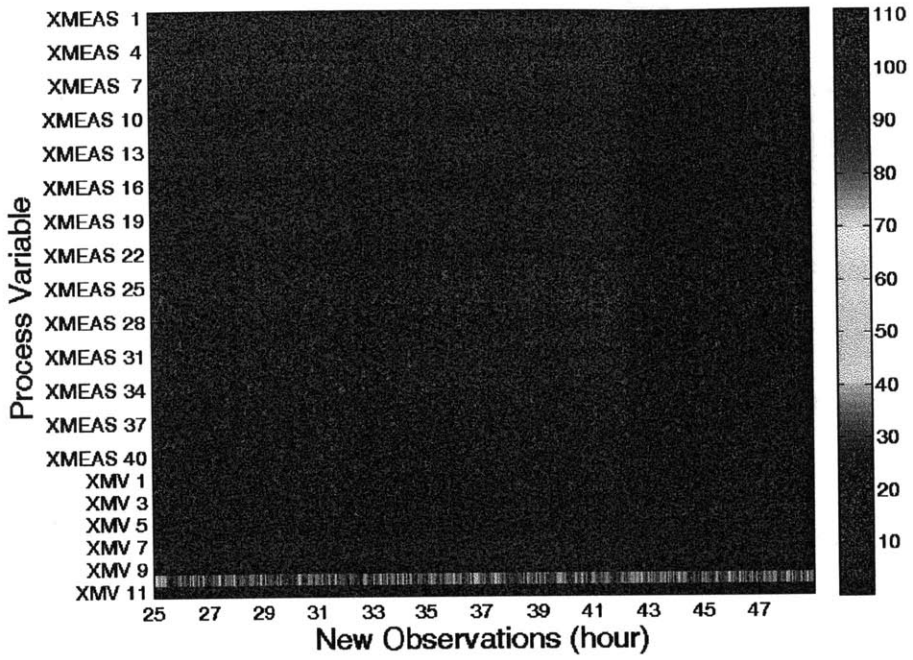

Figure 8.6 2D contribution map for Fault #4.

The implementation of the 2D contribution map is briefly summarized by the pseudo-code in Table 8.1.

8.4 Final Remarks

The 2D contribution map provides an alternative means of plotting fault contributions compared to the 1D contribution plot. By plotting multiple observations (time series data) on the same map, control engineers can more accurately identify the most impacted variables directly, and potentially gain more understanding of the fault and how its effects are propagated through the system.

Table 8.1 Pseudo-code for implementation of the 2D Contribution Map.

```
% pretreat the testing data (auto-scaling)
X = pretreat(X);
% calculate the contributions
[m, n] = size(X);
CONT = zeros (m, n);
for k = 1:m          % for each new observation k
   t = P * X(k, :)';
   cont = zeros(a, n)
   for i = 1:a       % for each principal component
      for j = 1:n    % for each process variable
         cont(i, j) = t(i) * X(k, j) * P(j,i)  / σ_i^2;
         cont(i, j) = cont(i, j) * (cont(i, j) > 0);
      end
   end
   CONT(k,:) = sum(cont,1);
end
% plot the 2D contribution map
imagesc(CONT');
xlabel('New Observations (hour)');
ylabel('Process Variable');
```

There are alternative means for calculating the contributions [5]. While the details of the formulas may be different, the idea of the 2D contribution map is universally applicable. Complementary to the T^2 statistic, the Q statistic, which captures faults in the residual space corresponding to the $m - a$ smallest singular values, can also employ the contribution map for fault identification in a similar manner.

It is the authors' opinion that every control engineer should receive some training in fault detection and diagnosis, and that the multivariable statistical methods, as well as classical Shewhart, EWMA, and CUSUM control charts, should be the covered at a

minimum. Preferably, this content is contained in a course devoted to the topic of fault detection and diagnosis, which should be a component of any undergraduate or graduate control curriculum. If such a course is not offered, then the content should be covered in one to two lectures of an introductory controls, systems engineering, or data analysis course. At the authors' institution, this material is covered in the modeling and data analysis section of an introductory systems engineering course mostly taken by first-year graduate students.

APPENDIX CHAPTER 9

A DAE-BASED METHOD OF CHARACTERISTICS APPROACH FOR THE EFFICIENT SIMULATION OF POPULATION BALANCE MODELS

Abstract Significant effort has been directed towards the development of simulation methods for population balance models (PBMs), due to their ability to describe phenomena in a wide variety of technologically important particulate processes. This paper proposes using the method of characteristics (MOCH) to transform the PBM into a system of differential-algebraic equations (DAEs) for the computationally efficient simulation of coupled population balance models and mass conservation in one step. The proposed MOCH approach is especially advantageous for the simulation of processes with growth rate that is a nonlinear function of size. The high accuracy and computational speed is demonstrated for four systems that exhibit various combinations of size-dependent growth, secondary nucleation, and agglomeration. The MOCH approach extends to particulate processes described by PBMs with one or more internal coordinates conveniently and enables on-line applications of parameter estimation, state estimation, and real-time optimization-based control.

9.1 Introduction

Particulate processes are ubiquitous in chemical engineering and include crystallization,[130] aerosols,[131] living cell dynamics,[132] and polymerization.[100,

133] Population balance models (PBMs) are commonly used to describe the dynamics of such processes. The product quality typically depends on the particle size distribution (PSD), and considerable efforts have been devoted to engineering of the PSD.[130, 134] Among the various particular processes, probably one of the most heavily studied in recent years is the modeling, prediction, and control of the size distribution for crystallization processes, given its importance in the development of pharmaceutical products.[135, 136]

In the modeling of particulate processes, population balance models have the general form[137]

$$\frac{\partial f(x,t)}{\partial t} + \frac{\partial\left(G(x,t)f(x,t)\right)}{\partial x} = h\left(f(x,t),x,t\right) \tag{9-1}$$

where $f(x,t)$ is the population distribution (density) function, $G(x,t)$ is the growth rate function, t is time, x is the internal coordinate (e.g., length, volume, mass, age), and h is the rate of generation or disappearance of particles, which typically involve nucleation, aggregation, agglomeration, coalescence, and/or breakage.

Several types of solution techniques have been developed for solving the population balance models, including the method of moments,[101, 138, 139] discretization methods,[137, 140-142], and Monte Carlo methods.[143, 144] The method of moments, such as the standard method of moments (SMM) and the quadrature method of moments (QMOM), converts the partial integro-differential equation into a set of ordinary differential equations (ODEs) for the moments. Very often these moment equations do not form a closed finite number of ODEs. The QMOM is probably the most

popular method for deriving a closed set of ODEs in the method of moments, by applying a quadrature approximation of the distribution function.[101] The moment equations alone only allow average properties of the particles to be computed, such as mean length or mean surface area. Although techniques for reconstruction of the size distribution from moments are available, they require a large number of moments, typically do not ensure a unique solution, and have numerical problems for multimodal distributions.[145, 146] Discretization methods such as finite difference and finite volume methods solve the PBMs directly and can simulate the size distribution dynamically, but are more computationally expensive and can exhibit numerical diffusion or dispersion.[137] More advanced numerical schemes such as the parallel high-resolution finite volume method was proposed to reduce the computational time and increase numerical accuracy.[140, 141, 147] Another well-known discretization method is the method of classes,[148, 149] which is a variation of a first-order-accurate finite volume method and the numerical method of lines. While some discretization methods are much faster and/or more accurate than others, all such methods exhibit some distortion in the shape of the distribution.

Advances in particle sensor technology have enabled the on-line acquisition of data that has inspired an increase in efforts to utilize such information in real-time optimization and control.[135] Real-time simulation and optimization of the PSD would be facilitated by having even faster PBM solvers, which has resulted in a resurge in interest in a rather old method known as the *method of characteristics* (MOCH).[145, 150-154] An early work that employed MOCH discretized the size into bins and integrated the population density function within each bin to generate a set of ODEs.[150] This combined MOCH-discretization approach had improved accuracy compared with

some finite discretization methods that had been previously proposed in the literature.[151, 155] Another approach combines the MOCH and finite volume methods for modeling processes with nucleation, growth, and aggregation.[156] Those studies did not include the mass conservation equation and its impact on the supersaturation (and, as a result, growth rates). In growth-only crystallization processes with size-independent growth, the MOCH was used to solve a PBM that included the effect of impurities.[152] To take into account the mass conservation constraint, MOCH has also been combined with SMM to simulate crystallizations with size-independent growth and nucleation.[153] An extension combined the QMOM and the MOCH for simulating crystallizations with size-dependent growth and nucleation.[145, 154] Such combined moments-MOCH approaches require two steps: pre-solve the moment equations to obtain the supersaturation and the lower order moments, and subsequently use the supersaturation information in the MOCH simulation.

This chapter proposes a method-of-characteristics approach for efficiently modeling the size distribution evolution in complex particulate processes involving size-dependent growth, nucleation, and agglomeration, without combination with other methods such as finite volume methods, SMM, and QMOM. The PBM is converted into a differential-algebraic equation (DAE) system that allows the simultaneous simulation of both the entire size distribution and the solute concentration. The solution technique is demonstrated for four examples with representative mechanisms that arise in particulate systems, including growth, growth and nucleation (cooling crystallization with both size-independent and size-dependent growth), growth and agglomeration (aerosol system), and lastly temperature-dependent growth in a crystallization.

9.2 Population Balance Model with the Method of Characteristics

The method of characteristics requires finding the *characteristics* in the *x-t* plane such that the partial differential equation (PDE) can be converted into a set of ordinary differential equations (ODEs). Along the characteristic curves, the ODEs with initial conditions are solved and transformed back to construct the solution of the original PDE.[157] Using the product rule, the population balance Equation 9-1 can be rewritten as

$$\frac{\partial f(x,t)}{\partial t} + G(x,t)\frac{\partial f(x,t)}{\partial x} = -f(x,t)\frac{\partial G(x,t)}{\partial x} + h\big(f(x,t),x,t\big) \tag{9-2}$$

The identification of the characteristics is straightforward and the systems of equations are generated as[145, 150, 153]

$$\frac{dx}{dt} = G(x,t) \tag{9-3}$$

$$\frac{df(x,t)}{dt} = -f(x,t)\frac{\partial G(x,t)}{\partial x} + h\big(f(x,t),x,t\big) \tag{9-4}$$

where the initial conditions for x and f are obtained from the initial size distribution, with $x(0) = x_0$ and $f(x,0) = f_0(x)$. For each characteristic x, there is a pairing f.

The functions G and h are usually dependent on other variables, such as particle size, size distribution, and solute concentration. To complete the model equations for the system, mass conservation equations must also be satisfied. We propose to implement any mass conservation equations as algebraic constraints that are simultaneously solved

with the characteristic equations (3)-(4) as a system of differential-algebraic equations (DAEs). For example, when the length L is chosen as the internal coordinate, the solute concentration can be related to the third-order moment μ_3 by the mass conservation constraint

$$C(t) = C(0) - \rho k_v \left(\mu_3(t) - \mu_3(0)\right) \tag{9-5}$$

where ρ is the density of the solid phase and k_v is the shape factor, and consistent units for the solute concentration C and the number density function f are used (e.g., both based on per mass solvent). The third-order moment μ_3 is expressed as an integral of the distribution function:

$$\mu_3(t) = \int_0^\infty f(L,t) L^3 dL \tag{9-6}$$

Equation 9-5 is coupled to the characteristic Equations 9-3 and 9-4 by the third-order moment. In most particulate processes, the growth rate G is dependent on the solute concentration. As a result, the model equations 9-3 to 9-6 are tightly coupled, which means that large errors arise from any attempt to solve one set of these equations independently of the other. In our proposed method, 9-3 to 9-6 would be the set of equations to be simulated.

Before describing how our method handles the integral in Equation 9-6, it is useful to describe the most closely related alternative method, which is a combined QMOM and MOCH approach[145] in which the moment equations are pre-solved for the entire time range to obtain the third-order moment and solute concentration. The results

of the third-order moment and solute concentration were subsequently supplied to solve the characteristic equations. To deal with size-dependent growth, the QMOM approximates the distribution function using a quadrature approximation,

$$f(L,t) = \sum_{i=1}^{N_q} w_i \delta\left(L_i(t), L\right) \tag{9-7}$$

with N_q being the number of quadrature points with each point containing a weight w_i and abscissa L_i. As a result, the third-order moment is then given by

$$\mu_3(t) = \int_0^\infty f(L,t) L^3 dL \approx \sum_{i=1}^{N_q} w_i L_i^3 \tag{9-8}$$

In the QMOM approach, the quadrature approximation is re-evaluated at each time step to obtain new weights and abscissas, using either the product-difference algorithm[101, 158] or a differential-algebraic equations approach.[138]

In contrast, our proposed strategy calculates the third-order moment during real-time simulation of the evolution of the size distribution, ***which completely avoids the need to pre-solve the moment equations***. By choosing N length characteristics (which give N pairs of L and f equations), the size distribution at any time is fully described by the N points and the distribution information can be directly utilized to obtain the third-order moment (or any other moments) accurately using any quadrature method, with the simplest being

$$\mu_3(t) = \sum_{i=1}^{N} f(L_i, t) L_i^3 \Delta L_i \tag{9-9}$$

Our DAE-based method-of-characteristics approach solves the population balance models efficiently, without simulating any moment equations and without approximating any derivatives of the distribution function *f*. The next section discusses some implementation details and the drawbacks of the heavily used alternative differential forms of the conservation Equation 9-5.

9.3 Numerical Methods and Algorithm

Our method employs conservation equations as algebraic constraints rather than as differential equations, to produce an index-1 DAE system to be solved. Equations 9-3, 4, 5, and 9 define an index-1 DAE system to be solved where the mass conservation (Equation 9-5) is the algebraic constraint. Taking a time derivative of Equation 9-5 would convert the DAE system into an ODE system, as

$$\frac{dC}{dt} = -\rho k_v \frac{d\mu_3}{dt} \tag{9-10}$$

When the growth rate function *G* has either no or linear dependency on size, the moment equations close and the $d\mu_3/dt$ term can be reduced, as commonly seen in the literature for PBMs.[130] For example, in size-independent growth case, Equation 9-10 reduces to the heavily used expression

$$\frac{dC}{dt} = -3\rho k_v G \mu_2 \tag{9-11}$$

where μ_2 is the second-order moment. However, with a more complicated size-dependency in the growth rate, a reduction such as (9-11) no longer holds. The $d\mu_3/dt$ term in (9-10) could be explicitly computed from the method of moments, which introduces error in the solute balance due to the approximations used to enforce closure,[10-12, 18] or could be computed from a discretized equation such as (9-9), which introduces time-discretization error that results in loss of mass conservation in the system unless the time interval Δt is very small. The algebraic Equation 9-5 has none of the numerical error associated with time discretization used to numerically solve Equation 9-10, and any DAE solver automatically sets its tolerances on the algebraic equations to be very small, so that mass conservation holds nearly exactly even for large values for the time interval Δt.

The idea of MOCH is usually illustrated by plotting the length characteristics (L-t relationships).[145, 152, 153] The length characteristics could be grouped into two types (Figure 9.1), which correspond to different mechanisms in the population balance models. In a system with growth and nucleation, the characteristics curve of the first type starts on the length L-axis and corresponds to the growth of any initial particles present in the system (such as crystal seeds). The characteristics curve of the second type originates from the time t-axis, and represents the new particles generated via mechanisms such as nucleation followed by growth. The characteristics curve on the t-axis does not need to be tracked in simulations when the mechanism of new particle formation (e.g., nucleation) is absent in the system.

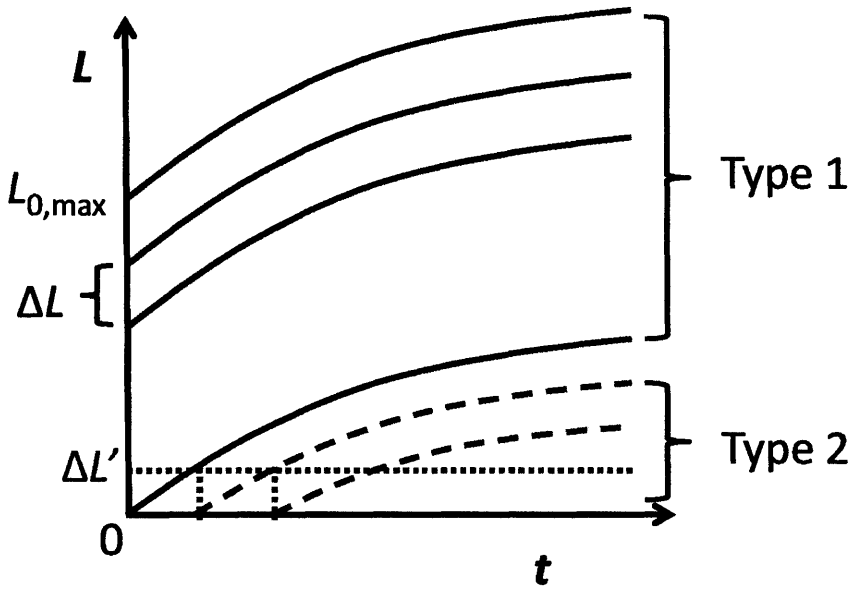

Figure 9.1 Evolution of characteristics lines originating from the length L-axis (for initial particles, denoted as Type 1) and time t-axis (for new-born particles, denoted as Type 2).[145]

The algorithm for constructing the system of equations is illustrated in Figure 9.2. For an initial distribution f, the initial length is sampled with N_1 points by using a length interval ΔL. An equal length interval ΔL is not required by the MOCH method, but could be chosen for convenience of implementation. Typically, the value of ΔL can be chosen much larger than those in finite difference or finite volume methods (as demonstrated later in Example 1). Those points correspond to the first-type characteristics on the L-axis in Figure 9.1. Each sampled point gives two ODEs associated with the length and distribution function (Equations (3) and (4)), and as a result the N_1 sampled points of the initial distribution gives $2N_1$ ODEs with corresponding initial conditions.

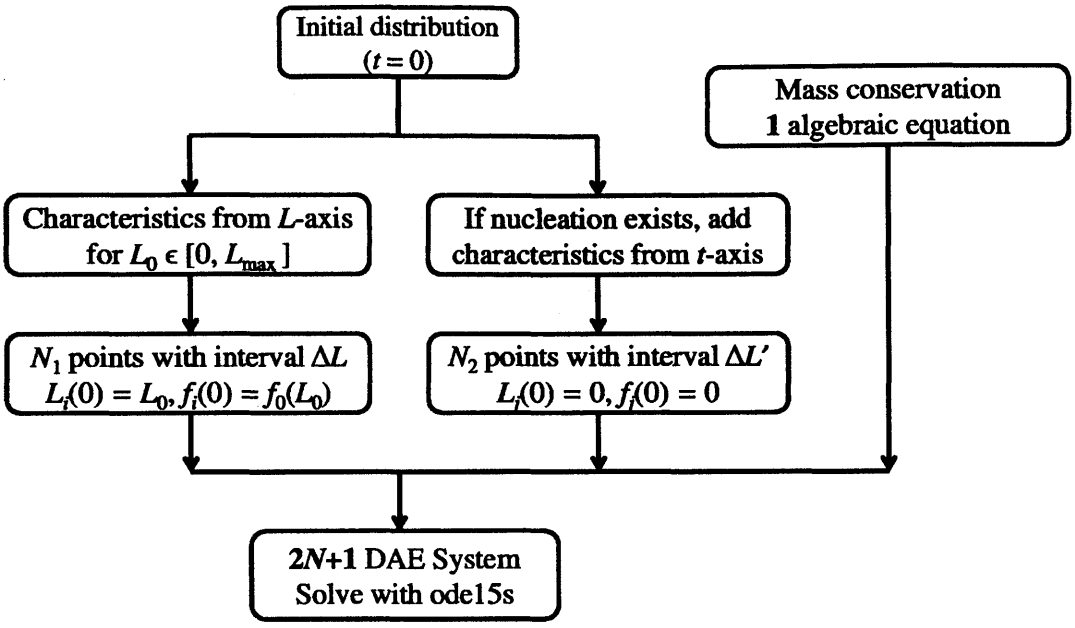

Figure 9.2 Procedure for construction of the DAE system for simulation of the population balance model with the method of characteristics illustrated with a growth-nucleation system.

If nucleation exists in the system, N_2 characteristics are generated for the second-type characteristic curve. The second type characteristics will add another $2N_2$ ODEs to the DAE system. For the N_2 second-type characteristics, the initial values of the length and density function are initialized as zero (consider that those characteristics are inactive until certain time points during the crystallization). The value of N_2 can be determined by dividing an expected lower bound on the final size of the initial crystal seeds with an length interval $\Delta L'$, which specifies that a characteristic curve becomes active when the previous characteristic grows to the size of $\Delta L'$ (Figure 9.1). The values of $\Delta L'$ are user-defined depending on how frequent the nucleation points are created compared with the

initial particles. One choice for $\Delta L'$ that is convenient for implementation is the maximum size of nuclei r_0.[145]

The generated $2N$ ODEs (N=N_1+N_2) together with the mass conservation Equation 9-5 constitute a differential-algebraic equation system with index 1. Such a system is conveniently handled by available commercial solvers, and ode15s in Matlab was chosen in this study for its general availability.

Calling ode15s involves defining the mass matrix in the DAE system, $\boldsymbol{M\dot{y} = F(t,y)}$, which is

$$M = \begin{bmatrix} I_{2N} & 0 \\ 0 & 0 \end{bmatrix}$$

where I_{2N} is the $2N$-by-$2N$ identity matrix. The solution of a DAE system using ode15s requires a consistent initial condition; for our particular system with index one, the consistent initial condition is satisfied by the initial mass balance.

9.4 Numerical Examples

Four examples are used to demonstrate the applications of the proposed MOCH approach for simulation of the PDEs associated with various population balance models. The particular examples are chosen to cover some representative mechanisms of particulate processes, while the method itself is general and applicable to other mechanisms. The first example considers particle growth, where a growth-dominated process with well-controlled constant supersaturation is used to verify the accuracy and efficiency of the

DAE-based MOCH approach by comparing with both the analytical solution and standard finite volume method. Then growth and nucleation are simulated for cooling crystallization processes, where size-independent growth and size-dependent growth show very different final crystal size distributions. The third example is a simultaneous growth and aggregation process for aerosol system. In the last example, the temperature effect on the crystal size distribution is simulated and discussed.

9.4.1 Example 1. Growth-Dominated System with Size-Dependency

A seeded process where nucleation is insignificant is often referred to as being *growth-dominated*. The size-dependent crystal growth rate is nearly always assumed in the literature to have the form

$$G = k_g S^g (1+\gamma L)^p \tag{9-12}$$

where S is the supersaturation (defined as ΔC, the difference between the concentration and solubility), and k_g, g, γ, and p are growth parameters. Size-independent growth is a special case included in the expression by simply setting γ to zero. Using feedback control, the supersaturation over the whole batch could be controlled accurately.[159-161] For such a process, the analytical solutions of the length characteristics and population density function can be obtained.[145] In particular, when $p = 1$,

$$L(t) = \frac{1}{\gamma}\left((1+\gamma L_0)\exp\left(\gamma k_g S^g t\right) - 1\right)$$

$$f(t) = f_0(L_0)\exp\left(-\gamma k_g S^g t\right) \tag{9-13}$$

which is equivalently written as

$$f(t,L) = f_0\left(\frac{(1+\gamma L)\exp(-\gamma k_g S^g t)-1}{\gamma}\right)\exp\left(-\gamma k_g S^g t\right) \qquad (9\text{-}14)$$

Table 9.1 Simulation parameters for a growth-dominated system with size-dependent growth in Example 1.

Parameter		Value
Density of solid	ρ	10^{-12} g/μm^3
Shape factor	k_v	0.6
Initial concentration	C_0	0.1 g/g solvent
Lumped growth constant	$k_g S^g$	0.02 μm/s
Size dependency of growth	γ	0.005
Size dependency power	p	1
Length interval for N_1	ΔL	1.5 μm

A Gaussian distribution was used as the initial number density f, with mean size of 90 μm and standard deviation of 8 μm. The constraint of a constant supersaturation was implemented by using a lumped growth constant $k_g S^g$ of 0.02 μm/s. The crystal size distribution simulated using the DAE-based MOCH approach completely overlaps with the analytical results for a growth-dominated system (see Figure 9.3, with simulation parameters in Table 9.1). The only difference between the MOCH and exact analytical solution would be associated with numerical roundoff and the numerical solution of a DAE system; numerical roundoff errors are vanishingly small for a double-precision calculation and the error in the numerical solution can be set to be <0.00001% by setting the error tolerance on the DAE solver.

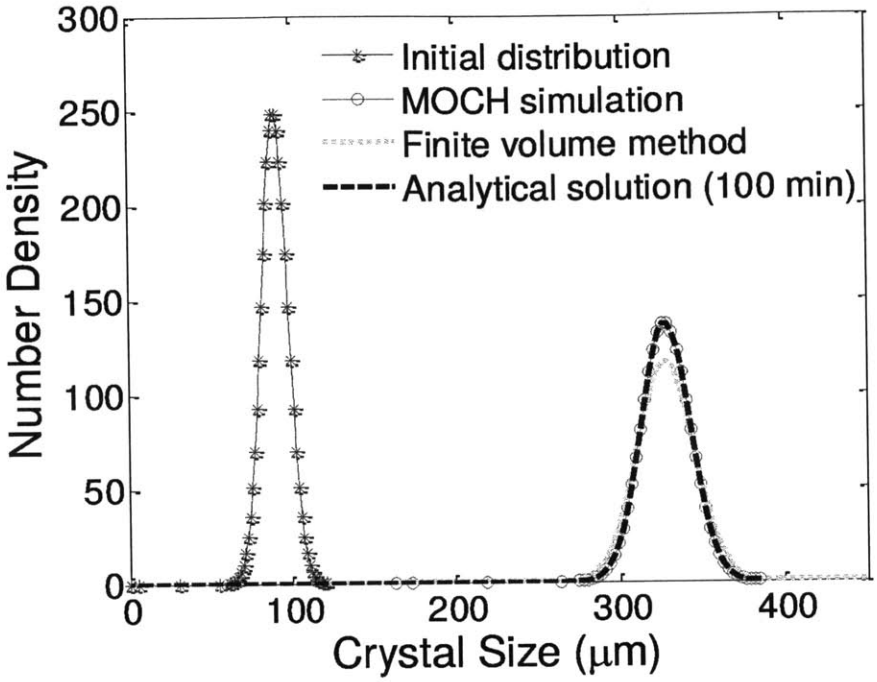

Figure 9.3 Simulation of a growth-dominated system (Example 1) overlaps with the analytical solution and is more than three orders-of-magnitude faster and more accurate than the finite volume method.

As a result of the size-dependency of the growth, the number density distribution flattens as the crystals grow (see Figure 9.3). The simulation technique using the method of characteristics completely avoids numerical dispersion or diffusion, which occurs in some extent in any discretization of the internal coordinates, such as occurs in the method of classes, finite difference, and finite volume methods. For comparison, the standard finite volume method is simulated and plotted in Figure 9.3, where significant numerical error is observed even with mesh size that is 1/8 of the ΔL used in the DAE-based MOCH approach. The finite volume method discretized the length coordinate and resulted in a set of ODEs that are solved.[155]

Another advantage of the DAE-based MOCH approach is that the solution of the DAE system is highly computationally efficient (computation time is 0.024 s for the DAE-based MOCH approach and 51.3 s for the finite volume method in Example 1, with the latter being >2000 times more expensive and having large numerical error). In the MOCH approach, the discretization of the length is only needed for the initial length range where f is nonzero, and the circle and star markers have one-on-one correspondence in Figure 9.3. In the finite volume method, the discretization was performed on the entire length coordinate (up to a maximum crystal size of interest by the end of the simulation) with a much smaller length interval. The finite volume method generated significantly more equations (2400) compared with that of the MOCH approach (111), which results in the greatly increased computational cost.

9.4.2 Example 2. Growth and Nucleation during Cooling Crystallization

Growth and new particle generation are common in many particulate systems, including living cells and crystallization processes. This example considers size-independent/size-dependent growth and secondary nucleation, with the latter typically expressed as

$$h = k_b S^b \mu_3 \delta(r_0, L) \tag{9-15}$$

with the h being the right-hand side of Equation 9-4 and k_b and b are nucleation parameters. The δ function is the Dirac delta function at r_0,[141] or a modified delta function (1 if L is less than or equal to r_0 and 0 elsewhere).[145] While such treatments could simplify the nucleation modeling, they exclude the fact that in reality the nuclei

may be formed with a more general size distribution. To accommodate this consideration, a smooth size distribution of the nuclei was assumed as

$$h = \alpha k_b S^b \mu_3 \left(-\frac{4}{r_0^2}\left(L - \frac{r_0}{2} \right)^2 + 1 \right) \text{ for } 0 \le L \le r_0 \qquad (9\text{-}16)$$

where α is a constant that ensures the consistency of the total generated seeds in equation (9-15). For a Dirac delta function in equation (9-15), α is 3/2. Compared with the commonly used delta function approximations of the nucleation distribution, this smooth representation also allows a fast convergence in the DAE solver by eliminating possible discontinuities in the ODEs of number density functions of the second-type characteristics.

A cooling crystallization process is considered in this example, in which the liquid solution is cooled with a constant rate from 30°C to 10°C, and the solubility of the crystallizing compound decreases linearly with temperature over the range (see solid line in Figure 9.4). Note that the approach applies to any solubility curve and temperature profile. The simulation is formulated and implemented as described in Figure 9.2, and the parameters are summarized in Table 9.2. The parameter values for growth and nucleation are based on the published values for potash alum in water.[145] Both simulated systems with size-dependent or size-independent growth started at the same initial conditions. The trends in the concentration evolution in Figure 9.4 are quite similar, with an initial large supersaturation that reduced quickly as a result of crystal growth and nucleation. The size-dependent growth case experienced a faster drop in concentration and supersaturation. For size-independent growth, the initial number density distribution peak

migrates towards higher length values while maintaining the exact shape (see Figure 9.5a). A second peak of crystals is generated by nucleation and growth. The number density of the crystals generated by nucleation greatly exceeds the number density of initial crystals. When converted to the volume fraction distribution, the volume of nucleated crystals is comparable to that of the initial crystals after growth (Figure 9.5b). The conversion of the number density distribution to volume distribution is carried out by

$$f_{v,i} = f_{n,i}L_i^3 \Big/ \sum_{j=1}^{N}\left(f_{n,j}L_j^3\Delta L_j\right) \tag{9-17}$$

Table 9.2 Simulation parameters for the growth-nucleation systems in Example 2.

Parameter		Value
Crystal density	ρ	10^{-12} g/μm^3
Shape factor	k_v	0.6
Initial concentration	C_0	0.1 g/g solvent
Growth rate constant	k_g	10 μm/s
Growth order constant	g	1
Size dependency of growth	γ	0 (size-independent), 0.005 (size-dependent)
Size dependency power	p	1
Nucleation rate constant	αk_b	0.038 (μm^{-3}s^{-1})
Nucleation order constant	b	3.4174
Length interval for N_1	ΔL	3 μm
Length interval for N_2 (= r_0)	$\Delta L'$	3 μm

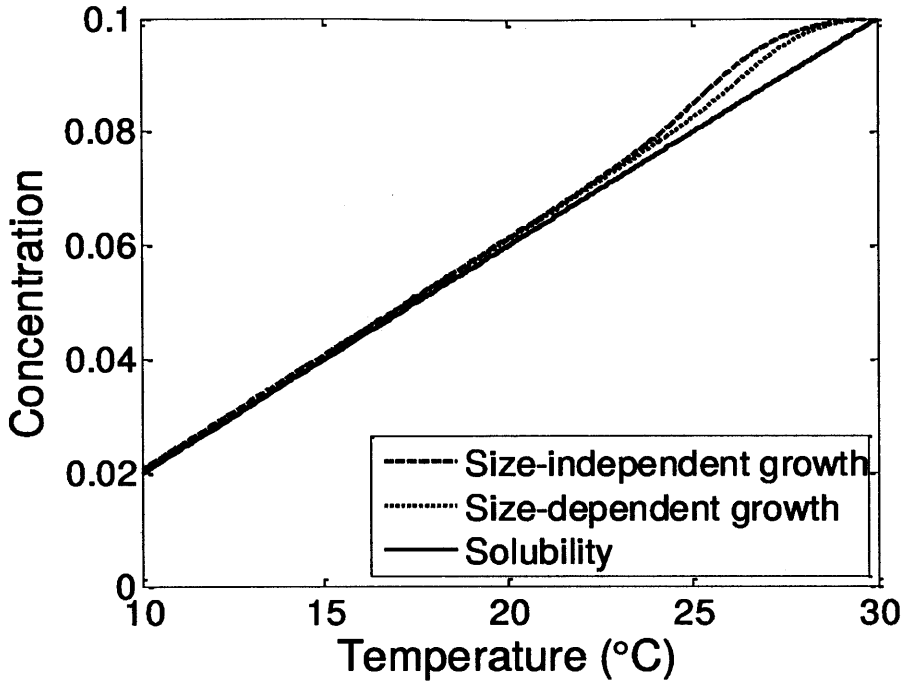

Figure 9.4 Concentration evolution curve along with the temperature change for size-independent growth (blue dash) and size-dependent growth (red dot) in Example 2.

The distribution of the nucleated crystals for the size-dependent growth case has a much lower peak value (see Figure 9.6a), which indicates that a lower number of crystals was nucleated compared with the size-independent case. The reduction in the nucleation rate occurred as an immediate result of the lower supersaturation levels in the size-dependent growth case (Figure 9.4). The size dependency of growth has a negative feedback on the supersaturation level that leads to a faster supersaturation drop. This effect also leads to a redistribution of the crystallized solute mass among the initial crystals and nucleated crystals. The volume fraction of crystals due to secondary nucleation is much smaller for the size-dependent growth case (cf. Figures 5b and 6b).

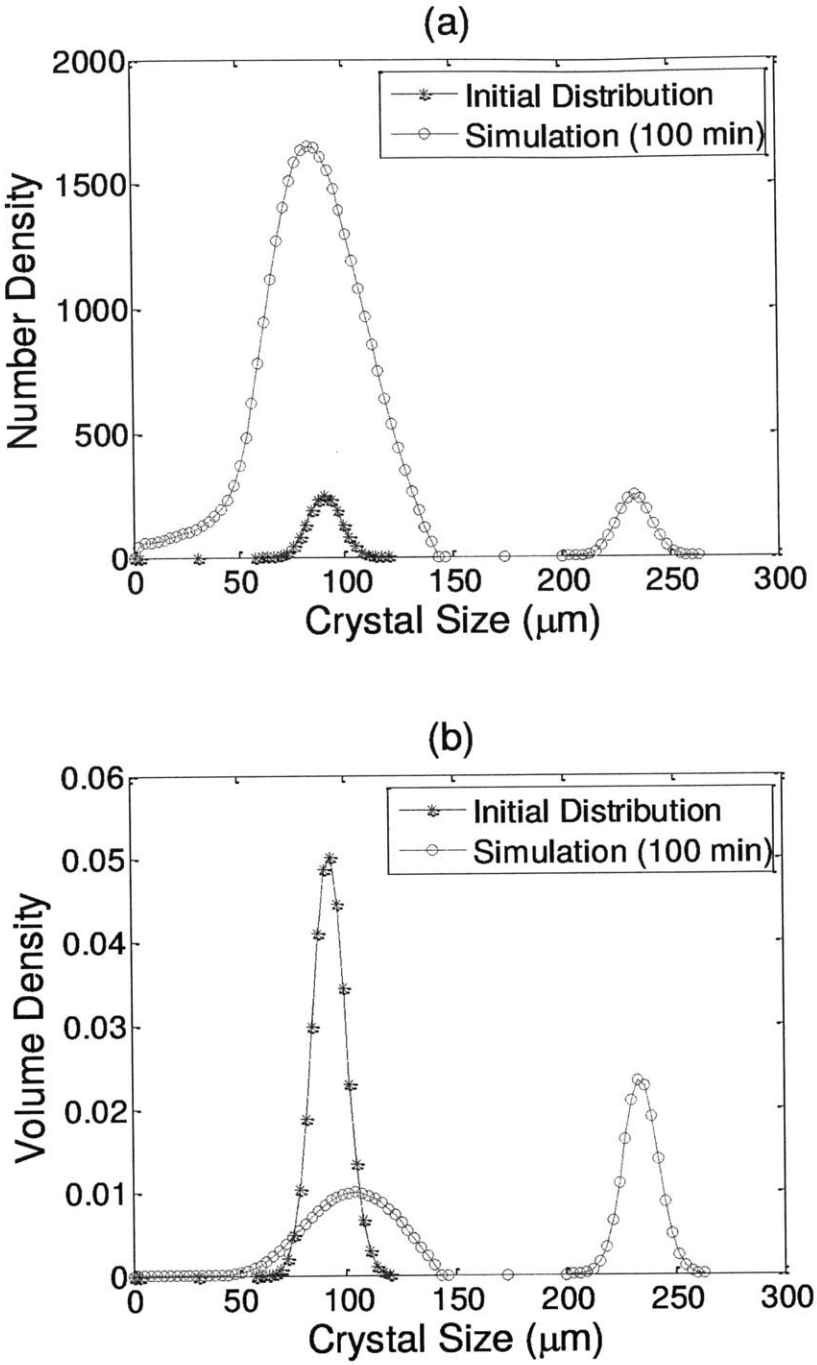

Figure 9.5 Simulated crystal size distribution of the growth-nucleation system in Example 2 with size-independent growth: (a) number density distribution and (b) volume distribution.

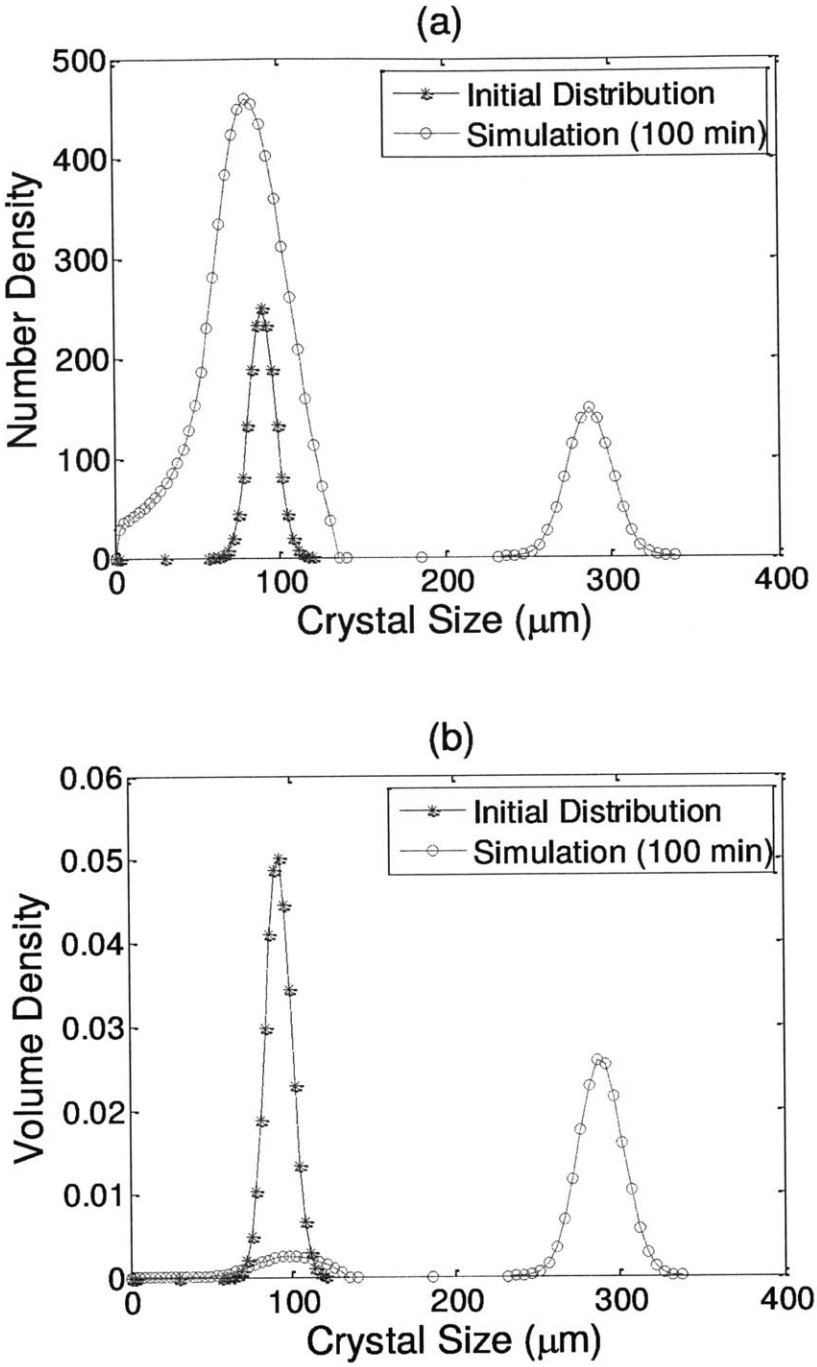

Figure 9.6 Simulated crystal size distribution of the growth-nucleation system in Example 2 with size-dependent growth: (a) number density distribution and (b) volume distribution.

The time evolution of the length characteristics for both cases is plotted in the *L-t* plane in Figure 9.7. For size-independent growth, the characteristics curve of the initial crystals evolves at the same rate and keeps the same distance from each other (Figure 9.7a). Such a constant distance is not maintained for size-dependent growth, with stretching being more significant at higher lengths (see Figure 9.7b). Very sparse sampling (only a few characteristics curves) for the initial crystal size between 0 and 60 μm was used, considering that the number density functions are zero for the region. For the characteristics curves generated on the time axis, the spacing was enlarged along the time axis, due to the slowdown of crystal growth at later times. This behavior of enlarging time intervals among the characteristics on the time axis was also observed in the combined QMOM-MOCH approach.[145]

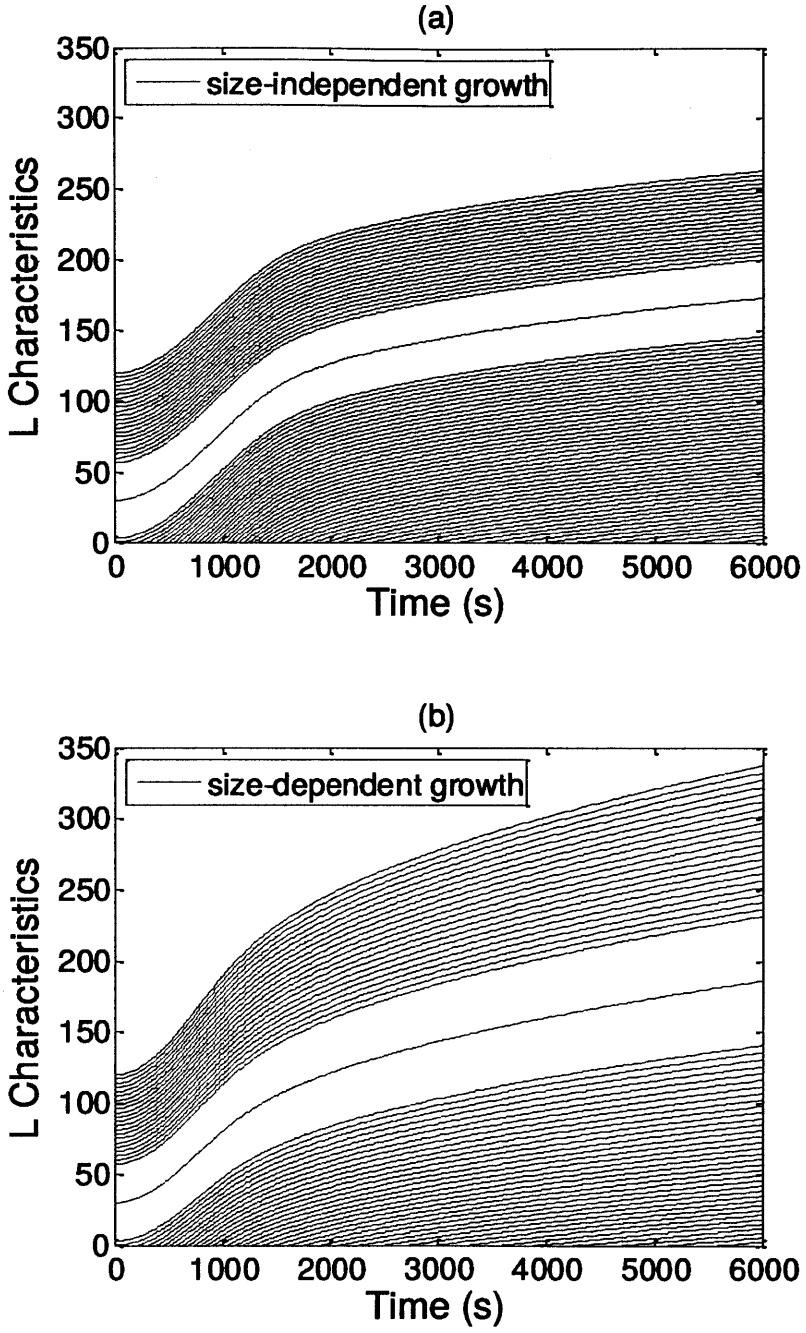

Figure 9.7. Length characteristics for secondary nucleation and (a) size-independent growth and (b) size-dependent growth (Example 2).

9.4.3 Example 3. Growth with Agglomeration

The agglomeration (or aggregation) of particles is a more complicated phenomenon that often occurs during particulate processing. For such processes, the particle volume is usually used as the internal coordinate in the population balance model, although length could be used by converting from the volume.[142] A convenience of using volume is that the total volume is conserved during particle agglomeration rather than the length. The mathematical form of agglomeration is expressed as the generation of larger particles from smaller particles and the disappearance of small particles that participated in the process:

$$B(v,t) = \frac{1}{2}\int_0^v \beta(v-\varepsilon,\varepsilon) f(v-\varepsilon,t) f(\varepsilon,t) d\varepsilon \tag{9-18}$$

$$D(v,t) = f(v,t)\int_0^\infty \beta(v,\varepsilon) f(\varepsilon,t) d\varepsilon \tag{9-19}$$

This example considers particles that grow and aggregate at the same time. For the purpose of numerical demonstration, an aerosol example is chosen for which an analytical solution is available for comparison.[131] The same example has been used in previous PBM simulation studies using the high resolution finite volume method.[137] The initial number density distribution is

$$f_0(v) = \frac{N_0}{v_0} e^{-v/v_0} \tag{9-20}$$

where N_0 and v_0 are parameters that specify the initial total number of crystals and mean volume, respectively. At a constant growth rate with size-independent agglomeration kernel, an analytical solution of equation (9-18) is[131]

$$f(v,t)=\frac{M_0^2/M_1}{1-2\Lambda v_0}\exp\left[-\frac{\frac{M_0}{M_1}\left(v-2\Lambda\left(\frac{N_0}{M_0}-1\right)\right)}{1-2\Lambda v_0\left(\frac{N_0-M_0}{M_1}\right)}\right] \tag{9-21}$$

$$\Lambda=\frac{G_0}{\beta_0 N_0 v_0}$$

$$M_0=\frac{2N_0}{2+\beta_0 N_0 t}$$

$$M_1=N_0 v_0\left[1-\frac{2G_0}{\beta_0 N_0 v_0}\ln\left(\frac{2}{2+\beta_0 N_0 t}\right)\right]$$

The number density of the growth-agglomeration example was simulated with the parameters in Table 9.3. In this example, a volume interval Δv instead of a length interval is used to generate the sampled points on a size range that includes the expected maximum particle size. Because of the equal interval between the sampled points, the convolution integral in (9-18) is conveniently handled by using a built-in command in Matlab (conv) that operates on the vector with f_i as its elements. The simulated size distribution completely overlaps with the analytical results (see Figure 9.8). This example demonstrates again the advantage of being free from numerical diffusion or dispersion with the DAE-based MOCH approach, which is especially important in handling distributions that have discontinuities, which typically requires special techniques in

discretization methods.[137] Due to the constant agglomeration kernel, the volume distribution flattens out very fast (see Figure 9.9).

Table 9.3 Simulation parameters for the growth-agglomeration systems in Example 3.

Parameter		Value
Initial distribution parameter	N_0	1000
Initial distribution parameter	v_0	100 μm^3
Constant growth rate	G_0	1 $\mu m^3/s$
Constant agglomeration kernel	β_0	1 s^{-1}
Volume interval for N_1	Δv	2 μm^3

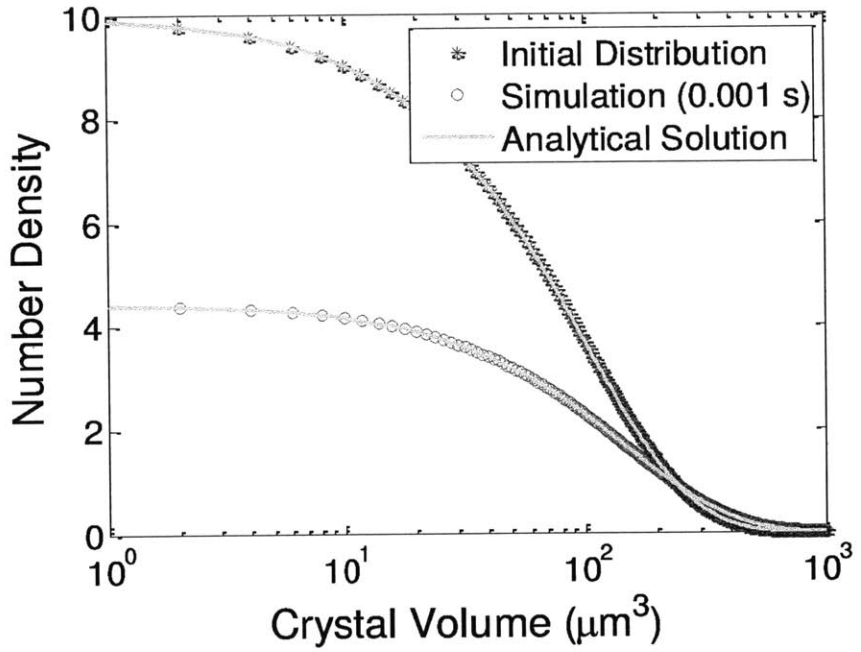

Figure 9.8 The simulated number density distribution of the growth-agglomeration system in Example 3 overlaps with the analytical solution.

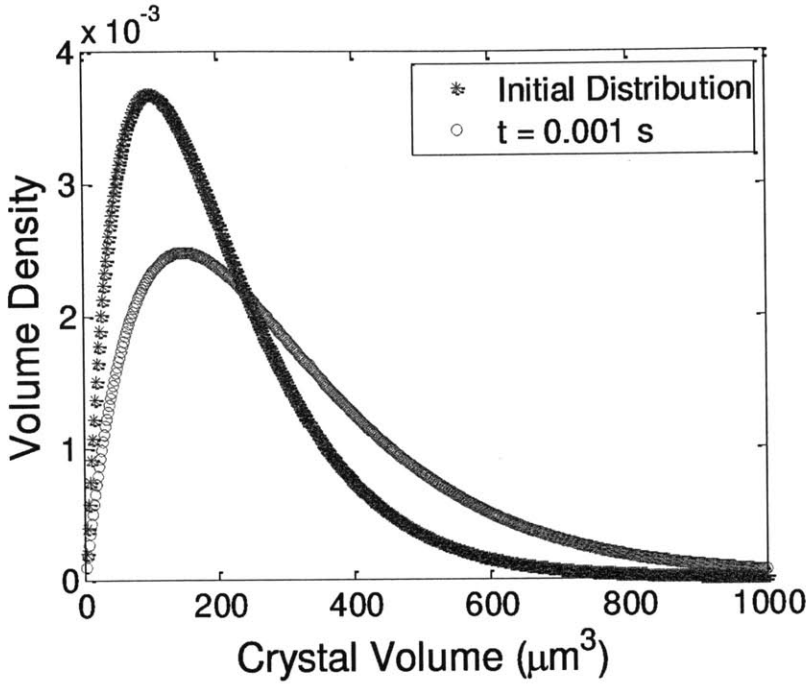

Figure 9.9 Simulated volume distribution of the growth-agglomeration system in Example 3.

9.4.4 Example 4. Temperature Effect on Growth Rates

During a cooling crystallization process, the temperature typically drops over a wide range. Experimental studies carried out at constant supersaturation have shown reduced growth rate at lower temperatures.[160] The temperature dependency of the growth rate constant k_g is described by Arrhenius law

$$k_g = k_{g,30} \exp\left(-\frac{E_a}{R}\left(\frac{1}{T+273.15} - \frac{1}{303.15} \right) \right) \tag{9-22}$$

where E_a is the activation energy and $k_{g,30}$ is the growth rate constant at the reference temperature of 30°C with a value of 1 μm/s. The activation energy E_a= 47.18 kJ/mol was selected as the value for the crystallization of pentaerythritol,[153] with the other simulation parameters being in Table 9.2, and the system is cooled with a constant cooling rate from 30°C to 10°C (same as in Example 2).

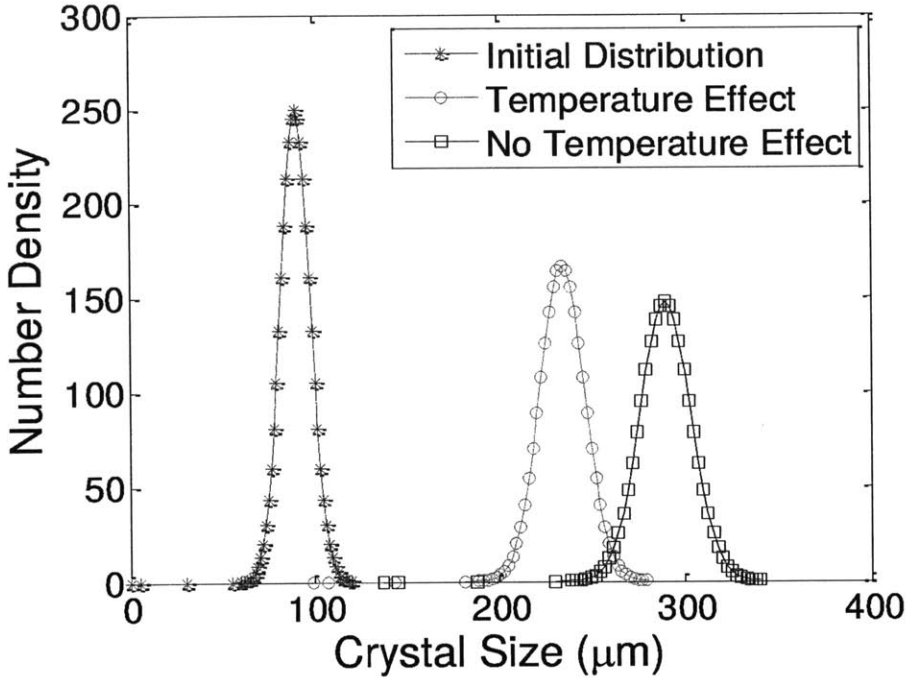

Figure 9.10 Temperature dependency of the growth kinetics greatly changes the size distribution of the product.

The distribution is located at a much smaller mean size when the temperature dependency on the growth rate is modeled (Figure 9.10). Estimates of crystallization kinetic parameters that ignore the temperature effect on growth and nucleation have their estimates including an averaged effect of temperature to some degree. Such a procedure,

although not as accurate, would be expected to work fine as long as the estimated parameters are utilized for the experiments carried out in the similar temperature range. The predictive ability of the model would be significantly lowered when a different temperature region is used. Including the temperature term not only allows more accurate parameter estimation, but also enhances the predictive value of the model.

9.5 Discussion

The MOCH approach applies to complex particulate processes with constraints such as mass conservation (and supersaturation change), and can describe various phenomenon including growth, nucleation, agglomeration (aggregation), and breakage. Agglomeration was chosen over breakage for demonstration purposes in Example 3 as it is more complicated in mathematical form. Modeling of breakage can be implemented similarly. Due to its higher accuracy and easier implementation compared to other methods, the DAE-based MOCH approach is a promising approach for use in the parameter estimation, design, and control of the size distribution for particulate processes having a very wide range of phenomena.

The DAE-based MOCH approach has a computational efficiency that is fast enough for real-time applications. The computational time for each example is much less than a minute, even for a system with agglomeration (see Table 9.4). The particular DAE solver used in the examples was an adaptive time stepper with a very low error tolerance; in applications where six decimal places of accuracy of not required, such as in real-time feedback control, the computational times could be further reduced by relaxing the error tolerance. These simulation times indicate that, by employing the MOCH, on-line

parameter estimation, state estimation, and feedback control is feasible for particulate systems with such characteristics such as side-dependent growth and agglomeration that hamper alternative simulation methods.

Table 9.4 Simulation time for the four example systems examined in the work.*

Example		N_1	N_2	N	Simulation time
Example 1	Growth-dominated system	55	0	55	0.024 s
Example 2	Size-independent growth and nucleation	25	67	92	12.28 s
	Size-dependent growth and nucleation	25	67	92	7.29 s
Example 3	Growth with agglomeration	500	0	500	4.29 s
Example 4	Temperature-dependent growth	45	0	45	0.049 s

*In Example 1, the finite volume method had to use a very small size discretization and had more than 2000 times the computational cost (51.3 s), while still giving huge numerical error (detailed discussion in Example 1). The finite volume method solved 2400 ODEs in Example 1, which is much more than used in the DAE-based MOCH approach. The cost of the finite volume method would be significantly higher for Examples 2-4 as well. In Example 2, size-independent growth used modestly more computational time than size-dependent growth. Application of the Matlab profiler indicated that the cause was the increased number of nuclei generated in the size-independent case, which resulted in the DAE solver ode15s using smaller time steps to ensure numerical accuracy. The ode15s default error tolerance was used in the simulation, which corresponds to an absolute error tolerance of 10^{-6} and a relative error tolerance of 10^{-3}.

In particulate processes with multiple internal coordinates (typically said to be *multidimensional* in the literature), methods based on discretization of the internal

coordinates[140, 141] are typically too computationally expensive to enable their use in many real-time control applications, and are even relatively slow for parameter estimation applications. The extension of the MOCH to multidimensional PBMs is straightforward. For an population balance model with any dimension N,

$$\frac{\partial f(\mathbf{x},t)}{\partial t}+\sum_{i=1}^{N}\frac{\partial\left(G_i(\mathbf{x},t)f(\mathbf{x},t)\right)}{\partial x_i}=h\left(f(\mathbf{x},t),\mathbf{x},t\right), \tag{9-23}$$

The ordinary differential equations describing the characteristics are

$$\frac{dx_i}{dt}=G_i(\mathbf{x},t) \text{ for } i=1,...,N \tag{9-24}$$

$$\frac{df(\mathbf{x},t)}{dt}=-f(\mathbf{x},t)\left(\sum_{i=1}^{N}\frac{\partial G_i(\mathbf{x},t)}{\partial x_i}\right)+h\left(f(\mathbf{x},t),\mathbf{x},t\right) \tag{9-25}$$

The algorithmic steps described in this paper (Figure 9.2) apply to the multidimensional PBM in the same way, whereas the number of equations will change due to the additional dimension(s). For illustration purposes, Example 1 is extended for a 2D case where the seed crystals have mean length of 150 μm and mean width of 90 μm. The simulation uses the same parameters from Example 1 for the two dimensions, and both size-independent growth and size-dependent growth are demonstrated in Figure 9.11. Both simulations took very little computational cost (~2 s). For size-independent growth, the entire peak maintained exactly the same shape and shifted the same distance in both the length and width directions. For size-dependent growth, the size distribution peak broadened and moved further, with more growth in the length direction due to the size-dependency.

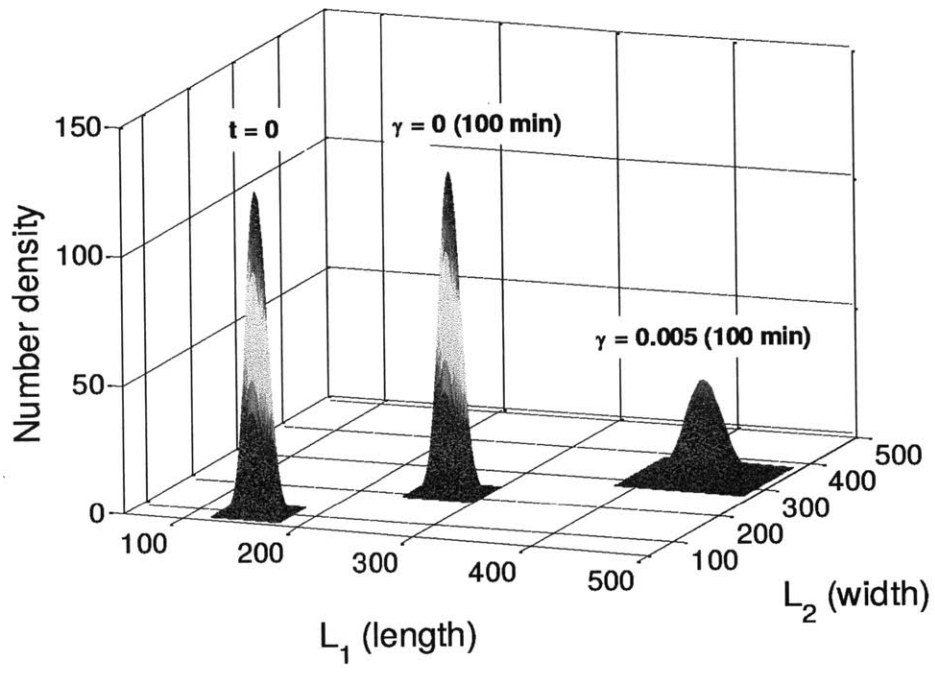

Figure 9.11 Extension of Example 1 to illustrate 2D growth with constant supersaturation control for both size-independent ($\gamma = 0$) and size-dependent ($\gamma = 0.005$) growth.

9.6 Conclusions

A DAE-based method-of-characteristics (MOCH) approach is proposed for modeling the evolution of the size distribution for particulate processes with such phenomena as size-dependent growth, secondary nucleation, and agglomeration. The approach transforms the population balance models and the mass conservation equation into a differential-algebraic equation (DAE) system, which is in particular advantageous for handling size-dependent growth problems. Compared with the widely used methods for simulation of particle size distributions, the proposed MOCH approach is more accurate (comparable to

analytical solutions) and computationally efficient. Example systems are simulated and analyzed to demonstrate the broad applications of this approach. As the method only requires the solution of a DAE system of relatively low dimension, the proposed method-of-characteristics approach is fast enough for on-line parameter estimation, real-time state estimation, and optimization-based control, and for multi-dimensional systems.

REFERENCES

[1] P. I. Lee and W. R. Good, "Overview of Controlled-Release Drug Delivery," in *Controlled-Release Technology*. vol. 348, ed: American Chemical Society, 1987, p. 1-13.

[2] R. Langer, "Drug delivery and targeting," *Nature,* vol. 392, p. 5-10, 1998.

[3] K. E. Uhrich, S. M. Cannizzaro, R. S. Langer, and K. M. Shakesheff, "Polymeric systems for controlled drug release," *Chemical Reviews,* vol. 99, p. 3181-3198, 1999.

[4] P. Gupta, K. Vermani, and S. Garg, "Hydrogels: from controlled release to pH-responsive drug delivery," *Drug Discovery Today,* vol. 7, p. 569-579, 2002.

[5] N. K. Varde and D. W. Pack, "Microspheres for controlled release drug delivery," *Expert Opinion on Biological Therapy,* vol. 4, p. 35-51, 2004.

[6] A. Gopferich, "Mechanisms of polymer degradation and erosion," *Biomaterials,* vol. 17, p. 103-114, 1996.

[7] L. S. Nair and C. T. Laurencin, "Biodegradable polymers as biomaterials," *Progress in Polymer Science,* vol. 32, p. 762-798, 2007.

[8] J. E. Sousa, P. W. Serruys, and M. A. Costa, "New frontiers in cardiology - Drug-eluting stents: Part I," *Circulation,* vol. 107, p. 2274-2279, 2003.

[9] M. Santin, P. Colombo, and G. Bruschi, "Interfacial biology of in-stent restenosis," *Expert Review of Medical Devices,* vol. 2, p. 429-443, 2005.

[10] J. Daemen and P. W. Serruys, "Drug-eluting stent update 2007 part I: A survey of current and future generation drug-eluting stents: Meaningful advances or more of the same?," *Circulation,* vol. 116, p. 316-328, 2007.

[11] R. Fattori and T. Piva, "Drug-eluting stents in vascular intervention," *Lancet,* vol. 361, p. 247-249, 2003.

[12] P. W. Serruys, M. J. B. Kutryk, and A. T. L. Ong, "Drug therapy - Coronary-artery stents," *New England Journal of Medicine,* vol. 354, p. 483-495, 2006.

[13] M. A. Costa and D. I. Simon, "Molecular basis of restenosis and drug-eluting stents," *Circulation,* vol. 111, p. 2257-2273, 2005.

[14] T. Inoue and K. Node, "Molecular Basis of Restenosis and Novel Issues of Drug-Eluting Stents," *Circulation Journal,* vol. 73, p. 615-621, 2009.

[15] H. Takebayashi, G. S. Mintz, S. G. Carlier, Y. Kobayashi, K. Fujii, T. Yasuda, R. A. Costa, I. Moussa, G. D. Dangas, R. Mehran, A. J. Lansky, E. Kreps, M. B. Collins, A. Colombo, G. W. Stone, M. B. Leon, and J. W. Moses, "Nonuniform strut distribution

correlates with more neointimal hyperplasia after sirolimus-eluting stent implantation," *Circulation,* vol. 110, p. 3430-3434, 2004.

[16] S. G. Carlier, L. C. A. van Damme, C. P. Blommerde, J. J. Wentzel, G. van Langehove, S. Verheye, M. M. Kockx, M. W. M. Knaapen, C. Cheng, F. Gijsen, D. J. Duncker, N. Stergiopulos, C. J. Slager, P. W. Serruys, and R. Krams, "Augmentation of wall shear stress inhibits neointimal hyperplasia after stent implantation - Inhibition through reduction of inflammation?," *Circulation,* vol. 107, p. 2741-2746, 2003.

[17] J. J. Wentzel, R. Krams, J. C. H. Schuurbiers, J. A. Oomen, J. Kloet, W. J. van der Giessen, P. W. Serruys, and C. J. Slager, "Relationship between neointimal thickness and shear stress after wallstent implantation in human coronary arteries," *Circulation,* vol. 103, p. 1740-1745, 2001.

[18] R. Virmani, G. Guagliumi, A. Farb, G. Musumeci, N. Grieco, T. Motta, L. Mihalcsik, M. Tespili, O. Valsecchi, and F. D. Kolodgie, "Localized hypersensitivity and late coronary thrombosis secondary to a sirolimus-eluting stent should we be cautious?," *Circulation,* vol. 109, p. 701-705, 2004.

[19] T. F. Lüscher, J. Steffel, F. R. Eberli, M. Joner, G. Nakazawa, F. C. Tanner, and R. Virmani, "Drug-eluting stent and coronary thrombosis - Biological mechanisms and clinical implications," *Circulation,* vol. 115, p. 1051-1058, 2007.

[20] E. Deconinck, I. Sohier, I. De Scheerder, and G. Van Den Mooter, "Pharmaceutical aspects of drug eluting stents," *Journal of Pharmaceutical Sciences,* vol. 97, p. 5047-5060, 2008.

[21] A. V. Finn, G. Nakazawa, F. D. Kolodgie, and R. Virmani, "Temporal Course of Neointimal Formation After Drug-Eluting Stent Placement," *Jacc-Cardiovascular Interventions,* vol. 2, p. 300-302, 2009.

[22] R. Wessely, A. Schomig, and A. Kastrati, "Sirolimus and paclitaxel on polymer-based drug-eluting stents - Similar but different," *Journal of the American College of Cardiology,* vol. 47, p. 708-714, 2006.

[23] F. Vogt, A. Stein, G. Rettemeier, N. Krott, R. Hoffmann, J. vom Dahl, A. K. Bosserhoff, W. Michaeli, P. Hanrath, C. Weber, and R. Blindt, "Long-term assessment of a novel biodegradable paclitaxel-eluting coronary polylactide stent," *European Heart Journal,* vol. 25, p. 1330-1340, 2004.

[24] W. J. van der Giessen, A. M. Lincoff, R. S. Schwartz, H. M. M. vanBeusekom, P. W. Serruys, D. R. Holmes, S. G. Ellis, and E. J. Topol, "Marked inflammatory sequelae to implantation of biodegradable and nonbiodegradable polymers in porcine coronary arteries," *Circulation,* vol. 94, p. 1690-1697, 1996.

[25] A. D. Levin, N. Vukmirovic, C. W. Hwang, and E. R. Edelman, "Specific binding to intracellular proteins determines arterial transport properties for rapamycin and paclitaxel," *Proceedings of the National Academy of Sciences of the United States of America,* vol. 101, p. 9463-9467, 2004.

[26] A. D. Levin, M. Jonas, C. W. Hwang, and E. R. Edelman, "Local and systemic drug competition in drug-eluting stent tissue deposition properties," *Journal of Controlled Release,* vol. 109, p. 236-243, 2005.

[27] C. M. Yang and H. A. Burt, "Drug-eluting stents: Factors governing local pharmacokinetics," *Advanced Drug Delivery Reviews,* vol. 58, p. 402-411, 2006.

[28] C. J. Creel, M. A. Lovich, and E. R. Edelman, "Arterial paclitaxel distribution and deposition," *Circulation Research,* vol. 86, p. 879-884, 2000.

[29] M. A. Lovich, C. Creel, K. Hong, C. W. Hwang, and E. R. Edelman, "Carrier proteins determine local pharmacokinetics and arterial distribution of paclitaxel," *Journal of Pharmaceutical Sciences,* vol. 90, p. 1324-1335, 2001.

[30] A. R. Tzafriri, N. Vukmirovic, V. B. Kolachalama, I. Astafieva, and E. R. Edelman, "Lesion complexity determines arterial drug distribution after local drug delivery," *Journal of Controlled Release,* vol. 142, p. 332-338, 2010.

[31] C. W. Hwang and E. R. Edelman, "Arterial ultrastructure influences transport of locally delivered drugs," *Circulation Research,* vol. 90, p. 826-832, 2002.

[32] R. Wessely, J. Hausleiter, C. Michaelis, B. Jaschke, M. Vogeser, S. Milz, B. Behnisch, T. Schratzenstaller, M. Renke-Gluszko, M. Stover, E. Wintermantel, A. Kastrati, and A. Schomig, "Inhibition of neointima formation by a novel drug-eluting stent system that allows for dose-adjustable, multiple, and on-site stent coating," *Arteriosclerosis Thrombosis and Vascular Biology,* vol. 25, p. 748-753, 2005.

[33] G. Acharya and K. Park, "Mechanisms of controlled drug release from drug-eluting stents," *Advanced Drug Delivery Reviews,* vol. 58, p. 387-401, 2006.

[34] S. Venkatraman and F. Boey, "Release profiles in drug-eluting stents: Issues and uncertainties," *Journal of Controlled Release,* vol. 120, p. 149-160, 2007.

[35] S. V. Ranade, K. M. Miller, R. E. Richard, A. K. Chan, M. J. Allen, and M. N. Helmus, "Physical characterization of controlled release of paclitaxel from the TAXUS(TM) Express(2TM) drug-eluting stent," *Journal of Biomedical Materials Research Part A,* vol. 71A, p. 625-634, 2004.

[36] K. R. Kamath, J. J. Barry, and K. M. Miller, "The Taxus (TM) drug-eluting stent: A new paradigm in controlled drug delivery," *Advanced Drug Delivery Reviews,* vol. 58, p. 412-436, 2006.

[37] S. Fredenberg, M. Wahlgren, M. Reslow, and A. Axelsson, "The mechanisms of drug release in poly(lactic-co-glycolic acid)-based drug delivery systems - A review," *International Journal of Pharmaceutics,* vol. 415, p. 34-52, 2011.

[38] T. Sharkawi, D. Leyni-Barbaz, N. Chikh, and J. N. McMullen, "Evaluation of the in vitro drug release from resorbable biocompatible coatings for vascular stents," *Journal of Bioactive and Compatible Polymers,* vol. 20, p. 153-168, 2005.

[39] A. Finkelstein, D. McClean, S. Kar, K. Takizawa, K. Varghese, N. Baek, K. Park, M. C. Fishbein, R. Makkar, F. Litvack, and N. L. Eigler, "Local drug delivery via a coronary stent with programmable release pharmacokinetics," *Circulation,* vol. 107, p. 777-784, 2003.

[40] B. D. Klugherz, P. L. Jones, X. M. Cui, W. L. Chen, N. F. Meneveau, S. DeFelice, J. Connolly, R. L. Wilensky, and R. J. Levy, "Gene delivery from a DNA controlled-release stent in porcine coronary arteries," *Nature Biotechnology,* vol. 18, p. 1181-1184, 2000.

[41] C. J. Pan, J. J. Tang, Y. J. Weng, J. Wang, and N. Huang, "Preparation, characterization and anticoagulation of curcumin-eluting controlled biodegradable coating stents," *Journal of Controlled Release,* vol. 116, p. 42-49, 2006.

[42] C. J. Pan, J. J. Tang, Y. J. Weng, J. Wang, and N. Huang, "Preparation and characterization of rapamycin-loaded PLGA coating stent," *Journal of Materials Science-Materials in Medicine,* vol. 18, p. 2193-2198, 2007.

[43] C.-J. Pan, J.-J. Tang, Y.-J. Weng, J. Wang, and N. Huang, "Preparation and in vitro release profiles of drug-eluting controlled biodegradable polymer coating stents," *Colloids and Surfaces B: Biointerfaces,* vol. 73, p. 199-206, 2009.

[44] F. Alexis, S. S. Venkatraman, S. K. Rath, and F. Boey, "In vitro study of release mechanisms of paclitaxel and rapamycin from drug-incorporated biodegradable stent matrices," *Journal of Controlled Release,* vol. 98, p. 67-74, 2004.

[45] X. T. Wang, S. S. Venkatraman, F. Y. C. Boey, J. S. C. Loo, and L. P. Tan, "Controlled release of sirolimus from a multilayered PLGA stent matrix," *Biomaterials,* vol. 27, p. 5588-5595, 2006.

[46] M. Kamberi, S. Nayak, K. Myo-Min, T. P. Carter, L. Hancock, and D. Feder, "A novel accelerated in vitro release method for biodegradable coating of drug eluting stents: Insight to the drug release mechanisms," *European Journal of Pharmaceutical Sciences,* vol. 37, p. 217-222, 2009.

[47] T. F. Xi, R. L. Gao, B. Xu, L. A. Chen, T. Luo, J. Liu, Y. Wei, and S. P. Zhong, "In vitro and in vivo changes to PLGA/sirolimus coating on drug eluting stents," *Biomaterials,* vol. 31, p. 5151-5158, 2010.

[48] L. Lu, C. A. Garcia, and A. G. Mikos, "In vitro degradation of thin poly(DL-lactic-co-glycolic acid) films," *Journal of Biomedical Materials Research,* vol. 46, p. 236-244, 1999.

[49] J. Siepmann and N. A. Peppas, "Higuchi equation: Derivation, applications, use and misuse," *International Journal of Pharmaceutics,* vol. 418, p. 6-12, 2011.

[50] T. Higuchi, "Rate of Release of Medicaments from Ointment Bases Containing Drugs in Suspension," *Journal of Pharmaceutical Sciences,* vol. 50, p. 874-&, 1961.

[51] H. Q. Zhao, D. Jayasinghe, S. Hossainy, and L. B. Schwartz, "A theoretical model to characterize the drug release behavior of drug-eluting stents with durable polymer matrix coating," *Journal of Biomedical Materials Research Part A,* vol. 100A, p. 120-124, 2012.

[52] N. A. Peppas, "Analysis of Fickian and Non-Fickian Drug Release from Polymers," *Pharmaceutica Acta Helvetiae,* vol. 60, p. 110-111, 1985.

[53] S. Hossainy and S. Prabhu, "A mathematical model for predicting drug release from a biodurable drug-eluting stent coating," *Journal of Biomedical Materials Research Part A,* vol. 87A, p. 487-493, 2008.

[54] R. Mongrain, I. Faik, R. L. Leask, J. Rodes-Cabau, E. Larose, and O. F. Bertrand, "Effects of diffusion coefficients and struts apposition using numerical simulations for drug eluting coronary stents," *Journal of Biomechanical Engineering-Transactions of the Asme,* vol. 129, p. 733-742, 2007.

[55] C. W. Hwang, D. Wu, and E. R. Edelman, "Physiological transport forces govern drug distribution for stent-based delivery," *Circulation,* vol. 104, p. 600-605, 2001.

[56] B. Balakrishnan, J. F. Dooley, G. Kopia, and E. R. Edelman, "Intravascular drug release kinetics dictate arterial drug deposition, retention, and distribution," *Journal of Controlled Release,* vol. 123, p. 100-108, 2007.

[57] A. Borghi, E. Foa, R. Balossino, F. Migliavacca, and G. Dubini, "Modelling drug elution from stents: effects of reversible binding in the vascular wall and degradable polymeric matrix," *Computer Methods in Biomechanics and Biomedical Engineering,* vol. 11, p. 367-377, 2008.

[58] G. Vairo, M. Cioffi, R. Cottone, G. Dubini, and F. Migliavacca, "Drug release from coronary eluting stents: A multidomain approach," *Journal of Biomechanics,* vol. 43, p. 1580-1589, 2010.

[59] G. Pontrelli and F. de Monte, "A multi-layer porous wall model for coronary drug-eluting stents," *International Journal of Heat and Mass Transfer,* vol. 53, p. 3629-3637, 2010.

[60] B. Balakrishnan, J. Dooley, G. Kopia, and E. R. Edelman, "Thrombus causes fluctuations in arterial drug delivery from intravascular stents," *Journal of Controlled Release,* vol. 131, p. 173-180, 2008.

[61] M. A. Lovich and E. R. Edelman, "Mechanisms of Transmural Heparin Transport in the Rat Abdominal-Aorta after Local Vascular Delivery," *Circulation Research,* vol. 77, p. 1143-1150, 1995.

[62] M. A. Lovich, M. Philbrook, S. Sawyer, E. Weselcouch, and E. R. Edelman, "Arterial heparin deposition: role of diffusion, convection, and extravascular space," *American Journal of Physiology-Heart and Circulatory Physiology,* vol. 44, p. H2236-H2242, 1998.

[63] V. B. Kolachalama, A. R. Tzafriri, D. Y. Arifin, and E. R. Edelman, "Luminal flow patterns dictate arterial drug deposition in stent-based delivery," *Journal of Controlled Release,* vol. 133, p. 24-30, 2009.

[64] M. A. Lovick and E. R. Edelman, "Computational simulations of local vascular heparin deposition and distribution," *American Journal of Physiology-Heart and Circulatory Physiology,* vol. 40, p. H2014-H2024, 1996.

[65] D. V. Sakharov, L. V. Kalachev, and D. C. Rijken, "Numerical simulation of local pharmacokinetics of a drug after intravascular delivery with an eluting stent," *Journal of Drug Targeting,* vol. 10, p. 507-513, 2002.

[66] C. Vergara and P. Zunino, "Multiscale Boundary Conditions for Drug Release from Cardiovascular Stents," *Multiscale Modeling & Simulation,* vol. 7, p. 565-588, 2008.

[67] B. Balakrishnan, A. R. Tzafriri, P. Seifert, A. Groothuis, C. Rogers, and E. R. Edelman, "Strut position, blood flow, and drug deposition - Implications for single and overlapping drug-eluting stents," *Circulation,* vol. 111, p. 2958-2965, 2005.

[68] M. Grassi, G. Pontrelli, L. Teresi, G. Grassi, L. Comel, A. Ferluga, and L. Galasso, "Novel Design of Drug Delivery in Stented Arteries: A Numerical Comparative Study," *Mathematical Biosciences and Engineering,* vol. 6, p. 493-508, 2009.

[69] M. C. Delfour, A. Garon, and V. Longo, "Modeling and design of coated stents to optimize the effect of the dose," *Siam Journal on Applied Mathematics,* vol. 65, p. 858-881, 2005.

[70] P. Zunino, C. D'Angelo, L. Petrini, C. Vergara, C. Capelli, and F. Migliavacca, "Numerical simulation of drug eluting coronary stents: Mechanics, fluid dynamics and drug release," *Computer Methods in Applied Mechanics and Engineering,* vol. 198, p. 3633-3644, 2009.

[71] P. Mortier, G. A. Holzapfel, M. De Beule, D. Van Loo, Y. Taeymans, P. Segers, P. Verdonck, and B. Verhegghe, "A Novel Simulation Strategy for Stent Insertion and Deployment in Curved Coronary Bifurcations: Comparison of Three Drug-Eluting Stents," *Annals of Biomedical Engineering,* vol. 38, p. 88-99, 2010.

[72] F. von Burkersroda, L. Schedl, and A. Gopferich, "Why degradable polymers undergo surface erosion or bulk erosion," *Biomaterials,* vol. 23, p. 4221-4231, 2002.

[73] J. Siepmann and A. Göpferich, "Mathematical modeling of bioerodible, polymeric drug delivery systems," *Advanced Drug Delivery Reviews,* vol. 48, p. 229-247, 2001.

[74] C. K. Sackett and B. Narasimhan, "Mathematical modeling of polymer erosion: Consequences for drug delivery," *International Journal of Pharmaceutics,* vol. 418, p. 104-114, 2011.

[75] R. P. Batycky, J. Hanes, R. Langer, and D. A. Edwards, "A theoretical model of erosion and macromolecular drug release from biodegrading microspheres," *Journal of Pharmaceutical Sciences,* vol. 86, p. 1464-1477, 1997.

[76] A. Charlier, B. Leclerc, and G. Couarraze, "Release of mifepristone from biodegradable matrices: experimental and theoretical evaluations," *International Journal of Pharmaceutics,* vol. 200, p. 115-120, 2000.

[77] J. Siepmann and N. A. Peppas, "Modeling of drug release from delivery systems based on hydroxypropyl methylcellulose (HPMC)," *Advanced Drug Delivery Reviews,* vol. 48, p. 139-157, 2001.

[78] C. Raman, C. Berkland, K. Kim, and D. W. Pack, "Modeling small-molecule release from PLG microspheres: effects of polymer degradation and nonuniform drug distribution," *Journal of Controlled Release,* vol. 103, p. 149-158, 2005.

[79] P. Arosio, V. Busini, G. Perale, D. Moscatelli, and M. Masi, "A new model of resorbable device degradation and drug release - Part I: Zero order model," *Polymer International,* vol. 57, p. 912-920, 2008.

[80] G. Perale, P. Arosio, D. Moscatelli, V. Barri, M. Muller, S. Maccagnan, and M. Masi, "A new model of resorbable device degradation and drug release: Transient 1-dimension diffusional model," *Journal of Controlled Release,* vol. 136, p. 196-205, 2009.

[81] A. G. Thombre and K. J. Himmelstein, "A Simultaneous Transport-Reaction Model for Controlled Drug Delivery from Catalyzed Bioerodible Polymer Matrices," *AIChE Journal,* vol. 31, p. 759-766, 1985.

[82] S. Prabhu and S. Hossainy, "Modeling of degradation and drug release from a biodegradable stent coating," *Journal of Biomedical Materials Research Part A,* vol. 80A, p. 732-741, 2007.

[83] H. Antheunis, J. C. van der Meer, M. de Geus, A. Heise, and C. E. Koning, "Autocatalytic equation describing the change in molecular weight during hydrolytic degradation of aliphatic polyesters," *Biomacromolecules,* vol. 11, p. 1118-1124, 2010.

[84] R. Wada, S. H. Hyon, and Y. Ikada, "Kinetics of diffusion-mediated drug-release enhanced by matrix degradation," *Journal of Controlled Release,* vol. 37, p. 151-160, 1995.

[85] J. van Brakel and P. M. Heertjes, "Analysis of diffusion in macroporous media in terms of a porosity, a tortuosity and a constrictivity factor," *International Journal of Heat and Mass Transfer,* vol. 17, p. 1093-1103, 1974.

[86] W. M. Deen, "Hindered transport of large molecules in liquid-filled pores," *AIChE Journal,* vol. 33, p. 1409-1425, 1987.

[87] W. M. Deen, M. P. Bohrer, and N. B. Epstein, "Effects of molecular size and configuration on diffusion in microporous membranes," *AIChE Journal,* vol. 27, p. 952-959, 1981.

[88] S. R. Bailey, "DES design: Theoretical Advantages and Disadvantages of Stent Strut Materials, Design, Thickness, and Surface Characteristics," *Journal of Interventional Cardiology,* vol. 22, p. S3-S17, 2009.

[89] F. M. Zhang, M. Fath, R. Marks, and R. J. Linhardt, "A highly stable covalent conjugated heparin biochip for heparin-protein interaction studies," *Analytical Biochemistry,* vol. 304, p. 271-273, 2002.

[90] C. W. Hwang, A. D. Levin, M. Jonas, P. H. Li, and E. R. Edelman, "Thrombosis modulates arterial drug distribution for drug-eluting stents," *Circulation,* vol. 111, p. 1619-1626, 2005.

[91] T. Murata, T. Hiro, T. Fujii, K. Yasumoto, A. Murashige, M. Kohno, J. Yamada, T. Miura, and M. Matsuzaki, "Impact of the cross-sectional geometry of the post-deployment coronary stent on in-stent neointimal hyperplasia - An intravascular ultrasound study," *Circulation Journal,* vol. 66, p. 489-493, 2002.

[92] V. B. Kolachalama, A. R. Tzafriri, D. Y. Arifin, and E. R. Edelman, "Luminal flow patterns dictate arterial drug deposition in stent-based delivery (vol 133, pg 24, 2009)," *Journal of Controlled Release,* vol. 146, p. 160-160, 2010.

[93] D. R. Durran, *Numerical methods for wave equations in geophysical fluid dynamics.* New York: Springer, 1999.

[94] D. S. Cohen and T. Erneux, "Controlled drug release asymptotics," *Siam Journal on Applied Mathematics,* vol. 58, p. 1193-1204, 1998.

[95] W. Khan, S. Farah, and A. J. Domb, "Drug eluting stents: Developments and current status," *Journal of Controlled Release,* vol. 161, p. 703-712, 2012.

[96] J. M. Anderson and M. S. Shive, "Biodegradation and biocompatibility of PLA and PLGA microspheres," *Advanced Drug Delivery Reviews,* vol. 28, p. 5-24, 1997.

[97] T. Xi, R. Gao, B. Xu, L. Chen, T. Luo, J. Liu, Y. Wei, and S. Zhong, "In vitro and in vivo changes to PLGA/sirolimus coating on drug eluting stents," *Biomaterials,* vol. 31, p. 5151-5158, 2010.

[98] N. Faisant, J. Siepmann, and J. P. Benoit, "PLGA-based microparticles: Elucidation of mechanisms and a new, simple mathematical model quantifying drug release," *European Journal of Pharmaceutical Sciences,* vol. 15, p. 355-366, 2002.

[99] H. Antheunis, J. C. van der Meer, M. de Geus, W. Kingma, and C. E. Koning, "Improved mathematical model for the hydrolytic degradation of aliphatic polyesters," *Macromolecules,* vol. 42, p. 2462-2471, 2009.

[100] X. X. Zhu, B. G. Li, L. B. Wu, Y. G. Zheng, S. P. Zhu, K. D. Hungenberg, S. Mussig, and B. Reinhard, "Kinetics and modeling of vinyl acetate graft polymerization from poly(ethylene glycol)," *Macromolecular Reaction Engineering,* vol. 2, p. 321-333, 2008.

[101] R. McGraw, "Description of Aerosol Dynamics by the Quadrature Method of Moments," *Aerosol Science and Technology,* vol. 27, p. 255-265, 1997.

[102] A. N. Ford Versypt, D. W. Pack, and R. D. Braatz, "Mathematical modeling of drug delivery from autocatalytically degradable PLGA microspheres - A review," *Journal of Controlled Release,* vol. 165, p. 29-37, 2013.

[103] E. L. Cussler, *Diffusion: Mass Transfer in Fluid Systems*: Cambridge University Press, UK, 1997.

[104] W. E. Schiesser, *The Numerical Method of Lines: Integration of Partial Differential Equations* vol. 212: Academic Press, San Diego, 1991.

[105] L.-J. Shen and F.-L. L. Wu, "Nanomedicines in renal transplant rejection–focus on sirolimus," *International journal of nanomedicine,* vol. 2, p. 25, 2007.

[106] G. M. Ferron, W. D. Conway, and W. J. Jusko, "Lipophilic benzamide and anilide derivatives as high-performance liquid chromatography internal standards: Application to sirolimus (rapamycin) determination," *Journal of Chromatography B: Biomedical Sciences and Applications,* vol. 703, p. 243-251, 1997.

[107] W. J. Denny and M. T. Walsh, "Numerical modelling of mass transport in an arterial wall with anisotropic transport properties," *Journal of Biomechanics,* vol. 47, p. 168-177, 2014.

[108] X. Zhu, D. W. Pack, and R. D. Braatz, "Modelling intravascular delivery from drug-eluting stents with biodurable coating: investigation of anisotropic vascular drug diffusivity and arterial drug distribution," *Computer Methods in Biomechanics and Biomedical Engineering,* vol. 17, p. 187-198, 2012.

[109] W. J. Denny and M. T. Walsh, "Numerical modelling of the physical factors that affect mass transport in the vasculature at early time periods," *Medical Engineering & Physics,* vol. 36, p. 308-317, 2014.

[110] X. Zhu and R. D. Braatz, "A mechanistic model for drug release in PLGA biodegradable stent coatings coupled with polymer degradation and erosion," to be submitted.

[111] V. B. Kolachalama, S. D. Pacetti, J. W. Franses, J. J. Stankus, H. Q. Zhao, T. Shazly, A. Nikanorov, L. B. Schwartz, A. R. Tzafriri, and E. R. Edelman, "Mechanisms of tissue uptake and retention in zotarolimus-coated balloon therapy," *Circulation,* vol. 127, p. 2047-+, 2013.

[112] M. A. Lovich and E. R. Edelman, "Computational simulations of local vascular heparin deposition and distribution," *American Journal of Physiology-Heart and Circulatory Physiology,* vol. 40, p. H2014, 1996.

[113] J. J. Castellot, K. Wong, B. Herman, R. L. Hoover, D. F. Albertini, T. C. Wright, B. L. Caleb, and M. J. Karnovsky, "Binding and internalization of heparin by vascular smooth muscle cells," *Journal of Cellular Physiology,* vol. 124, p. 13-20, 1985.

[114] J.-F. Deux, A. Meddahi-Pellé, A. F. Le Blanche, L. J. Feldman, S. Colliec-Jouault, F. Brée, F. Boudghène, J.-B. Michel, and D. Letourneur, "Low molecular weight fucoidan prevents neointimal hyperplasia in rabbit iliac artery in-stent restenosis model," *Arteriosclerosis, thrombosis, and vascular biology,* vol. 22, p. 1604-1609, 2002.

[115] D. Wang and J. Tarbell, "Modeling interstitial flow in an artery wall allows estimation of wall shear stress on smooth muscle cells," *Journal of biomechanical engineering,* vol. 117, p. 358-363, 1995.

[116] Z. Tonar, P. Kochová, and J. Janáček, "Orientation, anisotropy, clustering, and volume fraction of smooth muscle cells within the wall of porcine abdominal aorta," *Applied and Computational Mechanics,* vol. 2, p. 145-146, 2008.

[117] J. A. Rhodin, "Architecture of the vessel wall," *Comprehensive Physiology,* 2011.

[118] T. Roby, S. Olsen, and J. Nagatomi, "Effect of sustained tension on bladder smooth muscle cells in three-dimensional culture," *Annals of Biomedical Engineering,* vol. 36, p. 1744-1751, 2008.

[119] H. S. Fogler, *Elements of Chemical Reaction Engineering*: Prentice-Hall International London, 1999.

[120] G. A. Truskey, F. Yuan, and D. F. Katz, *Transport phenomena in biological systems*: Pearson/Prentice Hall Upper Saddle River NJ:, 2004.

[121] T. Kourti and J. F. MacGregor, "Multivariate SPC methods for process and product monitoring," *Journal of Quality Technology,* vol. 28, 1996.

[122] S. J. Qin, "Survey on data-driven industrial process monitoring and diagnosis," *Annual Reviews in Control,* vol. 36, p. 220-234, 2012.

[123] E. Russell, L. H. Chiang, and R. D. Braatz, *Data-driven methods for fault detection and diagnosis in chemical processes.* London: Springer, 2000.

[124] S. Joe Qin, "Statistical process monitoring: basics and beyond," *Journal of Chemometrics,* vol. 17, p. 480-502, 2003.

[125] J. A. Westerhuis, S. P. Gurden, and A. K. Smilde, "Generalized contribution plots in multivariate statistical process monitoring," *Chemometrics and Intelligent Laboratory Systems,* vol. 51, p. 95-114, 2000.

[126] J. J. Downs and E. F. Vogel, "A plant-wide industrial process control problem," *Computers & Chemical Engineering,* vol. 17, p. 245-255, 1993.

[127] N. Ricker and J. Lee, "Nonlinear model predictive control of the Tennessee Eastman challenge process," *Computers & Chemical Engineering,* vol. 19, p. 961-981, 1995.

[128] T. J. McAvoy and N. Ye, "Base control for the Tennessee Eastman problem," *Computers & Chemical Engineering,* vol. 18, p. 383-413, 1994.

[129] P. R. Lyman and C. Georgakis, "Plant-wide control of the Tennessee Eastman problem," *Computers & Chemical Engineering,* vol. 19, p. 321-331, 1995.

[130] A. D. Randolph and M. A. Larson, *Theory of particulate processes : analysis and techniques of continuous crystallization.* New York: Academic Press, 1971.

[131] T. E. Ramabhadran, T. W. Peterson, and J. H. Seinfeld, "Dynamics of Aerosol Coagulation and Condensation," *AIChE Journal,* vol. 22, p. 840-851, 1976.

[132] N. V. Mantzaris, J.-J. Liou, P. Daoutidis, and F. Srienc, "Numerical solution of a mass structured cell population balance model in an environment of changing substrate concentration," *Journal of Biotechnology,* vol. 71, p. 157-174, 1999.

[133] T. J. Crowley, E. S. Meadows, E. Kostoulas, and F. J. Doyle Iii, "Control of particle size distribution described by a population balance model of semibatch emulsion polymerization," *Journal of Process Control,* vol. 10, p. 419-432, 2000.

[134] U. Teipel, "Particle Technology: Design of Particulate Products and Dispersed Systems," *Chemical Engineering & Technology,* vol. 27, p. 751-756, 2004.

[135] Z. K. Nagy and R. D. Braatz, "Advances and New Directions in Crystallization Control," *Annual Review of Chemical and Biomolecular Engineering,* vol. 3, p. 55-75, 2012.

[136] R. D. Braatz, "Advanced control of crystallization processes," *Annual Reviews in Control,* vol. 26, p. 87-99, 2002.

[137] R. Gunawan, I. Fusman, and R. D. Braatz, "Parallel high-resolution finite volume simulation of particulate processes," *AIChE Journal,* vol. 54, p. 1449-1458, 2008.

[138] J. Gimbun, Z. K. Nagy, and C. D. Rielly, "Simultaneous Quadrature Method of Moments for the Solution of Population Balance Equations, Using a Differential Algebraic Equation Framework," *Industrial & Engineering Chemistry Research,* vol. 48, p. 7798-7812, 2009.

[139] D. L. Marchisio, J. T. Pikturna, R. O. Fox, R. D. Vigil, and A. A. Barresi, "Quadrature method of moments for population-balance equations," *AIChE Journal,* vol. 49, p. 1266-1276, 2003.

[140] D. L. Ma, D. K. Tafti, and R. D. Braatz, "High-resolution simulation of multidimensional crystal growth," *Industrial & Engineering Chemistry Research,* vol. 41, p. 6217-6223, 2002.

[141] R. Gunawan, I. Fusman, and R. D. Braatz, "High resolution algorithms for multidimensional population balance equations," *AIChE Journal,* vol. 50, p. 2738-2749, 2004.

[142] M. J. Hounslow, R. L. Ryall, and V. R. Marshall, "A discretized population balance for nucleation, growth, and aggregation," *AIChE Journal,* vol. 34, p. 1821-1832, 1988.

[143] M. Smith and T. Matsoukas, "Constant-number Monte Carlo simulation of population balances," *Chemical Engineering Science,* vol. 53, p. 1777-1786, 1998.

[144] Y. Lin, K. Lee, and T. Matsoukas, "Solution of the population balance equation using constant-number Monte Carlo," *Chemical Engineering Science,* vol. 57, p. 2241-2252, 2002.

[145] E. Aamir, Z. K. Nagy, C. D. Rielly, T. Kleinert, and B. Judat, "Combined Quadrature Method of Moments and Method of Characteristics Approach for Efficient Solution of Population Balance Models for Dynamic Modeling and Crystal Size Distribution Control of Crystallization Processes," *Industrial & Engineering Chemistry Research,* vol. 48, p. 8575-8584, 2009.

[146] A. E. Flood, "Thoughts on Recovering Particle Size Distributions from the Moment Form of the Population Balance," *Developments in Chemical Engineering and Mineral Processing,* vol. 10, p. 501-519, 2002.

[147] S. Qamar, M. P. Elsner, I. A. Angelov, G. Warnecke, and A. Seidel-Morgenstern, "A comparative study of high resolution schemes for solving population balances in crystallization," *Computers & Chemical Engineering,* vol. 30, p. 1119-1131, 2006.

[148] P. Marchal, R. David, J. P. Klein, and J. Villermaux, "Crystallization and Precipitation Engineering .1. An Efficient Method for Solving Population Balance in Crystallization with Agglomeration," *Chemical Engineering Science,* vol. 43, p. 59-67, 1988.

[149] F. Puel, G. Fevotte, and J. P. Klein, "Simulation and analysis of industrial crystallization processes through multidimensional population balance equations. Part 2: a study of semi-batch crystallization," *Chemical Engineering Science,* vol. 58, p. 3729-3740, 2003.

[150] S. Kumar and D. Ramkrishna, "On the solution of population balance equations by discretization—III. Nucleation, growth and aggregation of particles," *Chemical Engineering Science,* vol. 52, p. 4659-4679, 1997.

[151] S. Qamar, A. Ashfaq, I. Angelov, M. P. Elsner, G. Warnecke, and A. Seidel-Morgenstern, "Numerical solutions of population balance models in preferential crystallization," *Chemical Engineering Science,* vol. 63, p. 1342-1352, 2008.

[152] F. Fevotte and G. Fevotte, "A method of characteristics for solving population balance equations (PBE) describing the adsorption of impurities during crystallization processes," *Chemical Engineering Science,* vol. 65, p. 3191-3198, 2010.

[153] M. J. Hounslow and G. K. Reynolds, "Product engineering for crystal size distribution," *AIChE Journal,* vol. 52, p. 2507-2517, 2006.

[154] S. Qamar, S. Mukhtar, A. Seidel-Morgenstern, and M. P. Elsner, "An efficient numerical technique for solving one-dimensional batch crystallization models with size-dependent growth rates," *Chemical Engineering Science,* vol. 64, p. 3659-3667, 2009.

[155] A. Mesbah, H. J. M. Kramer, A. E. M. Huesman, and P. M. J. Van den Hof, "A control oriented study on the numerical solution of the population balance equation for crystallization processes," *Chemical Engineering Science,* vol. 64, p. 4262-4277, 2009.

[156] S. Qamar and G. Warnecke, "Numerical solution of population balance equations for nucleation, growth and aggregation processes," *Computers & Chemical Engineering,* vol. 31, p. 1576-1589, 2007.

[157] S. J. Farlow, *Partial Differential Equations for Scientists and Engineers.* New York: Dover, 1993.

[158] R. G. Gordon, "Error Bounds in Equilibrium Statistical Mechanics," *Journal of Mathematical Physics,* vol. 9, p. 655-663, 1968.

[159] V. Liotta and V. Sabesan, "Monitoring and Feedback Control of Supersaturation Using ATR-FTIR to Produce an Active Pharmaceutical Ingredient of a Desired Crystal Size," *Organic Process Research & Development,* vol. 8, p. 488-494, 2004.

[160] H. Grön, P. Mougin, A. Thomas, G. White, D. Wilkinson, R. B. Hammond, X. Lai, and K. J. Roberts, "Dynamic In-Process Examination of Particle Size and Crystallographic Form under Defined Conditions of Reactant Supersaturation as Associated with the Batch Crystallization of Monosodium Glutamate from Aqueous Solution," *Industrial & Engineering Chemistry Research,* vol. 42, p. 4888-4898, 2003.

[161] G. X. Zhou, M. Fujiwara, X. Y. Woo, E. Rusli, H. H. Tung, C. Starbuck, O. Davidson, Z. H. Ge, and R. D. Braatz, "Direct design of pharmaceutical antisolvent crystallization through concentration control," *Crystal Growth & Design,* vol. 6, p. 892-898, 2006.